POLITECNICO DI MILANO

SCHOOL OF INDUSTRIAL AND INFORMATION ENGINEERING

DEPARTMENT OF ENERGY

MASTER OF SCIENCE IN NUCLEAR ENGINEERING

ENHANCING PERSONAL NEUTRON DOSIMETRY USING SSNTD: NUMERICAL AND EXPERIMENTAL LET ESTIMATION OF THE TRACKS, VIA THE POLITRACK™ SYSTEM

Advisor:
Marco Caresana

Co-Advisor:
Marie-Anne Chevallier

Graduation thesis of:
Simone Cannarozzo - 884181

RÉPUBLIQUE FRANÇAISE
Liberté
Égalité
Fraternité

IRSN
INSTITUT DE RADIOPROTECTION ET DE SÛRETÉ NUCLÉAIRE

Academic Year 2019/2020

Contents

List of figures

Note: this list does not contain the citation of the source the image was taken from (if not personally produced). Of course, the references will be present in the text.

List of tables

Abstract

The aim of this thesis work is to investigate the feasibility of a spectroscopy technique using CR-39 solid state nuclear track detectors, in order to compensate the response in dose of the dosimeters which is dependent on the energy of the incident particle, in the context of personal neutron dosimetry. Neutrons hitting this plastic material, in fact, can produce recoil protons which release energy in the surrounding volume. After an etching process, these "activated" regions are corroded faster, thus producing tracks. Their morphology depends on the etching parameters and on the direction and energy of the recoil protons which in turn depend on the incident neutrons.

The hypothesis is that a link can be found between the morphology of the tracks and the spectrum of the neutron radiation field. To investigate this supposition, two studies have been conducted in parallel and finally compared: one experimental and the other computational.

In the experimental part, several irradiations were planned employing monoenergetic protons and neutrons which were eventually cancelled due to the SARS-CoV-2 outbreak. For this reason, data from past dosimeters (exposed to monoenergetic fields) were analysed using the Politrack™ system, a device capable of producing an LET spectrum through the combination of an optical system and a calculation software. The goal was to find a trend useful for the identification of the different energies from the LET spectra, in the simple case of monoenergetic irradiations.

As for as the computational part, a simulation environment has been built using the C++ language and the Geant4 toolkit. This software has been coded trying to reproduce the Politrack™ analysis routine, by simulating for each neutron the eventual recoil proton produced and how the track morphology should evolve from it. The reasons behind the development of this simulation are two. One is to understand if, from a theoretical point of view, neutrons at different energies can produce different LET spectra. The other is to have a tool which can figure out in advance the LET spectra of more complex fields, by reproducing accurately the behaviour of the dosimetric system.

Keywords: personal neutron dosimetry, CR-39, LET, Politrack™, Geant4.

Estratto

L'obbiettivo di questa tesi di laurea è di studiare le potenzialità di una tecnica spettroscopica mediante l'uso di rivelatori di tracce a stato solido in CR-39 nel contesto della dosimetria personale neutronica, con lo scopo finale di compensare la loro risposta in dose che dipende, la quale dipende dall'energia dei neutroni incidenti.

I neutroni, quando colpiscono il CR-39, posso produrre protoni di rinculo che depositano energia nel volume circostante. Un attacco chimico successivamente corrode maggiormente queste zone e produce delle tracce la quale morfologia dipende dai parametri del processo e da energia e direzione della particella che produce il danno, e quindi indirettamente dalle caratteristiche del neutrone iniziale.

L'idea alla base di questo lavoro è quindi che si può trovare un nesso tra la morfologia delle tracce e lo spettro del campo neutronico. Per studiare questa ipotesi, il lavoro è stato diviso in due parti, una sperimentale e una computazionale, i quali risultati sono stati alla fine confrontati.

In quella sperimentale, dopo l'annullamento a causa della pandemia di SARS-CoV-2 di una campagna già pianificata di irraggiamenti, sono stati usati dati da dosimetri precedentemente esposti a campi monocromatici di protoni e neutroni ed esaminati usando il sistema Politrack™. Questo è uno strumento che produce spettri di LET sulla base dell'analisi visiva della morfologia delle tracce nel CR-39.

Per la parte computazionale, è stato sviluppato un ambiente di simulazione usando il linguaggio C++ ed il toolkit Geant4 per riprodurre il metodo di analisi del Politrack™, simulando, per ogni neutrone, l'eventuale protone di rinculo e l'evoluzione della morfologia della traccia. Questo software è stato scritto per due motivi: uno è quello di per capire se, da un punto di vista teorico, i neutroni ad energie diverse possono produrre spettri di LET diversi; l'altro è per avere uno strumento in grado di anticipare gli spettri di campi di radiazioni più complessi di quelli monocromatici, riproducendo fedelmente un'analisi eseguita col Politrack™.

Parole chiave: dosimetria individuale neutronica, CR-39, LET, Politrack™, Geant4.

Sommario

L'obiettivo principale di questa tesi di laurea è di studiare la possibilità di usare dosimetri a tracce nucleari allo stato solido (SSNTD), impiegati nell'ambito della dosimetria personale neutronica, per riconoscere lo spettro energetico di un campo di neutroni. La risposta di questi dosimetri infatti dipende dall'energia dei neutroni, come mostrato nella **Figura 1** nello specifico per il particolare tipo di dosimetro usato in questo lavoro.

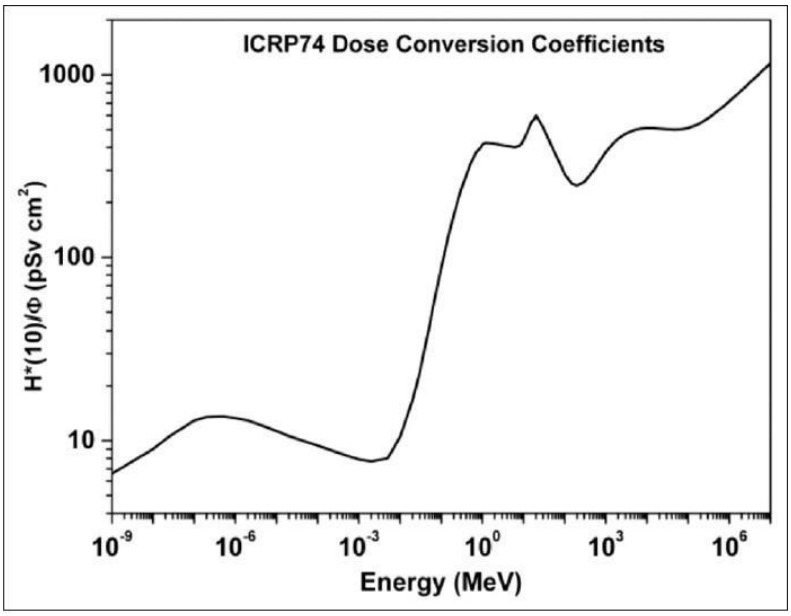

Figura 1 *– Fattore di conversion tra equivalente di dose ambientale e fluenza neutronica (H*(10)/ Φ(E)) in funzione dell'energia per SSNTD di CR-39. (Source International Commission on Radiological Protection. Conversion Coefficients for Use in Radiological Protection against External Radiation. ICRP Publication 74.)*

Per quanto riguarda il dosimetro infatti, si tratta di un materiale plastico [poliallil-diglicol-carbonato, $(C_5O_2H_8)_n$], comunemente noto col nome di CR-39, con un'area di 25 x 25 mm e 1,5 mm di spessore, accoppiato ad un radiatore in PMMA [polimetilmetacrilato, $(C_5O_2H_8)_n$], avente la stessa area ma uno spessore di 10 mm, come mostrato nella **Figura 2**, che serve ad

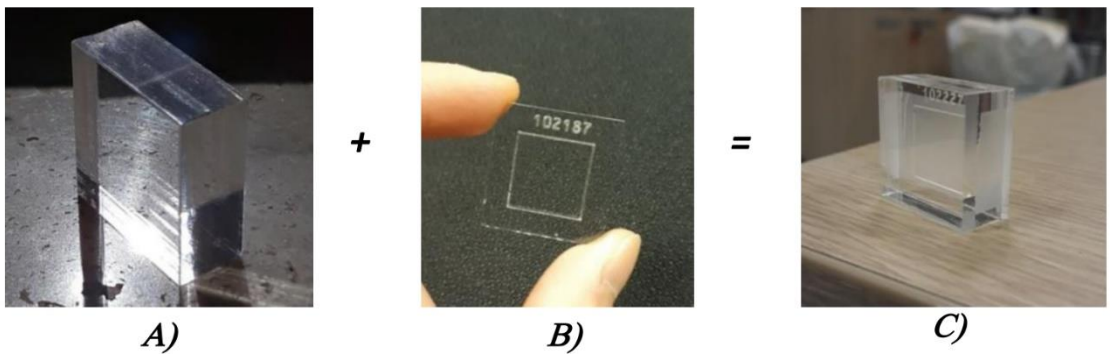

Figura 2 *– Il radiatore di PMMA (A) e il rivelatore di CR-39 (B) che compongono il dosimetro (C). Le due componenti sono unite mediante comune nastro adesivo. (Fonte: Bolzonella, M. (2019). Characterization of a passive dosimeter based on a CR-39 track detector for envoironmental and personal dosimetry in neutron mixed fields. Politecnico di Milano.)*

aumentare la possibilità di interazione e garantire l'equilibrio di particelle cariche anche per neutroni di alta energia.

Entrambi i materiali sono sensibili alla radiazione neutronica grazie alle reazioni che possono avvenire tra i neutroni e i loro costituenti, cioè C, O e H. Solo l'ultimo di questi però è stato preso in considerazione in questo lavoro, perché la reazione di gran lunga più probabile nel range energetico in esame (tra i 144 keV e i 5 MeV) è quella di scattering elastico sull'idrogeno con produzione di protoni di rinculo. Questi protoni a loro volta cedono energia attraverso l'eccitazione e soprattutto la ionizzazione del materiale che si trova nel percorso e lasciano delle tracce, dette "latenti", di materiale reso più sensibile ad attacchi chimici. Infatti, dopo l'irraggiamento, attraverso un bagno in idrossido di sodio (chiamato solitamente "etching") la superficie di CR-39 viene erosa ad una velocita, detta *velocità di attacco del bulk* V_b, mentre l'erosione lungo le tracce latenti avviene alla *velocità di attacco della traccia* V_t che è superiore e dipende dal LET della particella. Questa disproporzione tra le due velocità porta alla formazione delle vere e proprie tracce.

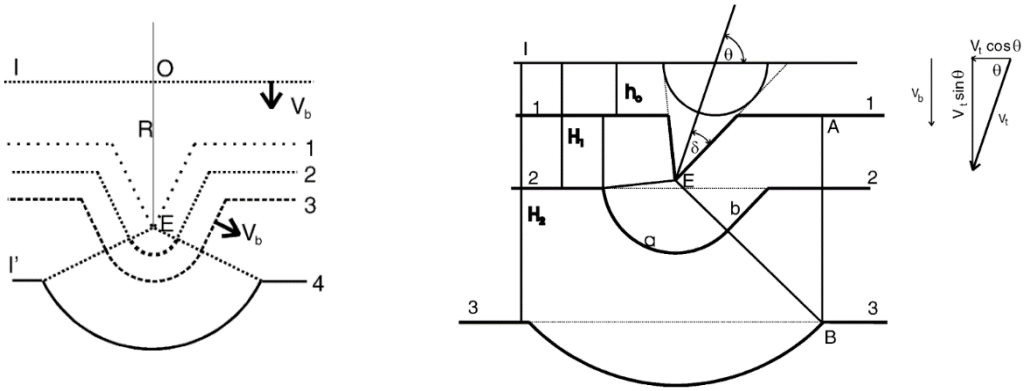

Figura 3 *– Fasi dello sviluppo della traccia, da sottosviluppata (1) a sovrasviluppata (4 nell'immagine di sinistra e 3 in quella di destra) per incidenza perpendicolare (immagine a sinistra) e obliqua (a destra). (Source Nikezic D, Yu N. K.. (2004) Formation and growth of tracks in nuclear track materials. Materials Science and Engineering R: Reports..)*

Le tracce, durante il processo di etching, vengono erose a poco a poco e possono attraversare varie fasi, illustrate nella **Figura 3**, passando da sottosviluppate (o underetched comunemente), con una forma conica rappresentativa dell'energia della particella, a sovrasviluppate (o overetched), quando assumono una forma sferica, in cui non è più possibile risalire all'energia. La fase di transizione da uno stato all'altro avviene quando l'etching corrode fino alla fine della traccia latente (cioè dove si ferma il protone) e successivamente prosegue alla velocità di bulk anche nell'estremità della traccia.

Il LET della particella, insieme alle caratteristiche dell'etching, determinano la forma finale della traccia. Infatti, *V*, che è il rapporto tra le velocità di etching ($V \equiv V_t/V_b$), dipende dal LET della particella e a sua volta la sezione della traccia dipende da *V* e da *h*, che è sostanzialmente la profondità alla quale è arrivato l'etching ed è data dal prodotto tra la velocità di bulk e il tempo in cui il dosimetro resta nel bagno chimico.

È possibile ripercorrere questi passaggi al contrario per collegare una quantità fisica misurabile, come la forma della sezione della traccia al LET della particella che l'ha prodotta. Infatti, ci si serve di modelli fisici che collegano *V* all' asse maggiore *D*, l'asse minore *d* (che sono appunto gli assi della sezione ellissoidale della traccia) e allo spessore rimosso *h*. Attraverso un secondo modello che lega *V* e LET, è quindi possibile produrre degli spettri di LET dall'analisi dei dosimetri, che sono alla base del lavoro svolto in questa tesi.

Infatti, questo è ciò che fai il Politrack™, il quale è composto principalmente da un sistema ottico, combinato ad uno di movimentazione dei dosimetri, che in maniera automatica scatta foto della superficie dei dosimetri (cf. **Figura 4**), e le sottopone a un software che analizza le tracce visibili in queste immagini. Dal calcolo della lunghezza degli assi, quindi, stima un valore di *LET* (che essendo quello calcolato dal sistema verrà chiamato LET_{nc}) per ogni traccia che identifica, e che restituisce alla fine dell'analisi dell'intera superficie sensibile insieme ad un'altra serie di latri dati, tra cui l'angolo di incidenza.

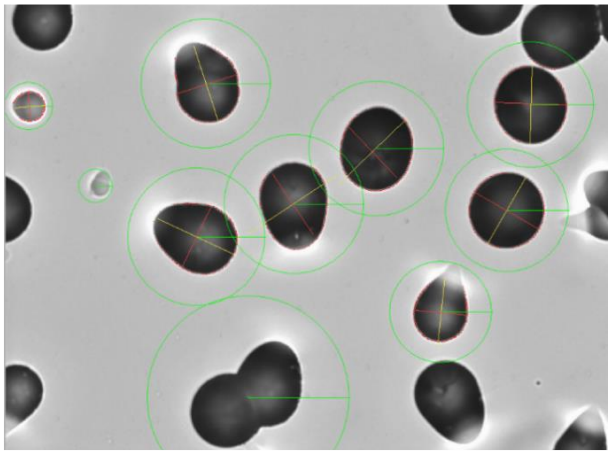

Figura 4 *– A sinistra, un esempio di foto scattata dal Politrack durante l'analisi. Si può vedere la caratteristica forma allungata delle tracce.*

Questa tesi parte da queste premesse per sviluppare uno studio volto a migliorare la dosimetria neutronica personale. L'obiettivo fissato è quello di capire se sia possibile, dagli spettri di LET_{nc}, risalire all'energia dei neutroni di un campo di radiazioni, perché *LET* ed energia di una particella sono profondamente connessi. Per fare questo è stato necessario partire dalla

situazione più semplice possibile, cioè campi neutronici monocromatici, e dividere lo studio in due parti: una sperimentale ed una computazionale.

La parte sperimentale prevede l'analisi di dosimetri irraggiati con protoni e neutroni monocromatici per caratterizzare la loro risposta in situazioni molto semplici, per poi estendere lo studio a sorgenti più complesse, come californio e americio-berillio. Nello specifico, grazie ai dosimetri irraggiati con protoni monocromatici, dovrebbe essere possibile capire l'efficacia del modello fisico usato per mettere in relazione *V* e *LET*, che non è stato mai testato con i protoni, e quindi la capacità del sistema dosimetrico di restituire uno spettro di LET_{nc} caratteristico per diverse energie. L'irraggiamento con neutroni invece ci permetterebbe di capire come cambiano gli spettri di LET_{nc} al variare dell'energia dei neutroni e se ci sono le basi per una eventuale spettrometria. Questi irraggiamenti si sarebbero dovuti tenere nella struttura dell'IRSN che ospita gli esperimenti MIRCOM (Ion microbeam for the radiobiology of intra and intercellular communications) e AMANDE (Accelerator for metrology and neutron applications for external dosimetry), illustrati in **Figura 5**.

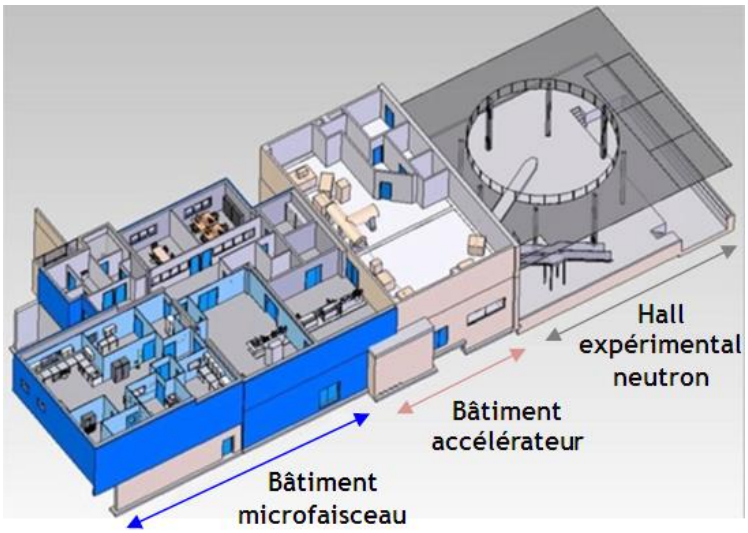

Figura 5 *– Struttura che ospita MIRCOM (sulla sinistra) e AMANDE (sulla destra). (Fonte: https://www.irsn.fr/FR/Larecherche/Actualites_Agenda/Actualites/Pages/2016-02-05-inauguration-installation-MIRCOM)*

Il primo è un acceleratore di protoni ad altissima precisione energetica ma soprattutto spaziale mentre il secondo è in grado di produrre neutroni con una precisione energetica altissima, soprattutto grazie a una struttura molto ampia e con griglie metalliche invece di cemento che permette di avere pochissimi neutroni rimbalzati sul detector dai materiali costruttivi.

Tuttavia, a causa delle chiusure degli impianti indotte dalla pandemia di SARS-CoV-2, gli irraggiamenti originariamente pianificati non sono stati condotti e sono stati sostituiti da dati da precedenti campagne sperimentali, usando i dosimetri elencati nella **Tabella 1**.

***Tabella 1**: Dosimetri analizzati in questo lavoro.*

Facility	Particle	Energy	Etching time	Removed layer
MIRCOM	proton	1,5 MeV	70 min	unknown
			90 min	unknown
		2,5 MeV	90 min	unknown
AMANDE	neutron	565 keV	90 min	15 µm
		2,5 MeV	90 min	15 µm
		5 MeV	90 min	15 µm
National Physical Laboratory (NPL)	neutron	565 keV	90 min	19,5 µm
		1,2 MeV	90 min	19,5 µm
		2,5 MeV	90 min	19,5 µm
		5 MeV	90 min	19,5 µm

Per quanto riguarda i protoni, sono stati usati dosimetri comunque irraggiati a MIRCOM ma per i quali non è stato possibile condure positivamente una calibrazione. Questo restituisce dei dati sui quali non è possibile lavorare nel senso inizialmente proposto, e che vengono usati principalmente per dimostrare che è necessario conoscere in modo molto preciso il valore di V_b (e quindi una buona calibrazione) per avere il valore di LET_{nc} realmente misurato, come illustrato in **Figura 6**.

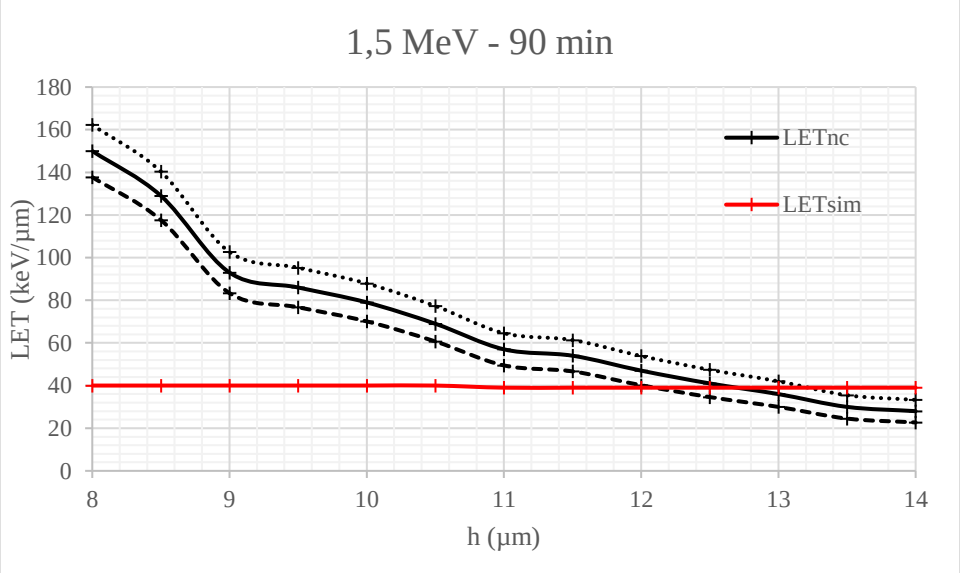

***Figura 6** – Andamento del valore di picco della distribuzione di LET in funzione dello spessore rimosso, per dati sperimentali e simulazioni nel caso di dosimetri irraggiati con protoni da 1,5 MeV e dopo un bagno chimico durato 90 minuti. LE line tratteggiate corrispondono al valore di LET_{nc} più e meno la deviazione standard.*

Quello che non è possibile investigare è la validità dell'equazione che lega *V* e *LET* nel range dei protoni ed è importante sottolineare che era un passaggio fondamentale per questo studio e per quelli futuri su questo argomento.

Passando ai neutroni, sono stati analizzati i dati di dosimetri irraggiati in campagne precedenti ad AMANDE e nei laboratori del National Physical Laboratory (NPL) a Teddington (UK), dove si trova un acceleratore di neutroni simile ad AMANDE, ma con delle performance relativamente meno elevate.

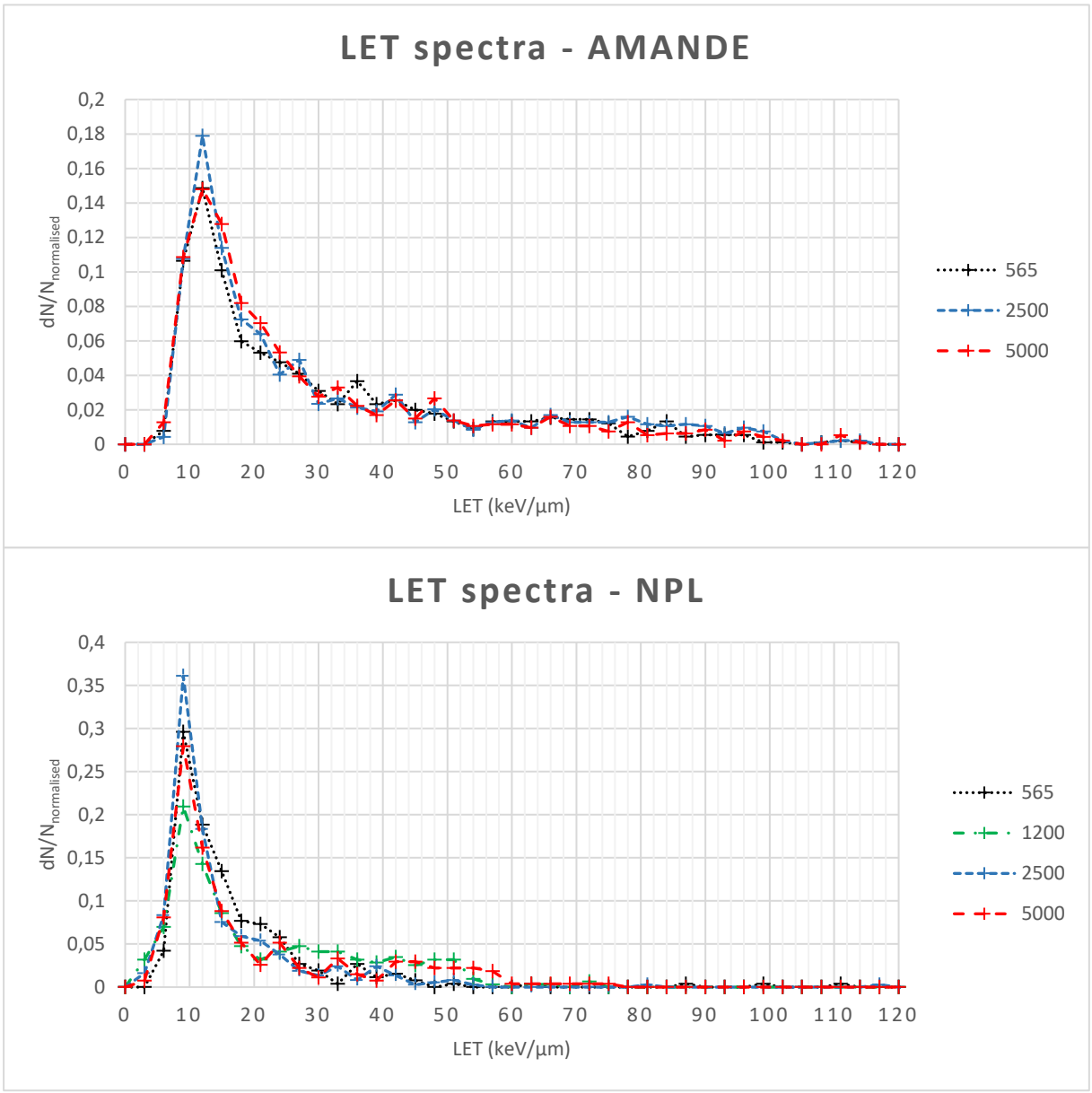

Figura 7 *– Spettri di LET_{nc} dei dosimetri irraggiati ad AMANDE e NPL a diverse energie.*

Quello che è emerso dall'analisi, mostrato nella **Figura 7** è che le distribuzioni hanno sempre un picco a valori di LET_{nc} molto bassi e che sono tutte sostanzialmente uguali. Tuttavia, a causa

della mancanza di dati dall'analisi dei protoni, non è possibile risalire al motivo per il quale i dosimetri hanno questo comportamento.

La parte computazionale di questo lavoro, invece, è stata basata sullo sviluppo di un software per capire se, da un punto di vista teorico, sia possibile avere spettri diversi a diverse energie e successivamente se sia possibile avere coincidenza tra i risultati delle simulazioni e i dati sperimentali. Se quest'ultimo punto fosse possibile, inoltre, le simulazioni potrebbero essere utilizzate per anticipare spettri più complessi ed essere usata in situazioni meno intuitive dei campi monocromatici.

Da un punto di vista pratico, la parte computazionale consiste nello sviluppo di un codice in grado di simulare al meglio l'irraggiamento di dosimetri di CR-39, l'etching e l'analisi. È stata quindi sviluppato un software scritto nel linguaggio di programmazione C++ attraverso l'uso di un toolkit chiamato Geant4. Quest'ultimo è sostanzialmente una libreria, cioè una raccolta di parti di codice già scritte da mettere insieme e modificare in base alle specifiche necessità per costruire la simulazione cercata. Geant4 permette di costruire simulazioni dalle prestazioni molto elevate, essendo scritto in un linguaggio molto efficiente, e soprattutto offre una grande quantità di modelli fisici molto affidabili da usare in base ai range e alle particelle coinvolte negli eventi fisici da riprodurre.

Nel corso del lavoro, sono state sviluppati due diversi metodi per il calcolo del *LET* (che essendo quello specifico delle simulazioni verrà da qui in poi definito LET_{sim}) con due filosofie molto differenti. Nella prima versione, il LET_{sim} veniva definito come l'energia depositata dal protone di rinculo divisa per il suo percorso. L'energia era calcolata integrando i singoli contributi depositati nelle interazioni col materiale dal punto di ingresso o di produzione del protone di rinculo fino alla fine teorica della traccia, che veniva calcolata utilizzando un modello fisico che cercava di ricalcare al meglio il vero etching di una traccia. Questo avveniva passando dall'energia del protone al *LET* e quindi alla velocità di etching della traccia, e, moltiplicando questa per il tempo, si otteneva la profondità teorica della traccia. Questo metodo tuttavia era poco efficace quando si trattava di analizzare protoni di rinculo che producevano tracce sovrasviluppate e quelli prodotti tra la superficie e lo spessore rimosso (definita anche auto-radiazione), illustrate in **Figura 9**.

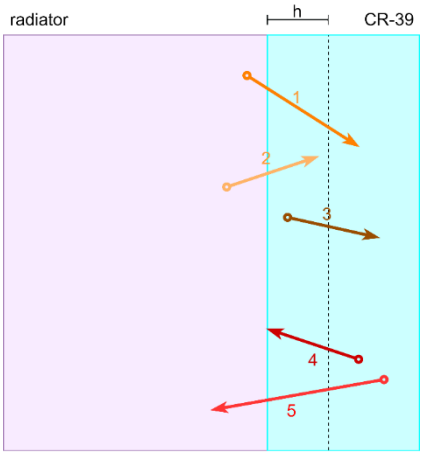

Figura 9 *– Schematizzazione delle diverse tipologie di protoni di rinculo e che possono portare alla formazione di tracce. (1) sono quelli che producono tracce sottosviluppate, (2) sovrasviluppate, (3) da auto-radiazione.*

Per risolvere questo problema, è stato sviluppato un secondo metodo, che al calcolo della profondità teorica e all'integrazione, sostituisce il calcolo della morfologia della traccia. Sfruttando un modello fisico di Somogyi and Szalay, il programma stima prima il rapporto tra le velocità di etching e poi da questo, grazie anche all'angolo di incidenza e in base allo spessore rimosso, calcola gli assi della sezione della traccia che quel protone avrebbe prodotto, secondo lo schema in **Figura 8**.

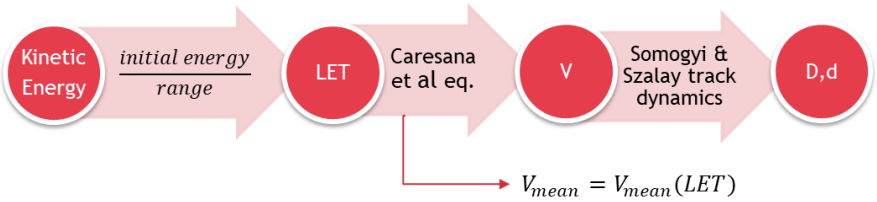

Figura 8 *– Schema della routine per calcolare gli assi maggiori e minori durante la simulazione.*

Da questo poi il LET_{sim} viene calcolato usando le stesse equazioni che usa il software di analisi del Politrack™, perché si ha lo stesso tipo di informazione in questi due casi. È quindi evidente come questa seconda filosofia si avvicini di più a quello che avviene sperimentalmente. Alla fine della simulazione, vengono quindi prodotto degli spettri di LET_{sim} mostrati nella **Figura 10**.

Come si può vedere, questi sono molto diversi rispetto i dati sperimentali (cf. **Figura 10**) e mostrano che forse, da un punto di vista teorico, una discriminazione è possibile. È allo stesso tempo chiaro che qualcosa prevenga una corrispondenza tra i dati simulati e quelli ricavati dai dosimetri. È difficile capire quale sia il fattore che lo determina, soprattutto a causa della mancanza di dati sugli irraggiamenti protonici. Infatti, un problema che potrebbe sicuramente

spiegare queste differenze, sarebbe un errore nelle equazioni che legano *V* e *LET* usate sia nell'analisi dei dati sperimentali che nelle simulazioni.

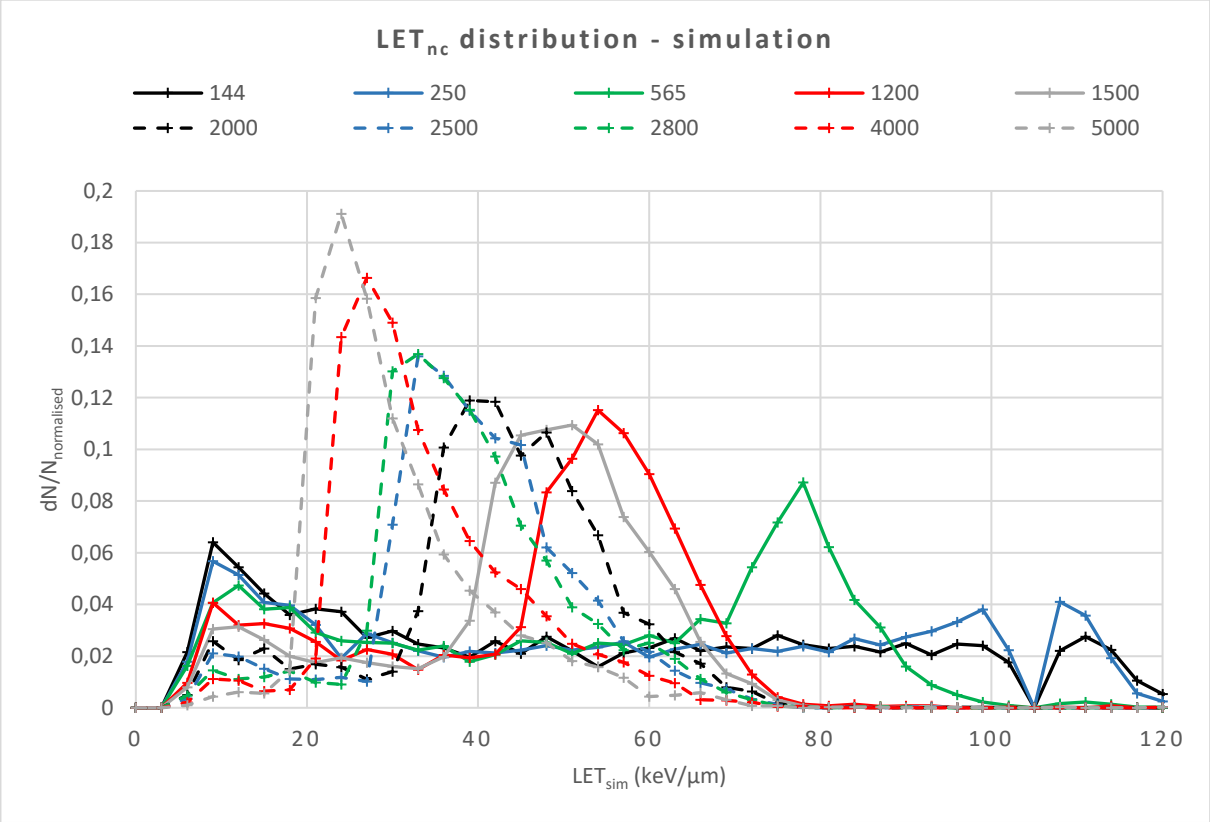

Figura 10 *– Distribuzioni di LET_{sim} per varie energie, calcolate attraverso usando la simulazione.*

Un altro fattore da investigare è la risoluzione del Politrack™ nel calcolare con precisione i diametri e quanto questo possa influire sulle distribuzioni di LET_{nc}, perché ad esempio guardando la **Figura 11** si vede che le distribuzioni degli assi sono negli stessi range ma hanno una diversa ampiezza.

In conclusione, nonostante questo lavoro sia stato fortemente influenzato dalla completa chiusura di tutte le strutture di ricerca, è stato possibile trarre alcune interessanti conclusioni ma soprattutto è stato possibile identificare dei punti sui quali è necessario concentrarsi per sviluppi futuri della dosimetria personale neutronica. Per capire se è possibile avere informazioni utili sullo spettro energetico di un campo di radiazioni neutronico usando SSNTD, dunque, sarà utile seguire il percorso tracciato dalle conclusioni di questa tesi. Nello specifico, sarà utile indagare il comportamento dei protoni nel CR-39, la validità del modello interpretativo e gli spettri prodotti, studiare la risoluzione del Politrack™ nel calcolo degli assi delle tracce e infine migliorare il codice per correggere o aggiungere parti in relazione ai risultati dei precedenti studi.

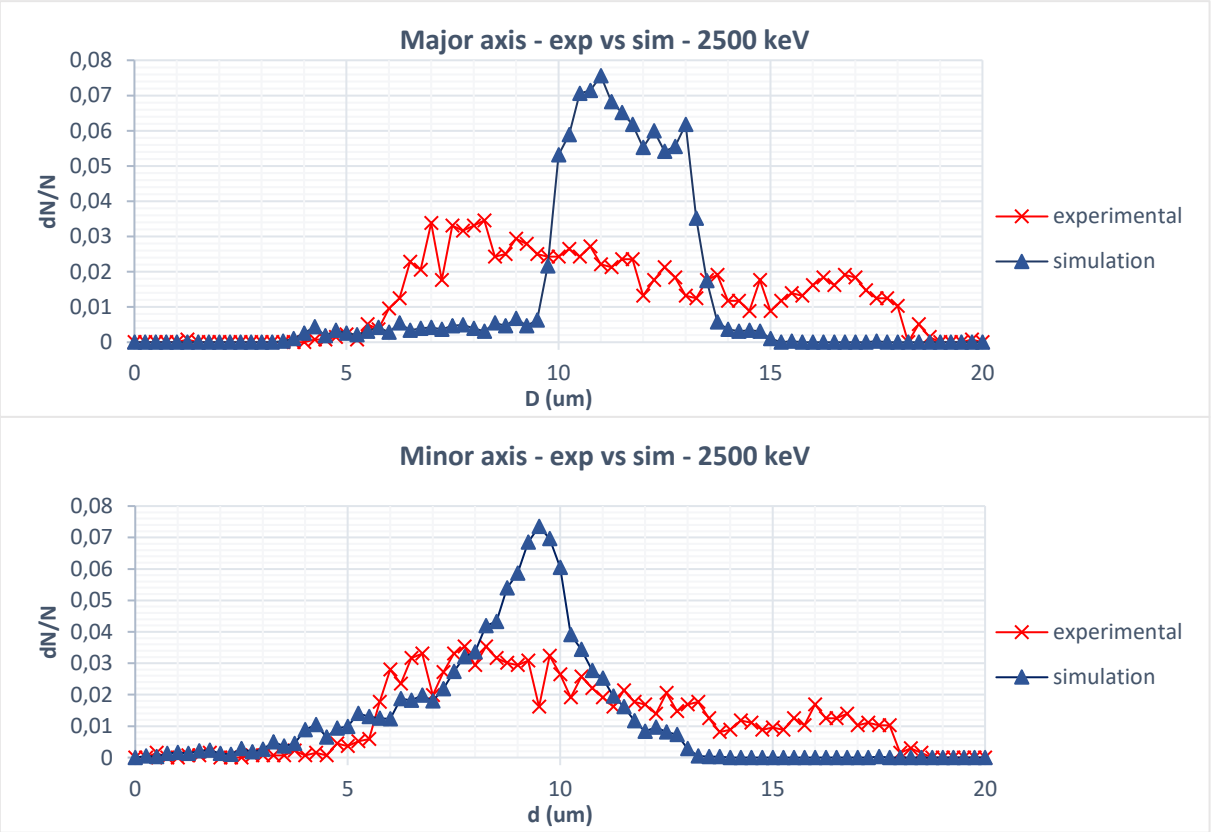

Figura 11 *– Comparazione tra spettri sperimentali e simulati per neutroni primari con un'energia di 2500 keV.*

1 Introduction

The aim of this thesis work is to enhance personal neutron dosimetry performed using Solid State Nuclear Track Detectors (SSNTD) by investigating a way to compensate the dependence of their response on the energy of the incident radiation. The main question of the work is how tracks morphology can give information about the incident neutron field, in order to correct the energy response to have it as flat as possible and then a constant response whatever the neutron spectrum encountered at workplaces. To do so, two different parts of the study have been performed in parallel, both experimental with the analysis of irradiated dosimeters, and computational with the development and use of the GEANT4 simulation software. In this introductory chapter, the context of this work will be presented, starting from the concepts of neutron personal dosimetry, its difficulties and how this thesis work could help in enhancing the measurements.

1.1 Personal dosimetry

In the world, each day, all humans are exposed to ionizing radiations which may cause damage to tissues and DNA. In everyday life, in fact, we are surrounded by weak natural radiations coming from cosmic rays, radioactive elements in soil and stones and other naturally occurring radioactive materials (NORM) present in nature. However, there are some situations in which the amount and type of radiation at which a human being is exposed to, can present risks for their health. For this reason, alongside with the expertise in the exploitation of radiation sources, ways of protecting humans and environment from them have been studied and developed. This is the field of activity of *radiation protection* which relies on both *dosimetry* to measure the quantity of the radiation by a material and *radiobiology* to assess its effect on the living tissues.

It has long been known, in fact, that a serious control on nuclear activities has to be enforced in order to minimize the possible harm that radiations can do to human end environment. To do so, ever since the rise of the nuclear sector, the international community and the nuclearized countries founded public institutions which have the task of supervising the nuclear industry in an independent way. Thus, on the one hand the *International Atomic Energy Agency* (IAEA) promotes the peaceful use of atomic knowledge and oversees the safety and safeguard of nuclear plants[1] of those countries which agreed to the non-proliferation treaty (all countries except India, Pakistan, South Sudan, Israel and North Korea). On the other hand, the single national authorities of these same countries, under the surveillance of IAEA, take care of the everyday supervision of the single nuclear sites and that all the reasonable efforts are put in the

protection of people and environment. Three examples of such institutions can be the *Nuclear Regulatory Commission* for the USA, the *National Inspectorate for Nuclear Safety and Radioprotecion* (ISIN) for Italy, and the *Autorité de Sûreté Nucléaire* fo France. This last institution works together with the *Radioprotection and Nuclear Safety Institute* (IRSN) which has the role of the French public expert on nuclear and radiological risks, helping from a technical point of view the national authority.

This thesis work has been developed as a collaboration between IRSN and Politecnico di Milano; the studies performed have been carried out under the frame of an internship agreement between these two institutions and performed in the laboratories of Fontenay-aux-Roses (Paris) in the *Ionizing Radiation Dosimetry Laboratory* (LDRI), of the Dosimetry Research Department within the Health Division. It is a (little) part of a major effort towards one of the missions of IRSN, which is to enhance dosimetric practices to better protect nuclear workers and in general people exposed to radiations. One of the lines of research of LDRI indeed is to "perform studies and research on external dosimetry measurement and calculation techniques within the field of conventional radiation protection[2]".

This thesis work will focus on workers exposed to neutrons, leaving aside other groups of people, like for example the patients of diagnostics and therapies based on nuclear techniques.

1.1.1 Elements of dosimetry

External dosimetry is the measurement of radiation coming from outside the human body (excluding then the cases when the radiation source is inside the metabolism of a person) and makes use of devices called dosimeters which give a measurable physical variation of a certain quantity in response to a radiation field. From this variation it is possible to find the energy absorbed by the sensitive material of the dosimeter. This way we can define the basic measurable quantity called *absorbed dose* (*D*):

$$D = \frac{d\bar{\varepsilon}}{dm}$$

Where $d\bar{\varepsilon}$ is the portion of mean *imparted* energy by ionising radiation to a portion of volume of mass *dm*; its SI unit system is $J\ kg^{-1}$ or more commonly *Gy*. When considering the effects that radiation fields have on the human body, this simple physical quantity is not enough because the damage depends on the type, or *quality*, of the radiation. This is why in the past the *International Commission on Radiological Protection* (ICRP) prescribed the use of the *quality*

factor Q, a dimensionless quantity, specific for a certain quality of the radiation field, which weights the absorbed dose for the capability of that specific charged particles to have biological effects. The quantity used to assess the biological damage was then the *dose equivalent*:

$$H = D \cdot Q$$

and its unit of measure in the SI is the same of D, but conventionally it is used the sievert (Sv) to distinguish the two. This definition is still sometimes in use, but it has been substituted in the Publication 60[3] and confirmed in the Publication 103[4] of the ICRP (1991) by the *radioprotection quantities* called *equivalent dose* (H_T) and *effective dose* (E).

1.1.1.1 Radioprotection quantities

They make use, to account for the quality differences, of the *radiation weighting factor* w_R and the *tissue weighting factor* w_T and are defined respectively as:

$$H_T = \sum_R w_R D_{T,R}$$

$$E = \sum_T w_T H_T = \sum_T \sum_R w_T \, w_R D_{T,R}$$

where the subscripts are *R* for the specific radiation and *T* for tissue.

As it can be inferred by the equations, H_T is the absorbed dose in a certain tissue weighted by the radiation weighting factor, summed for the different radiation type, if more than one is present. While E is the sum of the single equivalent doses in all the tissues weighted by the tissue weighting factor.

Unfortunately, these quantities cannot be directly measured and used in the monitoring of the irradiated people. To do so, the *International Commission on Radiation Units and Measurements* (ICRU) introduced a third class of quantities, called *operational quantities* which are "aimed at providing a conservative estimate or upper limit for the value of the protection quantities related to an exposure, or potential exposure of persons under most irradiation conditions"[5].

1.1.1.2 Operational quantities

Before presenting them and to better understand their meaning, it is useful to introduce three definitions:

- the *ICRU sphere phantom*: it is a sphere of 30 cm in diameter, composed like the human tissue (76.2 % oxygen, 11.1 % carbon, 10.1 % hydrogen and 2.6 % nitrogen) which is used to simulate the human body with respect to the various reactions that can occur to particles;
- the *expanded* and *aligned expanded radiation fields*: in the definition of the operational quantities it is necessary to represent the real radiation field using hypothetical fields having analogous characteristic. An expanded field is a hypothetical radiation field defined having the same values of fluence and both angular and energy distributions homogenous in a sufficiently large volume, like the actual field in the point of interest. A radiation field is defined as also aligned if instead of being uniformly distributed in the space it is unidirectional, as shown in **Figure 1.1**.

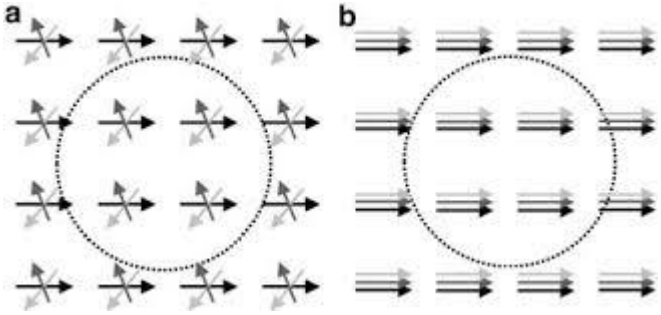

Figure 1.1 *– Diagram of an expanded (a) and expanded aligned (b) radiation fields. The circle is a sketch of the ICRU sphere. (Source: Mattsson, S., & Söderberg, M. (2013). Dose Quantities and Units for Radiation Protection. In Radiation Protection in Nuclear Medicine (pp. 7–18))*

At this point we can explain the three operational quantities:

- *Ambient dose equivalent $H^*(d)$*: defined at a point of interest of the real radiation field, it is the dose equivalent that would be produced in the ICRU sphere at a depth *d*, by the corresponding aligned and expanded radiation field, on the radius vector opposing the direction of incidence of the radiation.
- *Directional dose equivalent $H'(d;\alpha)$*: again defined at a point of the real radiation field, it is the dose equivalent that would be produced in the ICRU sphere at a depth *d* on a radius in a specified direction α, by the corresponding expanded radiation field.
- *Personal dose equivalent $H_p(d)$*: is the dose equivalent in the soft tissue at a depth *d* in a human body; in fact it should be calculated in the human body, but usually specific and standardized phantoms are used for this purpose.[5]

The unit for all of these quantities is joule per kilogram, while their special name is sievert (Sv).

The reason to define three different operational quantities is that it is necessary to account for the different situations and kind of monitoring, which in turns are *area* and *individual monitoring*. While area monitoring makes use of dosimeters fixed in certain positions, individual monitoring is performed using personal dosimeters, which are wearable devices (chest, fingers, near the eyeball) one specific for each worker.
The first ones collect information specific for a certain area; they are useful to keep under control operations and to know if anomalous increases (or decreases) of the radiation intensity occur. They are rarely used as the only dose assessment instrument.
The latter can be of very small dimensions (from few centimetres to millimetres) for passive dosimetry, and are used to understand if the exposition of the person wearing them reaches or even exceeds the limits imposed by regulations. This kind of dosimeters are the most employed in the dose calculations for the single worker.

The depth *d* at which the measurements are performed can be in theory any possible value but there are three different recommended values:

- 0.07 mm for a weakly penetrating radiation (those radiation field which produce a ratio between effective dose and equivalent dose to the skin lower than ten);
- 10 mm for a strongly penetrating radiation (if the same ratio is higher than ten);
- 3 mm when monitoring the dose to the lens of the eye which is a very specific case.

To understand how the operational quantities are used, in **Table 1-1** the single tasks of the different operational quantities are presented.

Table 1-1*: Tasks of the different operational quantities for monitoring of the external exposure. (Source: modified from International Commission on Radiological Protection (ICRP). (2005). Basis for dosimetric quantities used in Radiological Protection.)*

Task	**Operational quantities for**	
	area monitoring	individual monitoring
Control of effective dose (strongly penetrating radiation)	*Ambient dose equivalent* $H^*(10)$	*Personal dose equivalent* $H_p(10)$
Control of skin dose (weakly penetrating radiation)	*Directional dose equivalent* $H'(0,07;\alpha)$	*Personal dose equivalent* $H_p(0,07)$

Through radiobiological studies it is then possible to link a certain level of dose to the possibility of damages to the living tissue and, in turns, to the possible harm to the exposed person. Thanks to this effort, certain very conservative limits may be fixed below which the risk of occurrence of diseases is very low. In few words, there limits are fixed in order to not exceed a certain threshold above which a series of effects certainly occur (these are called *determinist effects*).

For example, to have determinist effects on the eye lens, the limit of absorbed dose is fixed, by ICRP in *Publication 118*[6], to be 0.5 Gy. On this basis, the calculated dose limit for equivalent dose to the lens of the eye is 20 mSv · year^{-1}. People who are supposedly exposed to radiations are then constantly monitored by means of personal and ambient dosimeters in order to prevent the exceeding of these limits. To see a real case, let us take Italy and France, where the situation is the same and there are three categories of workers: the non-exposed one for which the maximum effective dose over the year is equal to 1 mSv, the "B" category whose limit is 6 mSv, while 20 mSv is the limit for the "A" one. If a worker exceeds the 20 mSv threshold, he or she will be prevented from being exposed again over the successive year.

1.1.2 The French situation

The most exposed group of people is the one of workers. To see an example, let us consider France, which is a heavily nuclearized country. During 2018 a total number of 365 980 workers have been monitored, of which 12 884 (the 3,5% of the total) exceeded 1 mSv and only 10 the threshold of 20 mSv, which is the national highest dose limit for annual whole body effective dose. In total, the workers' *collective dose* (which in general is the sum of the effective dose over all the people belonging to a group) calculated over the year is equal to 55,2 man-Sv and the mean effective dose is 0,80 mSv.

***Table 1-2**: Trends from 2015 to 2018 of the distribution of workers by dose class. (Source: Institut de Radioprotection et de Sûreté Nucléaire (IRSN). (2019). La radioprotection des travailleurs - Exposition professionnelle aux rayonnements ionisants en France: bilan 2018.)*

year	monitored workers	collective dose (man-Sv)	mean effective dose (mSv)	distribution of workers by dose class						
				< detection threshold	from threshold to 1 mSv	1 - 5 mSv	5 - 10 mSv	10 - 15 mSv	15 - 20 mSv	> 20 mSv
2015	352 641	65,61	0,76	265 925	72 134	11 795	2 458	317	10	2
2016	357 527	66,71	0,73	266 348	76 442	11 812	2 587	332	5	1

2017	360 694	53,52	0,72	285 856	61 927	10 832	1 894	177	6	2
2018	365 980	55,24	0,8	296 515	56 581	10 457	2 154	259	4	10

In **Table 1-2** it is possible to see the trend from 2015 to 2018 for French workers under radiological surveillance and in **Table 1-3** the division into working field.

***Table 1-3**: Distribution in dose class divided into working field. (Source: Institut de Radioprotection et de Sûreté Nucléaire (IRSN). (2019). La radioprotection des travailleurs - Exposition professionnelle aux rayonnements ionisants en France : bilan 2018.)*

working field	**monitored workers**	**collective dose (man-Sv)**	**mean effective dose (mSv)**	**distribution of workers by dose class**						
				< detection threshold	**from threshold to 1 mSv**	**1 - 5 mSv**	**5 - 10 mSv**	**10 - 15 mSv**	**15 - 20 mSv**	**> 20 mSv**
human and veterinary medicine	221 875	9,5	0,3	190 322	29 776	1 701	51	14	3	8
nuclear industry	86 702	41,51	1,4	57 085	19 401	8 005	1 975	235	1	0
non-nuclear industry	15 772	2,57	0,88	12 864	2 266	532	99	9	0	2
research and teaching	12 414	0,32	0,23	11 002	1 377	34	1	0	0	0
others	9 190	0,93	0,63	7 714	1 262	185	28	1	0	0
indefinite	20 027	0,4	0,16	17 528	2 499	0	0	0	0	0
total	365 980	55,23	0,8	296 515	56 581	10 457	2 154	259	4	10

1.2 Personal neutron dosimetry

In France, of the 365 980 monitored workers, 57 851 (around the 16%) are exposed also to neutrons[7], in places like nuclear power plants, accelerator facilities, research laboratories and even airplanes and space missions. Therefore, it is very important to have reliable personal neutron dosimeters, even if it is very complex to measure doses associated to neutrons.

1.2.1 Difficulties of personal neutron dosimetry

The reasons why neutron dosimetry is much more complex than the photon one, are many:

- The spectra can extend in a very high range of neutron energies for the same workplace, like it is possible to see in **Figure 1.2**, where they span from few meV to tens of MeV, that is ten orders of magnitude.

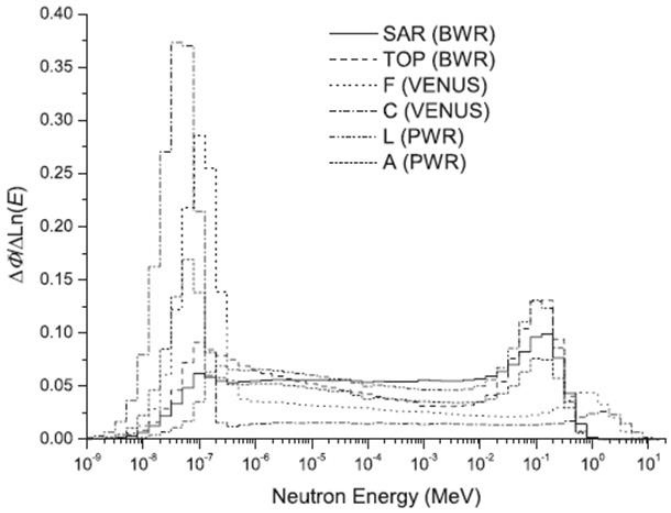

Figure 1.2 *– Energy distribution of the normalized neutron fluence, for a boiling water reactor (BWR located in Krümmel, Germany), an irradiated fuel container from pressurized water reactor (PWR located in Ringhals, Sweden) and the VENUS research reactor (located in Mol, Belgium). (SAR: measurements below the BWR reactor; TOP: measurements above the reactor; F: measurements near the reacto; C: measurements in the control room; L: measurements in the airlock before the containment container; A: measurements in the container). Source: European EVIDOS project (Euratom Framework Program 2002-2005).*

- The very high variability of neutron spectra that can be found in the different working places. In **Figure 1.4** it is possible to see how the energy of the main peak changes.
- A direct detection of the neutrons is not possible since they do not interact by means of electromagnetic force. This means that dosimetry has to rely exclusively on the detection of the secondary particles which are produced by either elastic scattering (protons) or nuclear reactions, depending on the energy and the target material.
- Most of the times, along with the neutron radiation field, also a photon one is present, and it is necessary to discriminate the two when the detector is sensitive to both.
- The conversion coefficient $h^*(10)$ to translate a fluence measure $\Phi(E)$ to a personal dose equivalent $H^*(10)$ estimation is a function of the energy, as illustrated in **Figure 1.3**, differing even of two orders of magnitude at different energies. The conversion coefficient at a fixed energy is:

$$h^*(10) = \frac{H^*(10)}{\Phi(E)}$$

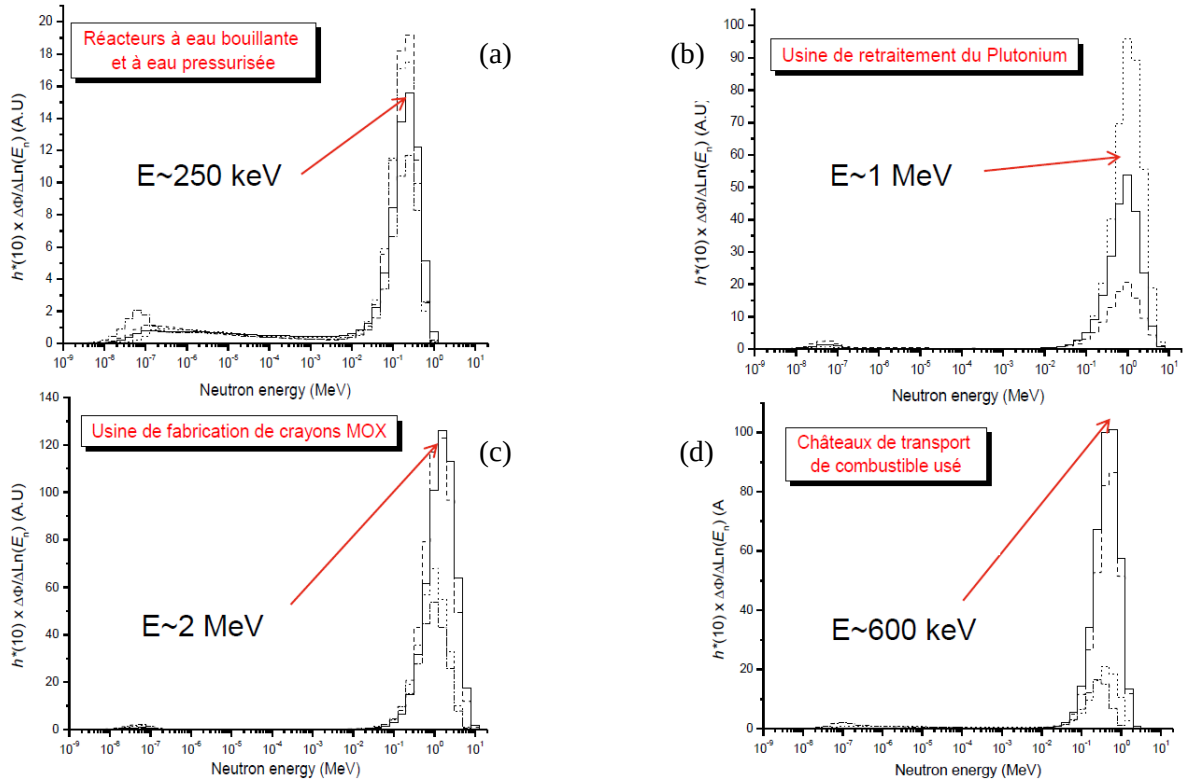

Figure 1.4 *– Dose spectre in working places: (a) pressurized and boiling water reactors; (b) plutonium reprocessing plant; (c) mixed-oxide (MOX) fuel production plant; (c) spent fuel transport casks. (Source: European EVIDOS project (Euratom Framework Program 2002-2005)).*

Moreover comparing **Figure 1.4** and **Figure 1.3** it is useful to point out that the peaks of the workplace spectra are all in the region where the conversion coefficient presents a very evident step of slightly less than two orders of magnitude (10^{-2} – 10^{0} MeV). To correct this problem, it is necessary to know either the response function of the instrument or the energy spectrum of

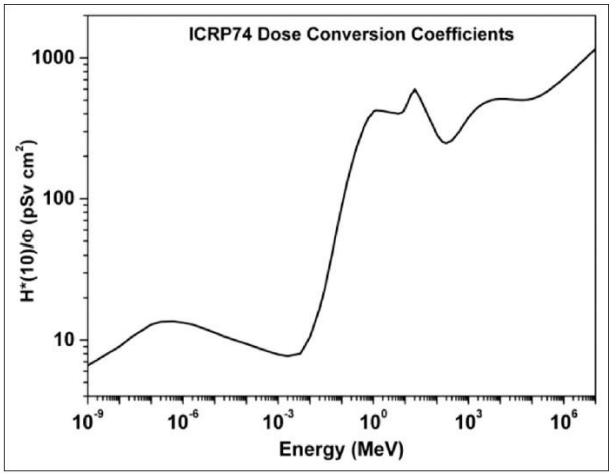

Figure 1.3 *– Conversion factors between ambient dose equivalent and neutron fluence (H*(10)/ Φ(E)) as a function of the energy. (Source International Commission on Radiological Protection. Conversion Coefficients for Use in Radiological Protection against External Radiation. ICRP Publication 74.)*

the neutron field. Another solution could be to develop a dosimeter having a flat dose response as a function of the neutron energy.

Considering all these problems, it is clear how the design of a dosimeter capable of working in all the situation is very complex and it is necessary to fix certain feasibility limits. For personal neutron dosimetry and this thesis work, the focus is on the range from 100 keV to 5 MeV, roughly; the reason for this choice is in the combination of the higher conversion coefficient from flux to dose (cf. **Figure 1.3**) and the high fluxes in this range for working-place spectra (cf. **Figure 1.2** and **Figure 1.4**).

1.2.2 Neutron interaction with matter

To move forward to the techniques and the dosimeters used in personal neutron dosimetry, it is necessary to introduce how neutrons interact with matter and release the energy to be measured.

Neutrons do not interact like heavy charged particles (like protons or ions) through the electromagnetic interaction with electrons and nuclei and, therefore, the direct ionisation and excitation of the atoms of the medium. Instead they can interact only with other nuclei through nuclear reactions. To simplify, while protons "see" a sea of electrons with which they continuously interact, for neutrons matter is empty space with small concentrated blobs of nuclear matter spread around. A neutron passing through a volume containing a number of nuclei has only two options; either it passes undisturbed or it interacts with a nucleus."[8] Thus the detection of neutrons is performed indirectly through the use of these secondary particles. This and what follow are an oversimplification of the real situation, and do not explain plenty of real physical events occurring, because an extensive explanation of neutron interactions goes beyond the aim of this thesis work.

Neutrons' interactions with matter are highly dependent on their energy E_n, and for this reason it is useful to divide them in three classes:

- thermal neutrons: if $E_n < 0.5$ eV, thus if they are in thermal equilibrium with the medium at room temperature, with a maximum probable energy of 0.025 eV;
- epithermal neutrons: if 0.5 eV $< E_n <$ 100 keV;
- fast neutrons: $E_n >$ 100 keV.

To this classes roughly correspond different most probable interactions and then different techniques used for the detection. The two "channels" of interaction mainly used for detection are neutron-induced reactions and elastic scattering. Which one to choose depends mainly on the *cross section* of the interaction, which is a measure of the probability of it to occur at a

certain energy. To use the previous analogy, it is like the area of the blobs that a neutron sees in its path. Cross section is indeed an area and its unit of measure is the *barn*:

$$1\ b = 10^{-24}\ cm$$

At low energies, the most probable classes of interactions are two. One class is the one of neutron captures *(n,γ)*, where a neutron is absorbed by the target nucleus and the exceeding energy is released as a photon. The other is the one of exothermic reactions, where the absorption of the neutron leads to a rearrangement in the nucleus resulting in a new one and a secondary particle, both having a certain *recoil* energy useful for the detection. This kind of reactions have a growing cross section as the energy (and thus the velocity) of the incoming neutron decreases, presenting the characteristic "*1/v*" behaviour.

As the energy grows the nuclear reactions are less probable, and the *elastic scattering* becomes the favourite channel. It consists of a transfer of energy from a neutron to the target nucleus, the amount of which depends on the weight of the target. Elastic scattering actually happens also at low energies, but the resulting recoil nuclei have an energy too low to be detected and to be used for measurements. In Chapter 2 this phenomenon will be explained in a detailed way, for now it is enough to know that this event can be seen like the non-quantistic event of two balls colliding. It is easy to understand that the maximum energy that can be transferred increases if the two balls are of the same dimension (imagine hitting a wrecking ball with a tennis ball). This, combined to a high cross section, is why hydrogen is the most used element when the aim is to detect neutrons[9]; it is even possible that a neutron releases all its energy after an elastic collision and gets backscattered, in a so-called "*knock-off*" event.

The nuclear reactions and the elastic collisions are at the heart of the two main systems used for personal neutron dosimetry: *albedo's dosimeters* and *CR-39 dosimeters*.

1.2.3 Albedo's dosimeter

Due to the high presence of hydrogen in the body, neutrons are easily moderated (meaning that they lose energy until they reach the thermal temperature) and backscattered. The reflected neutrons are called *albedo neutrons* and can be measured by a thermoluminescent dosimeter (TLD) sensitive also to thermal neutrons (along with the X and γ photons). These are passive devices composed by crystals capable of storing the energy released by radiations until they are heated. When this happens, they release photons in a quantity dependent on the absorbed

energy. Combining such a dosimeter with another TLD sensitive just to photons, it is possible to subtract the two measurements to have only the neutronic contribution.

For example, one of the most common TLD used for this application is the LiF one. In fact lithium has two natural isotopes, ^{7}Li (92.41%) and ^{6}Li (7.59%); while the first one is sensitive just to photons, the second one also to thermal neutrons through the interaction ^{6}Li (n,α) ^{3}H. Two LiF chips, one enriched with ^{6}Li and the other with ^{7}Li are then enclosed in a cover (sometimes using also different filters to discriminate different components of the spectrum) and used for whole-body personal dosimeters, like it is shown in **Figure 1.5**.

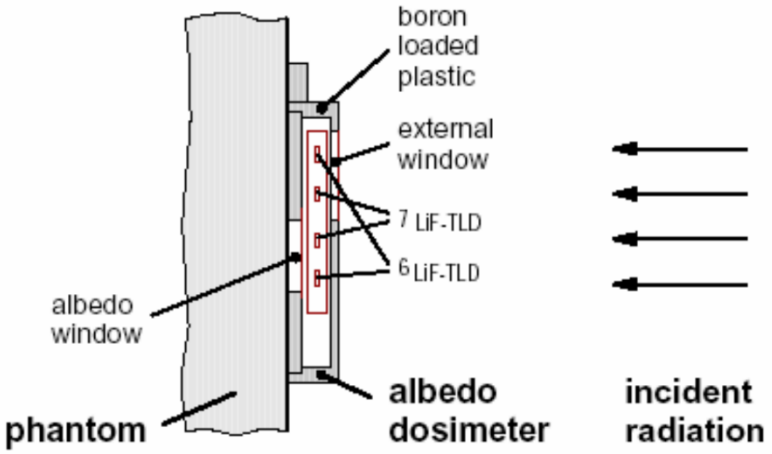

Figure 1.5 *– Schematic drawing of an albedo neutron dosimeter consisting of a boron plastic encapsulation and a card containing two chips each of 6LiF and 7LiF. (Source Errico, F. (2007). Neutron dosimetry. 1–24)*

After the reading, the information stored inside TLDs is lost and they can be re-cycled and re-used. Although this can be seen as a disadvantage, the most relevant problem is that the response is almost flat from thermal energies to around 10 keV, and then it lowers as energy increases. This means that their employment is highly dependent on the energy spectrum of the field to be measured. Thus, this implies that such dosimeters need to be calibrated at the workplace where they are used and under the condition that these neutron fields do not change much over time.

1.2.4 Solid state nuclear track detector (SSNTD)

These detectors are polymeric materials sensitive to neutrons like the cellulose nitrate (called LR115), and the *poly-allyl-diglycol carbonate* also called *CR-39*, the one used in this thesis work. When neutrons interact with SSNTDs, they produce recoil nuclei (for example protons or alpha particles) through both elastic scattering and nuclear reactions, which damage the polymeric chains and produce a *latent track*. After the irradiation, a chemical etching is performed which attacks the latent tracks at a higher velocity than the rest of the material. This

chemical treatment consists in a bath of a specific chemical reactant, for example of sodium hydroxide for CR-39, as performed in this work.

Due to this difference in etching rate, the dosimeters show a series of holes, at the end of the chemical treatment, whose dimensions are related to the energy released by the secondary particle. In fact, the etching velocity of the latent track depends on the local energy deposition, while the etching velocity of the bulk depends only on the bath characteristics, thus it is constant over the whole process. These dosimeters are then read by a device capable of finding the holes through an optical system, measure their features and calculate on this basis one of the operational dosimetric quantities. The Politrack^{TM}, designed by the company Mi.am S.r.l. in collaboration with the Department of Energy of Politecnico di Milano is one of these devices.

The great advantages of SSNTDs are that they are not sensitive to photons, cover a large range of neutron energies if combined to proper radiators and, once they have been etched, information does not degrade over time. On the other hand, the final information is dependent on the etching process and, most of all, on the initial characteristics of the material and the manufacturing process. This means that the level of background can be very high, variable between different dosimeters and thus increase the lower limit of detection.
Other important disadvantages are *ageing* and *fading*, which refer to a decrease in sensitivity over time respectively before and after the irradiation. These effects are ascribable to a decrease in the etching rate of the tracks due to a partial repair of the latent track[10]. To prevent fading and ageing the dosimeters are stored in refrigerators (higher temperatures facilitates the occurrence of restoring chemical reactions) and analysed as soon as possible after the irradiation.

The CR-39 dosimeter will be described in deeper detail in Chapter 2, but to move forward in this introductory discussion it is useful to underline why this specific dosimeter has been chosen for this thesis work: it can store an information about the energy released by the particle.

In fact, the Politrack^{TM} system calculates, using an algorithm, an estimation of the *linear energy transfer* (LET_{nc}) which is the energy divided by the path inside CR-39, starting from the geometrical characteristics of the tracks seen by the device's optical system (cf. **Figure 1.6** for an example of what Politrack^{TM} "sees").

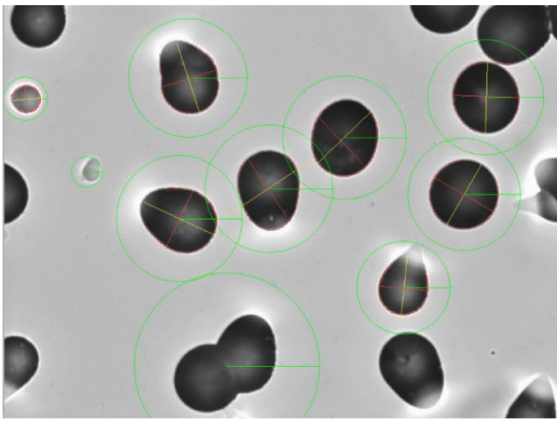

Figure 1.6 *– Tracks as they are seen by the Politrack™ system.*

The basic idea of this work is to investigate whether it is possible to link the LET distribution assessed by Politrack™ to the energy spectrum of the neutron field. It is not immediate because the output information is related to the secondary protons, which can be produced at any energy and any recoil angle. In addition to this, a variety of events can happen during the etching process resulting in a deterioration of the useful information.

1.3 Goal and structure of the work

In few words, the goal of this thesis work is to understand if a rough spectrometry using CR-39 is possible, in order to compensate for the variation of the conversion factor (**Figure 1.3**) in the energy range from 100 keV to 5 MeV.

To do so, the work has been divided into two parts: an experimental one (Chapter 2), focused on the irradiation and analysis of the dosimeters, and a computational one (Chapter 3), during which a software for the simulation of the irradiation has been built.

1.3.1 Experimental part of the study

The aim of this part of the thesis work was to understand the degree of precision of the system, because a mandatory request to reach the final goal is to have an uncertainty on the estimation of the LET of the tracks low enough to let us distinguish the different contributions to the spectrum. To do so, the initial plan was to irradiate dosimeters using:

- Monochromatic protons at different energies at the MIRCOM facility (Ion microbeam for the radiobiology of intra and intercellular communications). The reason for this irradiation was to study the capability of the system to distinguish different proton energies and to test the simulation built on this preliminary situation, since protons have a behaviour in CR-39 much more predictable than neutrons because the energy and

angle of incidence would be perfectly known. This preliminary experimental campaign is an indispensable first validation before moving to the more complex case of neutrons.

- Monochromatic neutrons at different energies at the AMANDE (Accelerator for metrology and neutron applications for external dosimetry) facility, to see how different neutron energies may give different LET spectra and again to test the capability of the Politrack™ system to estimate the LET, compared to the expected ones obtained by simulations;
- Non-monochromatic neutron fields using conventional calibration sources like AmBe, bare ^{252}Cf, and ^{252}Cf moderated with heavy water, to finally see the behaviour of the simulation with respect to a broad spectrum of energies.

Unfortunately, as a result of the SARS-CoV-2 pandemic of 2020, these facilities have been shut down during the months this work has been performed. In Chapter 2 will be presented the solutions to this problem and how the initial irradiation plan changed, together with the dosimeters actually used for the study, coming from previous irradiations performed before this work.

1.3.2 Computational part of the study

The aim of building a simulation for the irradiation of the dosimeter is to understand if, from a purely theoretical point of view, it is possible to link the LET spectra to the energy distribution of a neutron irradiation. To do so, a C++ toolkit, called GEANT4, has been used to build an application capable of reproducing the LET assessment of the Politrack™, by producing a theoretical LET_{sim} (the name that will be used from now on to indicate the LET simulated) distribution.

This simulation tool developed for this work has the ability to follow the history of each particle (primary neutrons and secondary protons) from the production moment to its end. Once a proton has been produced, the program identifies if it is capable of leaving a track, then calculates the theoretical end of the track and integrates the energy, giving at the end of the process the linear energy transfer (this whole process will be explained in detail in Chapter 3).

1.3.3 Final part: comparison of the data

The final part of the work consists in comparing experimental and simulation data to understand if the rough spectrometry hoped can be reached, and, if not, how to correct both the dosimetric

system and the simulation in order to achieve it. Such a conclusion can be useful to prepare future studies to move forward in the field of personal neutron dosimetry.

2 CR-39 dosimeter and Politrack

In this chapter the whole dosimetric system will be explained, starting from the detection system. Thus, the process of track formation will be presented along with the etching process and how the LET can be calculated through their morphology. Then, the device performing the last task cited, namely the Politrack^{TM}, will be described in detail: from its hardware to the software which performs the track analysis. This first part is crucial to understand all the experimental analysis performed for this work and also the simulations, as the code will try to reproduce a real irradiation. At the end of the chapter, the calibrant method will be presented along with preliminary studies performed.

2.1 The detection system

The solid-state nuclear track detector used for this thesis work is composed of two different parts, both with an area 25 x 25 mm^2, which are:

- the passive detector made of poly-allyl diglycolic carbonate $(C_{12}O_7H_{18})_n$ commonly known as CR-39 or PADC, of a thickness of 1.5 mm;
- a radiator made of poly-methyl methacrylate $(C_5O_2H_8)_n$, commonly known as PMMA, of a thickness of 10 mm. Its purpose is to enhance the signal by the production of secondary particles in a thickness much larger than it would be otherwise. Moreover, when its depth is 10 mm, it is the one recommended for the estimation of the operational quantities *ambient dose equivalent* $H^*(10)$ and *personal dose equivalent* $H_p(10; \alpha)$ in case of strongly-penetrating radiation.

This dosimetric system is based on the damage that primary or secondary particles produce to the polymeric chains in CR-39 with the formation of the latent tracks. The successive etching process enlarges the tracks, enabling a scanning process through a microscope, image acquisition system and analysis software using Politrack^{TM}. Each of these steps will be seen in detail in the following.

2.2 Track formation, etching process, and LET_{nc} calculation

As already introduced, the primary event necessary for the detection of particles, is the ionization and excitation of the molecules of the detector; this is why neutrons are detected only indirectly after the production of a secondary. In the energy range considered for this work, the

main interaction occurring is the elastic scattering between neutrons and hydrogen particles (cf. **Figure 2.1**).

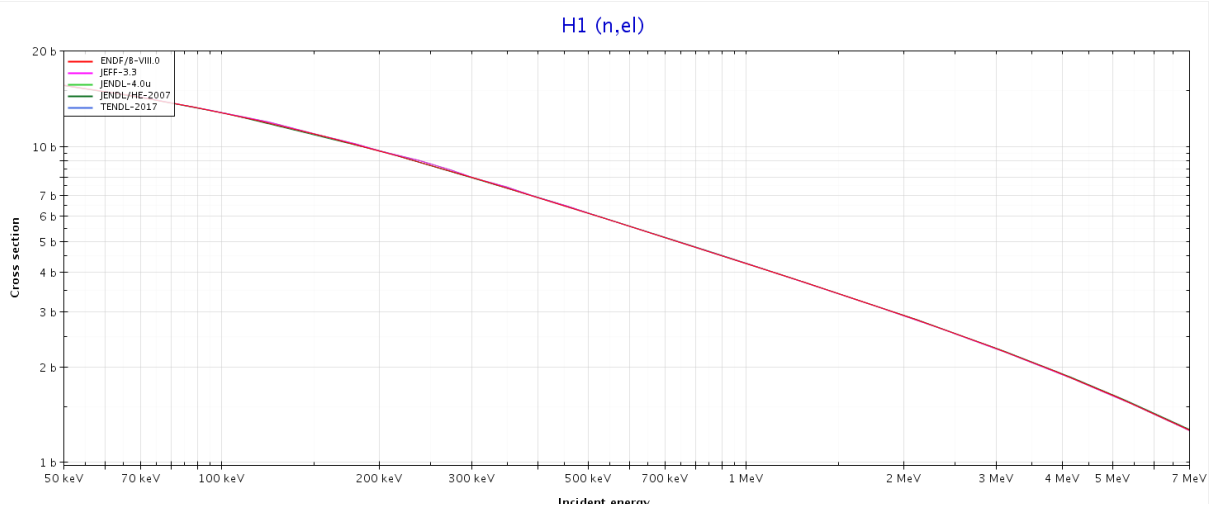

Figure 2.1 *– Cross section of neutron-induced elastic scattering with H in the energy range of interest. (Source: http://www.oecd-nea.org/janisweb)*

Considering the elements composing both detector and whatever radiator (H, C, O), the interaction with probability of occurring comparable to that of elastic scattering on hydrogen, is again elastic scattering on O and C[11].

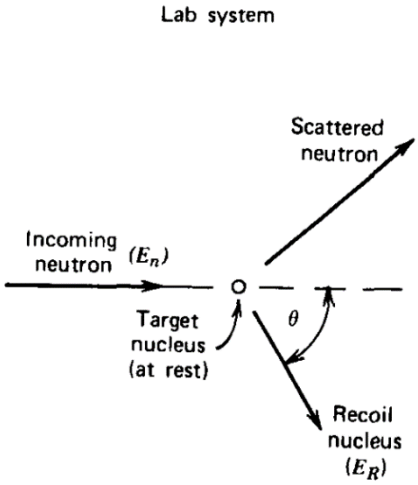

Figure 2.2 *– Schematization of an elastic scattering between an incoming neutron and a genereci nucleus at rest in the laboratory reference frame. (Source: Knoll, G. F. (2000). Radiation Detection and Measurement, Third Edition)*

This reaction is a rather easy way to model mathematically, and the energy of a recoil nucleus E_R having atomic number A, after a collision is:

$$E_R = \frac{4A}{(1+A)^2}(cos^2\theta)E_n \qquad (2\text{-}1)$$

Where E_n is the energy of the incoming neutron and θ is the recoil angle (cf. **Figure 2.2**). The recoil heavy nuclei have a lower maximum energy than the one of the primary particles, and just a few of them, because the production probability distribution as a function of energy has a continuous distribution form the neutron energy, down to 0. Thus, considering the highest possible energy of the secondary particles and the correspondent range inside CR-39 (cf. **Table 2-1**), in the energy range of interest for this work, recoil protons would travel much more than carbon and oxygen, which on the contrary have a maximum path not too far from the detection limit of 1 µm, as we will see in the following.

***Table 2-1**: Maximum fractional energy transfer and range supposing the energy of the neutron to be 5 MeV in CR-39 in neutron elastic scattering. (Source: modified from Knoll, G. F. (2000). Radiation Detection and Measurement, Third Edition)*

target nucleus	atomic number A	$\left.\frac{E_R}{En}\right\|_{max} = \frac{4A}{(1+A)^2}$	maximum range [µm]
H	1	1	281.78
C	12	16/25 = 0.640	> 4.50
O	16	64/289 = 0.221	> 2.15

For this reason, it is a very good approximation to consider just recoil protons in the following of this work.

2.2.1 Latent track formation

Once protons have been produced, they continuously release energy through electromagnetic collisions linked to Coulomb force with electrons and nuclei in the surrounding material. Even if these are point interactions, they constantly happen, such that the situation is described in terms of the continuous *collisional linear stopping power* S_{coll} defined as the energy loss in average *dE* per unit distance travelled *dx*:

$$S_{coll} = -\left.\frac{dE}{dx}\right|_{coll} \tag{2-2}$$

It is expressed through the well-known Bethe-Bloch equation, valid for a charged hadron of speed *v*, mass m_0, and charge *z*, in a medium with atomic number *Z* and number density *N*:

$$S_{coll} = \frac{4\pi e^4 z^2}{m_0 v^2} NZk^2 \left[\ln\left(\frac{2m_0 v^2}{I}\right) - ln(1-\beta^2) - \beta - \frac{\delta}{2}\right] \tag{2-3}$$

Where k is the Coulomb's constant, $\beta = v/c$ is a constant relevant only at relativistic energies, I is the average ionization potential of the target, and δ accounts for the density effect correction, becoming important at high energies and densities. This equation starts to fail at low energies when the velocity of the particle is close to the one of the orbital electrons. The most relevant part of the equation is the $1/v^2$ contribution, which finally defines the behaviour of the whole equation. So, the energy lost by the particle increases with the decrease of the energy, and this phenomenon can be explained, in a simplistic way, because slow protons spend more time close to electrons, therefore the energy transfer is larger. When the energy of the proton is low (under the validity limit of (2-3) a (very fast) continuous charge transfer starts. This whole behaviour is often referred to as *Bragg curve* or *peak*, like in **Figure 2.3**.

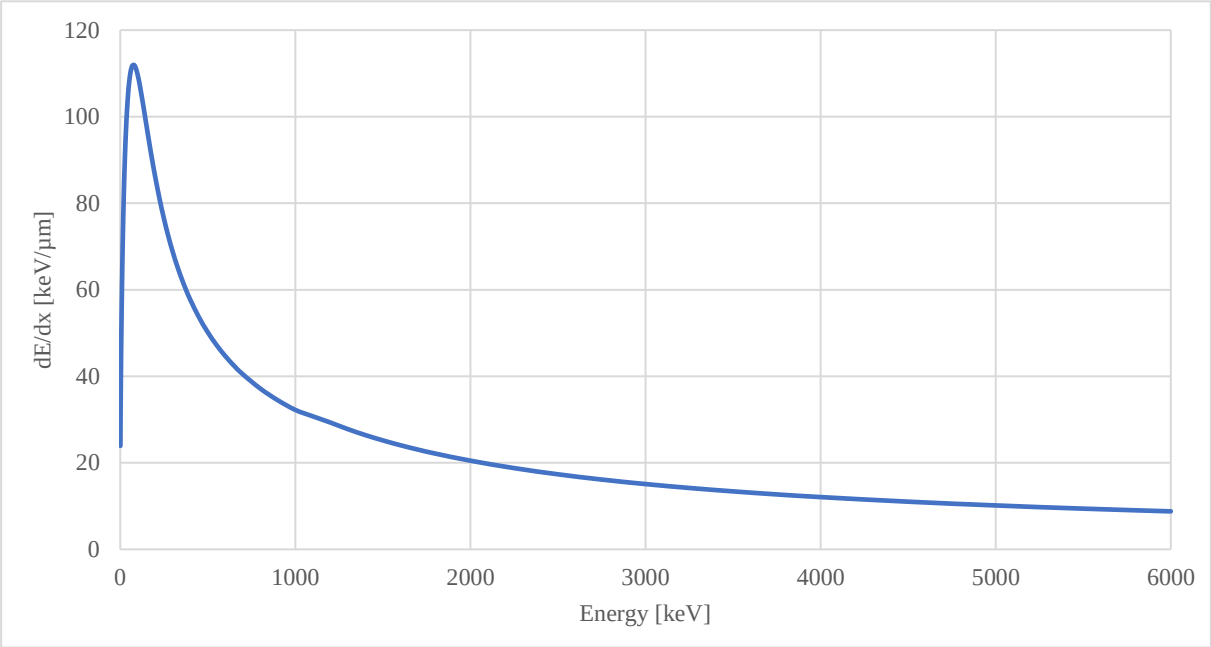

Figure 2.3 *– Proton's stopping power as a function of energy; this is often called Bragg curve. (Source: data from SRIM)*

In general, a part of the particle's energy can be lost through the production of electromagnetic radiation during the deceleration, through a relativistic phenomenon called *Bremsstrahlung effect*; the quantity describing this effect is called *radiative linear stopping power* S_{rad}. This contribution is inversely proportional to the square of the rest mass, meaning that for protons it is negligible. On the contrary, it is not negligible for electrons: protons may produce high energy secondary electrons (called δ rays) which can, in turn, produce Bremsstrahlung radiation, capable of escaping the material. If such a concatenation of events happens, the energy lost by the proton is different from the one transferred to the material. In fact, a new quantity is used to consider this effect, called *linear energy transfer* (*LET*), defined as the portion of energy transferred dE_{tr} to a medium by a directly ionizing radiation per unit distance dx:

$$LET = \frac{dE_{tr}}{dx} \tag{2-4}$$

In other words, the LET is the portion of stopping power transferred to the material. 33In some cases, δ rays may have an energy high enough to be spent far away from the path of the primary proton, and not contribute to the formation of the track. To account for this fact, a new quantity must be introduced, called *restricted energy loss* (*REL*), which is the LET but considering only the energy transfers lower than a certain threshold. For example, defining REL_{350}, one considers only those events where the energy transferred is lower than 350 keV.

These quantities have been introduced because they are useful to formalize and understand the basis of the CR-39 SSNTD. In fact, the formation of tracks starts from the latent track production through the energy release of protons. The ionization of the surrounding material produced by the passage of a heavy charged particle, triggers the break of polymeric chains and the formation of new chemical compounds, called free radicals, which are highly reactive[12]. This process is depicted exemplified in **Figure 2.4**.

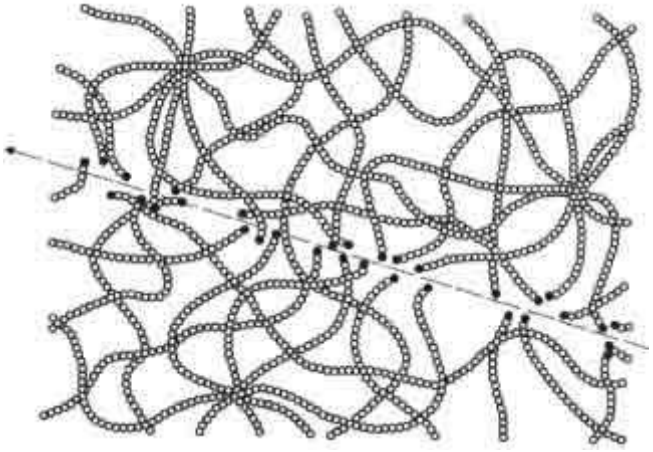

Figure 2.4 *– The breaking of the polimeric bonds by crossing chraged particle; black dots are free radicals and other reactive sites. (Source https://www.bo.infn.it/slim/NTD)*

It is easy to understand that the higher is the LET of a particle, the higher is the damage produced because more and more chains will be broken.

2.2.2 Etching process and track development

Once the irradiation has been performed (for example after the monitoring period for a worker exposed in the case of routine dose monitoring), the dosimeters undergo a chemical etching process. For this work, the chemical treatment has been performed using a 6.25 mol/L aqueous solution of *sodium hydroxide* (*NaOH*) at 98 ± 1 °C for a time long enough (90 minutes) to

remove a thickness around 15 μm of the surface. This length is in this work often referred to as *etching depth* or *h.*, while the etched section of CR-39 is defined as *removed layer*.

Two etching rates characterise the whole chemical process:

- The bulk etch rate V_b, the etching velocity of the undamaged detector's surface, which depends on the specific aspects of the chemical attack, and determines the removed layer of dosimeter's surface *h*;

$$h = V_b \cdot t \tag{2-5}$$

  So, the removed layer is a result of both the bulk etch and the treatment time, where the first depends on the specific characteristics of the plastic material (it may change between different suppliers and even different batches), and the latter is controlled by the user.
- The track etch rate V_t, the etching velocity along the latent track, which is highly related to the energy released by the particle.

Both are usually given in μm/h. While the first one is constant among all the dosimeters in the same bath (calculated through a calibration process, described in Section 2.4), the latter depends on the LET and varies along all the length of the track. Despite this variability, the model used for LET assessment by the Politrack™ and many others consider V_t constant, using a mean value for it. The whole process is governed by the fact that V_t is larger than V_b, meaning that

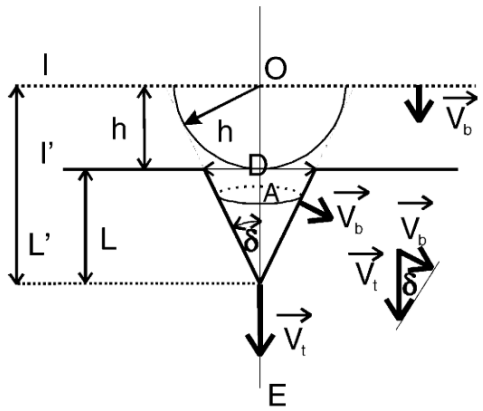

Figure 2.5 *– Geometry of the track development. The incident angle is normal with respect to the detector surface. (Source Nikezic D, Yu N. K., Formation and growth of tracks in nuclear track materials. Materials Science and Engineering R: Reports. 2004.)*

the pit of the track will be etched at a faster rate (V_t) than the walls and the surface (V_b). This leads to the formation of tracks elongated in the direction of propagation of the particle, as

schematized in **Figure 2.5**, where *O* and *E* are respectively the entering and the ending point for the proton in CR-39, and δ is called developing angle. In this image, *I* is the surface of the detector before etching and *I'* is the surface after the etching process. These tracks have geometrical characteristics which, under the right theorical frame, can be linked to the LET of the particle. This is the simplest case of perpendicular incidence and considering V_t constant (a simplification). In this case, a conical track is produced where the hole which can be seen on the surface has a circular form. Obviously, most of the tracks will be given by an oblique incidence.

Figure 2.6 helps us understand the track development in both cases of perpendicular and

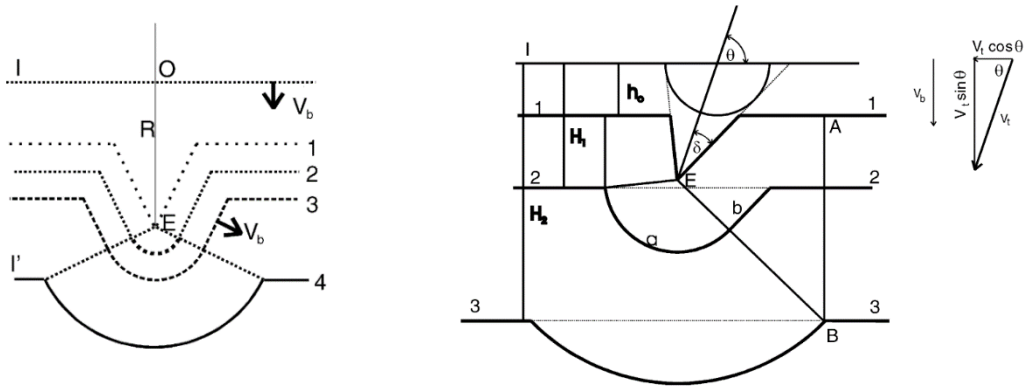

Figure 2.6 *– Phases of track development, from underetched (1) to overetched (4 and the left and 3 on the right) for perpendicular incidence, on the right, and oblique incidence, on the left. (Source Nikezic D, Yu N. K.. Formation and growth of tracks in nuclear track materials. Materials Science and Engineering R: Reports. 2004.)*

oblique incidence. It is also useful to introduce the concept of *overetching*, which is what happens when the etching process continues after reaching the point where the particle stops. The etching rate then becomes V_b for the whole track and the bottom starts to grow with a spherical shape: this kind of tracks are defined as *overetched*. As this phenomenon is more and more relevant in the definition of the shape (thus as the etching proceeds), the geometrical characteristic of the track are less representative of the LET, to the point that an easy discrimination with respect to a defect of CR-39 is less immediate.

Not all obliquely propagating protons can be detected, because the depth of etched track, given by $V_t \cdot t \cdot sin\theta$ where t is the etching time and θ is the *dip angle*, the complementary of the impinging angle, needs to be larger than $h = V_b t$. As it is shown in **Figure 2.7**, the reason is that, as etching progresses, this kind of tracks would be lost (situation "c" in the image). Working with the two relations, the *critical* or *limit angle* is given by:

$$\theta_{lim} = \arcsin\left(\frac{V_b}{V_t}\right) = \arcsin\left(\frac{1}{V}\right) \quad (2\text{-}6)$$

Where the *etch rate ratio* $V \equiv \frac{V_t}{V_b}$ has been introduced.

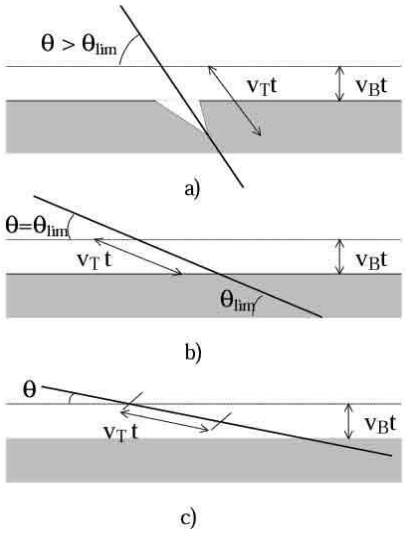

Figure 2.7 *– Track formation for different dip angles, showing what happens above and below the limit angle. (Source: https://www.bo.infn.it/slim/NTD.htm)*

2.2.3 LET assessment through track morphology

Now the discussion will be focused on how the LET is calculated through the morphology of a track. This information is at the heart of this thesis work since these concepts are heavily exploited by both the analysis system of the Politrack™ and the code for the simulations.

A series of models during the years have been developed to describe the growth of the tracks from a physical point of view. A general approach to the theory of track analysis can be complicated and goes beyond the aim of this work. For this reason, from now on, the theory for the calculation of the LET will be described following the same approach and steps as the development of Politrack™. The physical model used in this case is the one developed by Somogyi and Szalay [13] and will better explained in Section 794.3.3.1 as it is fundamental for the code written for the simulations. At this moment, it is enough to know that this model assumes a constant value for V_t, equal to the mean value along the track, and it links V to the final shape of the elliptical section of the hole. This last one is characterized by a major and a minor axis *D* and *d*, which can be measured by an optical system as we will see later in this chapter (Section 2.3.2.1). Moreover, V also depends on *h* because the phase of the track (that is under- or overetched) derive from its position with respect to the removed layer. The

assumption made is, in most cases, satisfying because it does not vary too much along the path of the particle; it may be useful to underline that, under this condition, also *V* is constant.

The dependency exploited to get the final link is the following:

$$V = V(D, d, h)$$

As for as V is concerned, it is calculated through $R = \frac{D}{2h}$ and $K = \frac{1+\left(d^2/4h^2\right)}{1-\left(d^2/4h^2\right)}$ and together with the dip angle, they are:

$$V = \sqrt{1 + R^2(k+1)^2} \qquad \theta = arcsin\frac{K}{V} \tag{2-7}$$

Once *V* is known, it is possible to obtain the LET following the procedure followed by Caresana et al.[13] who started from the use of a practical relation between V and the REL_{350} (cf. page 33 for the definition). This expression holds under the condition that secondary electrons with energy higher than 350 eV do not participate in the formation of the track because they release their energy too far from the path of the particle. REL_{350} is obviously a function of the LET and it is possible to write an analytical relationship between the two, to finally obtain $V = V(REL_{350}) = V(LET)$ which can be written as follows[14]:

$$LET_{nc}[keV/\mu m] = -6.6269 \times 10^2 \cdot V^6 + 6.3379 \times 10^3 \cdot V^5 - 2.4883 \times 10^4 \cdot V^4 + 5.1240 \times 10^4 \cdot V^3 - 5.8254 \times 10^4 \cdot V^2 + 3.4691 \times 10^4 \cdot V - 8.4669 \times 10^3$$

$$\text{for } 4 < LET_{nc} < 100 \text{ or } 1.04 \leq V < 2.1$$

$$LET_{nc}[keV/\mu m] = 1.4132 \cdot V^3 - 22.453 \cdot V^2 + 149.82 \cdot V - 123.06$$

$$\text{for } 100 \leq LET_{nc} < 286 \text{ or } 2.1 \leq V < 6.4$$

$$LET_{nc}[keV/\mu m] = 0.0026 \cdot V^3 - 0.3922 \cdot V^2 + 29.997 \cdot V + 116.81$$

$$\text{for } 286 \leq LET_{nc} \leq 966 \text{ or } 6.4 \leq V \leq 50.7 \tag{2-8}$$

The LET_{nc} is the quantity calculated by Politrack™ (where *nc* stands for "*Nuclear track detector CR-39*") and it is used to indicate this specific procedure of calculation.

Theoretically this expression is a punctual one, which, if inverted, links directly the energy transferred locally by the particle to the track etching rate at that point. However, using a mean value for *V*, the final LET is an average value of the LET along the whole track (cf. **Figure 2.8**

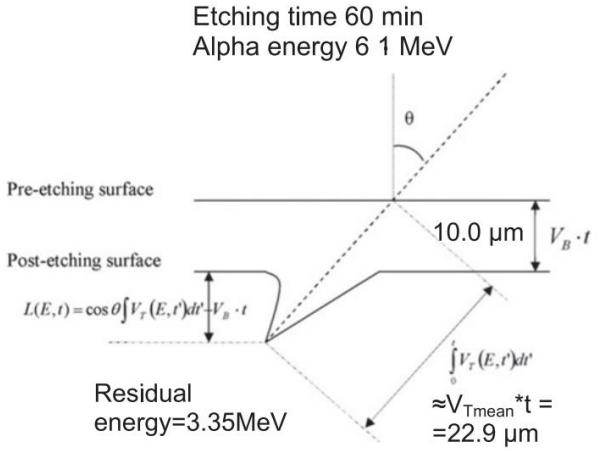

$$MeanLET = \frac{E_i - E_r}{x} = \frac{6100 - 3350}{22.9} = 120\left[keV/\mu m\right]$$

Figure 2.8 *– Representation of the calculation of the mean LET in the case of an alpha particle. (Source: Caresana, M., Ferrarini, M., Fuerstner, M., & Mayer, S. (2012). Determination of LET in PADC detectors through the measurement of track parameters. Nuclear Instruments and Methods in Physics Research, Section A: Accelerators, Spectrometers, Detectors and Associated Equipment, 683, 8–15)*

for a representation of what mean *LET* is).

2.3 The Politrack™ system

Once the theoretical framework has been explained, it is now possible to understand how the analysis system works, its components, and their purposes. Politrack™ is a reader for automatic scanning of SSNTD which can read both CR-39 and LR115 films. It is used for radon and neutron dosimetry, thanks to a complex LET and dose assessment technique, which we will see in the following. **Figure 2.9** shows the hardware of the system.

2.3.1 The hardware

The three main components of this system are:

- A motorized XY cartesian table, fixed on an anti-vibration structure. It has a 200x200 mm wide glass sheet which hosts the dosimeters to be analysed.
- The optical system fixed on a motorized arm which moves along the Z axis to set the focus. It is composed by a microscope whose total magnification is about 4x or 20x according to the objective used, the latter in case of neutron dosimetry. This microscope is coupled to a camera hosting a monochromatic CCD detector and it can investigate

the detector surface with a spatial resolution of either 0.64 or 0.15 μm^2 per $pixel^2$, respectively for radon and neutron analysis. Underneath the glass, an LED diode functions as light source so that the microscope works as a transmission microscope. It can be either green (for CR-39) or amber (for both CR-39 and LR115) and it is chosen to properly match the spectra absorbance of the dosimeters.

- A PC which, through a software described in next session, controls the motion of the plane along X and Y and the motion of the microscope along Z. It also acquires and analyse the images from the microscope and produces the dose assessment along with a series of output data. [15]

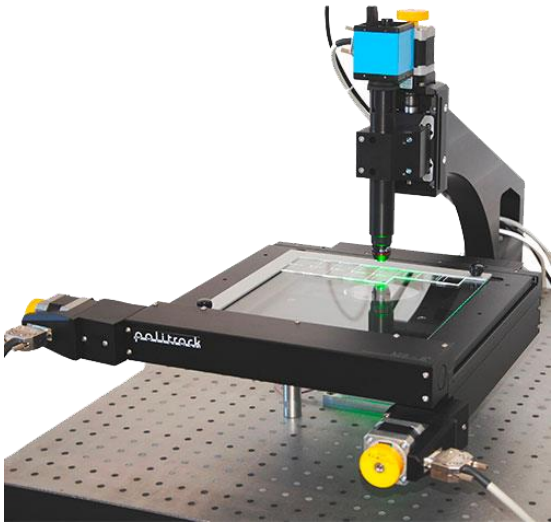

Figure 2.9 *– Picture of the Politrack system where are evident the motorized XY plane, a few dosimeter on it and the optical system. (Source https://miam.it/prodotti/politrack)*

2.3.2 The software

The principal features of Politrack™ software are:

- Autofocusing: it places the microscope between 100 and 200 µm from the surface and executes a series of scans with 10 µm steps to auto determine at which position the edges of the tracks are sharper. Then it runs another series of the same scans but with steps of 2 µm, to obtain the final focus position.
- Possibility to set the scan area of the single dosimeter.
- Detector code scanning for automatic identification of the serial number.
- Morphological analysis of the tracks.

At the beginning of an analysis routine, the user must set a series of inputs:

- neutron or radon analysis;

- CR-39 or LR115 analysis;
- definition of the scan area of the dosimeter, which usually changes between different CR-39 suppliers;
- detector code scanning modality, which again usually changes with the supplier;
- number of detectors to be scanned in sequence, and number of scans to be performed for each dosimeter;
- the value of *h*, which is found through the calibration process (which will be explained in section 2.4);
- settings for the analysis filters, meaning that certain tracks will not be considered as real tacks if they do not respect certain parameters (like if they have an area too small or too big). This concept will be clearer after the next section.

2.3.2.1 Morphological analysis of the track

The analysis is executed in two steps. In the first, starting from a threshold in terms of greyscale (pixels do not have a colour, they have a grey value), each pixel over the threshold is targeted as "1", while the others as "0". On this basis, a new binary image is produced by selecting just the 1s, like represented in **Figure 2.10**.

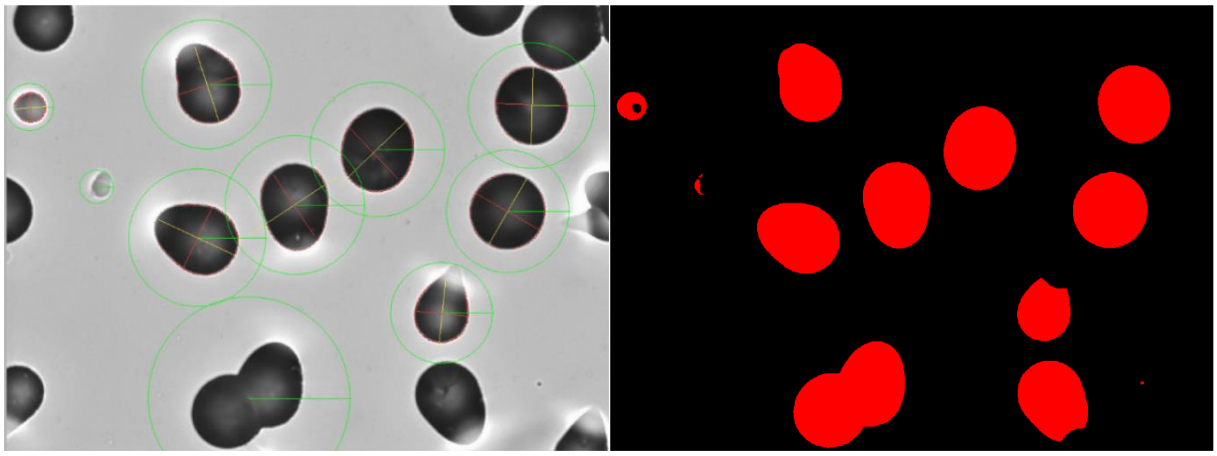

Figure 2.10 *– Image after the morphology analysis on the left and the corresponding binary image on the right. It is possible to see the characteristic elongated elliptical shape.*

The software identifies as tracks all the objects in the binary image and for each the following parameters are calculated:

1.-2. coordinates of the center of mass;
3. track perimeter;
4. convex hull perimeter (the convex hull is the smallest convex polygon containing the pit);
5. holes perimeter (sum of the perimeter of the holes inside a pit);

6. Feret diameter (the maximum distance between two pixels belonging to the pit);
7.-8. equivalent ellipse major and minor axes (the equivalent ellipse is an ellipse with the same area and perimeter as the pit);
9.-10. equivalent rectangle major and minor sides (the equivalent rectangle is rectangle with the same area and perimeter as the pit);
11. hydraulic radius (ratio between pit area and pit perimeter);
12. Waddell disk diameter (diameter of a disk with the same area as the pit);
13. area;
14. holes area;
15. convex hull area;
16. number of holes (inside a pit);
17. track area to image area percentage ratio;
18. elongation factor (ratio between the Feret diameter and equivalent ellipse minor axis);
19. compactness factor (ratio between pit area and the area of the bounding rectangle);
20. Heywhood factor (ratio between the pit area and the circumference of a disk of the same area as the pit)
21.-27. Hu moments from 1 to 7 (these are particular image moments, namely weighted average of the image pixels intensities or functions of them having attractive properties; in the case of the Hu moments considered, these are shift, scale, and rotation invariant);

The second step of the image analysis is on the greyscale image. For each pit, the software sets a circular region of interest (*ROI*) centered on the center of mass and having a radius equal to the Feret one. The software then scans from the center of the ROI to the edge (the user can set also to do the contrary) and, when it finds a contrast of 100 or higher in term of grey scale, it sets it as the border of the pit. At this point, the algorithm performs an elliptical fit and the following parameters are calculated:

28.-29. coordinates of the center of the fitted ellipse;
30.-31. major and minor axes of the fitted ellipse;
32.-33. area and perimeter of the fitted ellipse;
34. mode of the gray scale inside the track;
35. mean of the gray scale inside the track;

36. residual (distance among the track contour points and the ones of the fitted ellipse; it is an index of the goodness of the fit itself);
37. sharpness (ratio between the fitted ellipse area and the one obtained through the same procedure but using a threshold equal to a half of the previous one).

All these parameters are the output for each track and are the ones useful to set the filters. For example, a parameter often used is the *residual* which represents how much a pit's contour is close to the ellipticity, the lower the closer. The user can set a certain threshold, above which the tracks are neglected, eliminating tracks which will almost surely be background or defects. These filters are indeed used to discriminate the real information from the background of the dosimeters.

At the end of the analysis the Politrack™ produces three different files:

- *.trk format file*: it contains all the parameters already enlisted for each of the tracks, even to those which do not pass the filters. This file is produced to store all the information of an analysis, not to perform it again in future and to use this information with other software than the Politrack™'s. The same could be done storing the images taken by the device, but this way the information to store would weight too much;
- *Excel format file*: it contains a subset of the data chosen by the user and data for each reading, like the identification number of the dosimeter, the different values of focuses, the track density, the dose assessment and so on.
- *out.dat file*: a file which record all the activities of the scanner.

Finally, the Politrack™ contains a package of graphical tools which can post-process data from an analysis (downloading it from a .trk file), as in **Figure 2.11**. It is in fact possible to put filters and look at distributions and correlations of the various tracks' parameters.

2.3.2.2 LET_{nc} calculation

The LET_{nc} is assessed starting from the major and minor axis of the fitted ellipsis, which the algorithm calculates as just explained, and following the procedure explained in section 2.2.3. It is then displayed through the *LET Spectrometry graph tool*, (cf. **Figure 2.11**, first graph), making use of *V* and *h*. The user can select a .trk file to analyse and the software will display the LET_{nc} distribution either using the input *h* value ("runtime mode") or a value inserted a posteriori in the tool ("recalculation mode").

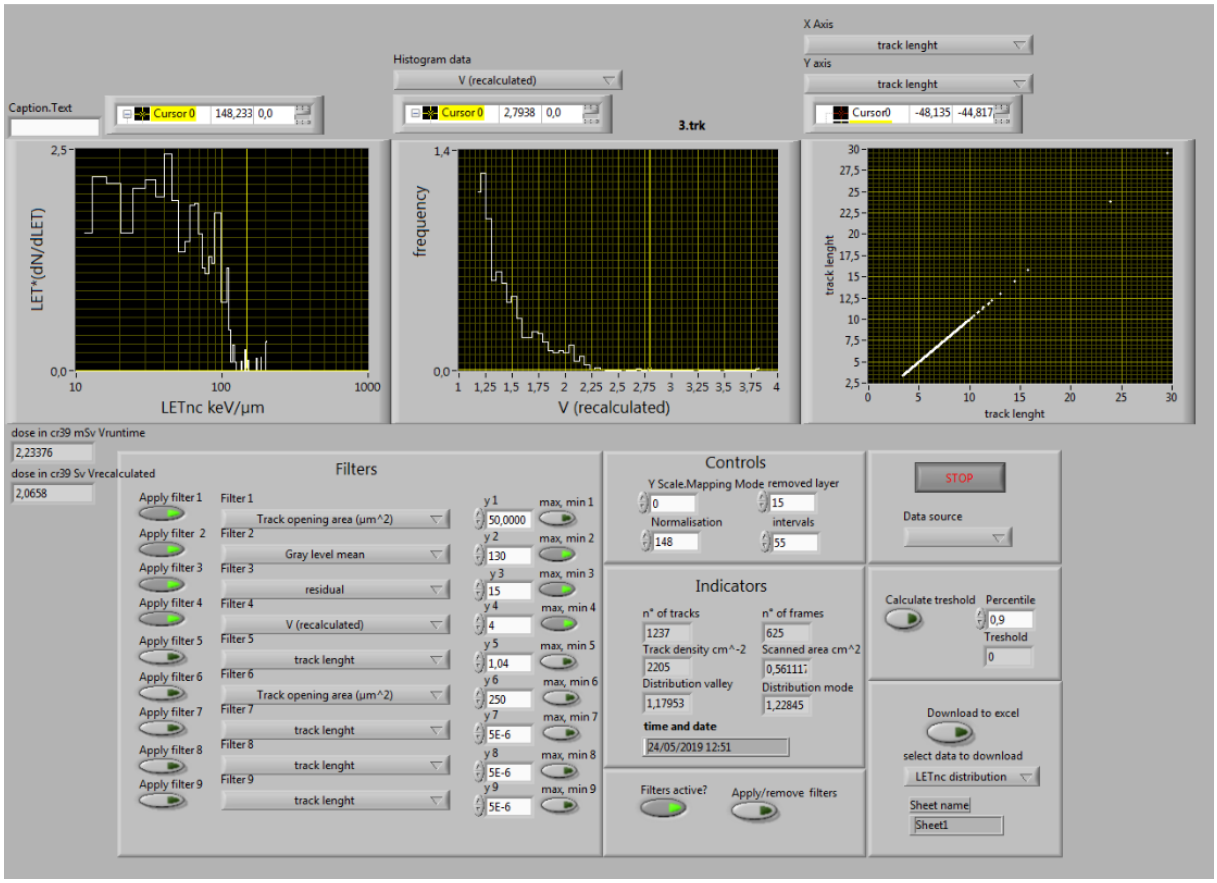

Figure 2.11 *– Politrack™ software analysis tool. On the upper part of the screen the graphs, on the lower the possible filters along with other controls and data.*

For this work, the post-processing of the data has been performed using the Excel software and applying the same equations that Politrack™ does for each track. This has been necessary because of the outbreak of the SARS-CoV 2 pandemics.

2.3.2.3 Equivalent dose assessment

Finally, probably the most important feature of the Politrack™, it is possible to have an estimation of the equivalent dose *H*, through the conceptual steps of the works of Caresana et al.[13], [16]. This is the key feature when Politrack™ is used for individual neutron dose monitoring. It is necessary anyway to underline that this work focuses only on the LET assessment, and this feature is presented just for the sake of completeness.

To obtain the equation for the equivalent dose, it is necessary to start from the definition of absorbed dose *D* (cf. section 1.1.1) and how it is calculated in the case of a charged particle impinging at an angle θ on the surface of a material with density ρ and area *A*:

$$D = \frac{\varepsilon}{m} = \frac{\int_0^x \frac{dE}{dx} dx'}{\rho A l} = \frac{\langle \frac{dE}{dx} \rangle x}{\rho A l} = \frac{\frac{\Delta E}{\Delta x} \frac{l}{cos\theta}}{\rho A l} = \frac{\overline{LET}}{\rho A \, cos\theta} \qquad (2\text{-}9)$$

where *x* and *l* are respectively the length of the track and the material thickness affected by the deposition of the energy.

Here pass from the integral of the *collisional stopping power* along the length of the track, through its mean value $\langle \frac{dE}{dx} \rangle$, to finally the total energy lost divided by the path in the material. The last equality between $\frac{\Delta E}{\Delta x}$ and $\overline{LET}$ (expressed in keV/µm) is not true in principle, because does not consider the secondaries losing energy through Bremsstrahlung radiation. It is anyway true in our case, because of the low atomic number of the PADC.

The previous equation was specifically for just one particle. If we assume now to have *N* particles impinging on the surface, the dose would be:

$$D = \frac{1}{\rho A} \times 1{,}602 \cdot 10^{-6} \times \sum_{i=1}^{n} \frac{\overline{LET_i}}{cos\theta_i} \tag{2-10}$$

where the index *i* stands for the single *i-th* track, and so the sum is performed on all the tracks. The final step is to multiply this by the ICRP quality factor $Q(\overline{LET_i})$ to have the final equivalent dose calculated through a SSNTD detector:

$$H_{cr} = \frac{1}{\rho A} \times 1{,}602 \cdot 10^{-6} \times \sum_{i=1}^{n} \frac{\overline{LET_i}}{cos\theta_i} Q(\overline{LET_i}) \tag{2-11}$$

This is an approximation of the equivalent dose *H* because:

- certain particles which finally contribute to the dose are neglected, specifically the ones impinging with an angle below the limit angle;
- recoil protons with energies higher than around 10 MeV are not detected, because their LET is lower than 6 keV/µm, not enough to release a track;
- the ICRP quality factors are defined in water as $Q(\overline{LET}_{wi})$, not in CR-39. This means that one needs to convert the $\overline{LET_i}$ into $\overline{LET}_{wi}$, which is the correspondent let in water and then use $Q(\overline{LET}_{wi})$. All this is performed using approximated relations, thus introducing an error factor.

For all these reasons, H_{cr} has to be considered as a response function of the SSNTD representing an estimation of the equivalent dose and, when coupled to a radiator with a thickness of 10 mm, can be used as an estimate of $H^*(10)$ and $H_p(10)$.[16]

At the end of a Politrack™ analysis, the value of H_{cr} is displayed in the analysis tool (cf. **Figure 2.11**) both in runtime and recalculated mode.

2.4 Calibration of Politrack™

The discussion, so far, focused on the calculation of V_t and the use of V in an LET_{nc} assessment, while leaving apart the problem of how V_b is obtained, which is going to be explained in this section. This is what can be considered a calibration for the LET_{nc} assessment. The aim of the calibration, indeed, is to know the removed layer h in order to calculate V_b using the basic relation (2-5).

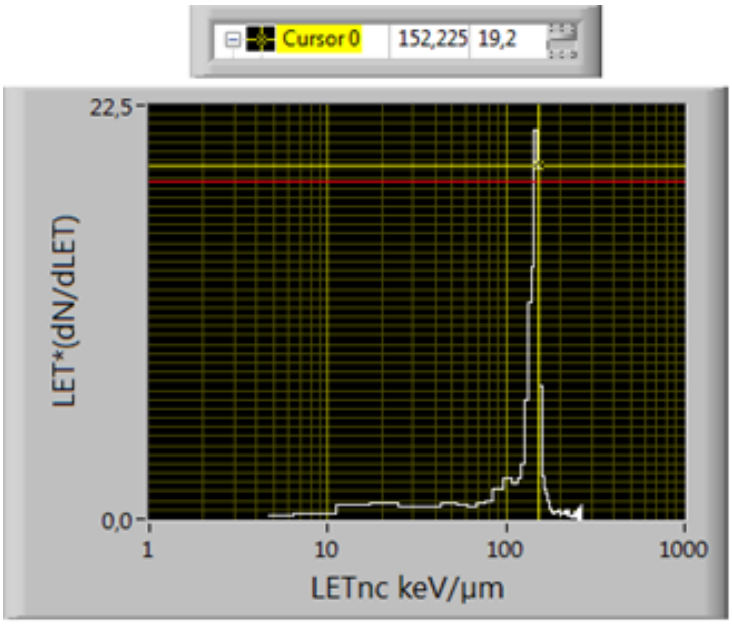

***Figure 2.12** – LET_{nc} distribution produced by a ^{252}Cf source.*

A way commonly used to calibrate this system is to expose the CR-39 detector to a known α particles source with a known LET_{nc} distribution. After this, the calibration dosimeter is etched together with the other dosimeters and then analysed. Since the LET_{nc} distribution is already known, it is sufficient to change the h value in runtime mode in order to make the calibration behaviour match the theoretical one.

For the works performed at the Ionizing Radiation Dosimetry Laboratory (LDRI) of IRSN, CR-39 detectors have been calibrated using a ^{252}Cf α particles source. This isotope has a peak in the emission spectrum of 6.1 MeV, and after an etching time of 90 minutes it should produce a sharp peak in the LET_{nc} distribution around 154 keV/µm (cf. **Figure 2.12**) [13].

2.4.1 Problem faced and proposed solutions

Even if it may seem easy to perform, this calibration method presents two main issues:

- There is not such a source at IRSN's facility, so it is necessary to send the dosimeters for irradiation before every experimental campaign.
- In the past, it happened that for some etching procedures, this method has not worked properly because it was not possible to obtain the expected LET_{nc} distribution form the Politrack™ with any h value. This has led to the loss of the information in the irradiated dosimeters. Moreover, a former study[17] shown that knowing V_b an uncertainty of $\pm 0{,}5\ \mu m/h$ leads to an error in the estimation of the LET up to 20%. This shows the importance of the calibration and the reason of this preliminary study in the context of this work.

Due to these problems, it can be useful to design and test new protocols for the calibration having in mind that they should be at least as reliable as the current one, and that can guarantee to work, not to lose any future experimental campaign. The initial part of the internship collaboration which lead to the development of this thesis work focused on this detail in order to prepare the next irradiation campaign.

One of the solutions could be to use dosimeters which have been exposed to air, meaning that they are irradiated using mainly the ^{222}Rn, which emits α particles at 5.6 MeV. This solution, however, cannot be applied because the dosimeters must be exposed for a very long time in order to have a sufficient number of tracks, leading to a very high ageing and fading risk. In **Table 2-2** are presented examples of dosimeters exposed to air and the relative number of tracks, which are still too few to be used:

***Table 2-2**: Examples of dosimeters exposed to air, showing the irradiation time and the number of tracks.*

Dosimeter ID	Etching Time	Exposure Time	Track number
663	90 min	May 2019-February 2020	104
631	90 min	May 2019-February 2020	68
691	90 min	May 2019-February 2020	133
673	150 min	May 2019-February 2020	71
634	150 min	May 2019-February 2020	105
598	150 min	May 2019-February 2020	153

Note that dosimeters irradiated using ^{252}Cf, as a reference, have a number of tracks higher than 1000 tracks, which is mandatory to have a statistical reliable LET distribution to find the value of h.

Another solution could be to measure the weight of the dosimeters before and after the etching process to assess the difference in mass and so, knowing the density, the etched depth; this is possible using a scale with a resolution of at least 10^{-1} mg. In fact, the dosimeters used for this study, produced by the company TASL[18], weight between 700 and 800 mg, and the weight variations are in the order of the tenths of mg (cf. **Figure 2.13**).

To study the feasibility of this method the original idea was to measure the weight of 24 dosimeters etched for 1h30m and 24 etched for 2h30m, calculate the etched depth and compare it with the one found using the usual calibration method. The first weight measurement was performed just before the etching, while the second was performed the day after, to let the dosimeters dry out for one night under a fume hood. A third measurement was performed at the end of the second day which showed that the weight of the dosimeters was not stable, on the contrary it dropped during the day. Since it is necessary to have a stable weight to assess the etched depth, the weight of 12 dosimeters (one for each combination of exposition type and etching time) has been recorder from that moment on for few days to see if there was a clear trend in the time variation and to understand why.

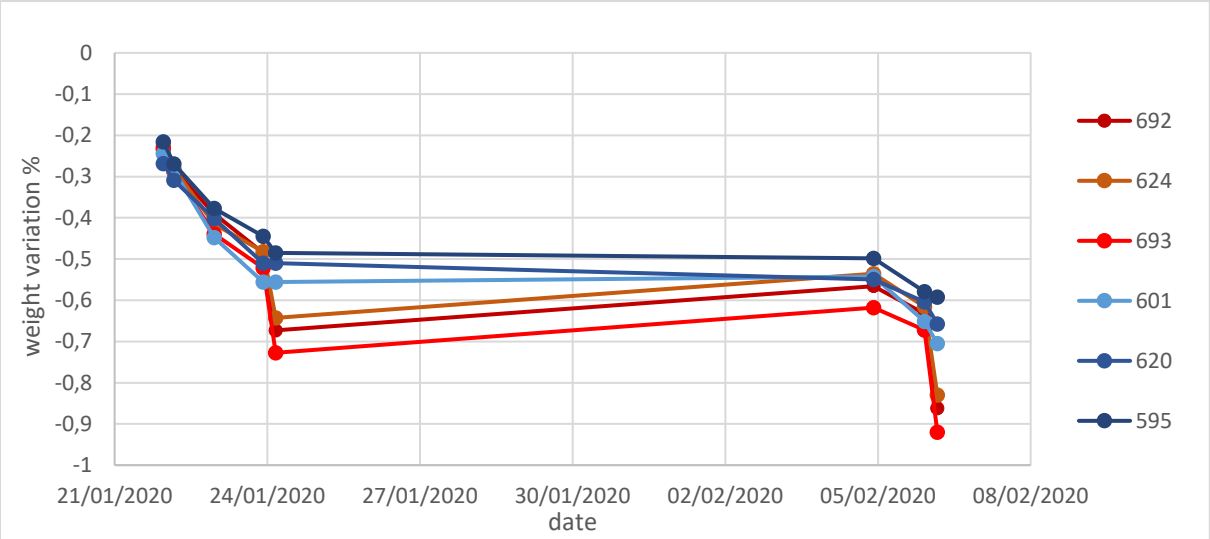

Figure 2.13 *– Time variation of the weight of different dosimeters*

For the next 4 days the weight of all dosimeters kept reducing, confirming a decreasing tendency as it shown in **Figure 2.13**. This phenomenon can be explained by hypothesizing that a residual humidity is present in the dosimeters which keep drying out over time. In fact, to speed up the drying and to investigate further the decreasing trend, two heating process where performed (correspondent to indeed the biggest variations in **Figure 2.14**); the first at 40°C and the latter at 50°C.

It can be shown that this uncertainty of the weight deeply affects the estimation of the etching depth, in **Figure 2.14** the error is plotted defined as:

$$error = \frac{h' - h}{h'} * 100$$

where *h'* is the etching depth estimated with the usual routine (the one with an α source) while *h* is the one assessed using the "weighting routine". In the graph it is possible to see even two dosimeters presentin a very low error, for which however the treatment was the same as the others, meaning that it can also be a casual result.

However, at the end of all this analysis, a problem in the scale was found which produced an uncertainty of cents of mg, depending on the position of the sample on the weighting plate. So while we can be sure that the general trend is the one recorded, meaning a variation of the weight during time (because the uncertainty due to scale problems is lower than this reduction), we cannot rely on these data for a quantitative study.

The conclusion of this preliminary study, which should have prepared the irradiation campaign to be performed at AMANDE and MIRCOM, was to request the use of an α particles source present at the facility of IRSN where this work has been performed.

The source identified was an ^{241}Am source, which decays producing α at an energy around 5.5

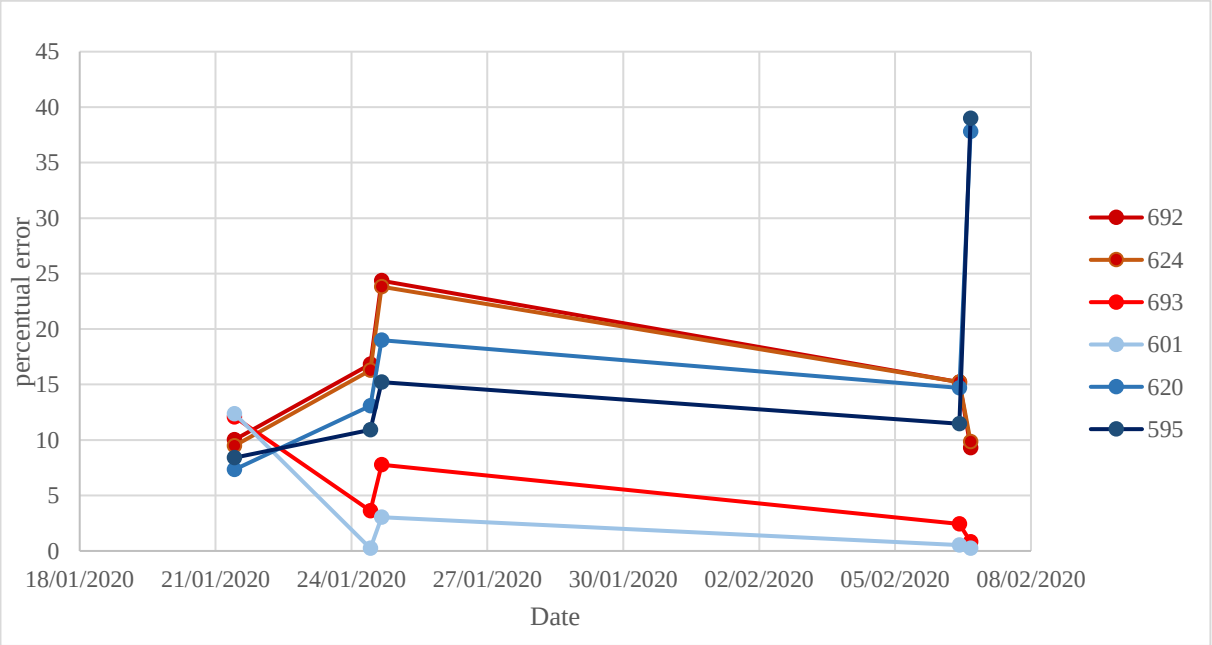

Figure 2.14 *– Variation over time of the percentual error in the estimation of the removed layer.*

MeV. The characterization of the source was yet to be performed, but should have been part of this study, in order to know the expected LET_{nc} distribution.

Unfortunately, due to the SARS-CoV-2 pandemic, the manufacture of the source by the dedicated department within IRSN, the calibration and the irradiation campaign never occurred.

3 Irradiations planned and facilities involved

This chapter will go through the initial irradiation plan, describing which kind of irradiations were thought to be useful for the development of the thesis goal, to then move on what was actually used in the thesis as a response to the shut-down of the irradiation facilities. So, after an explanation of the use of these dosimeters in the work, the discussion will focus on explaining the facilities where the dosimeters have been irradiated and why they have been chosen.

3.1 Goal of the experimental study

In order to better understand the irradiations, it may be useful to remember the idea at the basis of the thesis: use the LET_{nc} spectrum of CR-39 dosimeters produced by the Politrack™ irradiated by neutrons to have an information on the fast component of the radiation field and in the meanwhile build a simulation of the system.

The first question to answer is whether the system is capable of discriminating the protons (the secondaries producing the damage) at different energies and angles, and to which degree of precision. But above all, the key point is to know the uncertainties of the LET estimation performed using the Politrack™ and which parameters can affect this process. Possible cruial parameters can be the incidence angle, the various energies (uncertainty in the estimation can depend on the energy of the particles) and for sure the value of the bulk etchin rate. In fact many complications can prevent the final goal: for example a deviance from the track dynamics physical model or a difference too small in the mean values of LET_{nc} between two proton energies and other unpredictable behaviours.
To test all this, the initial plan was to irradiate particles with monoenergetic protons at the MIRCOM facility (Microbeam of Ions dedicated to the Radiobiology of Intra and Intercellular Communications), using two different energies and three incidence angles. Moreover these dosimeters could have helped in understanding whether the model for the simulations works for this preliminary situation; it has been programmed indeed in order to work both with protons and neutrons. As we will see in section 4.3, the irradiation using protons is much easier to code and this code is then applied, with few modifications, to the irradiation with neutrons. Having experimental data could have indeed helped in validating the basis for the final model.

The logical successive step is to validate the whole study irradiating dosimeters with neutrons. Since the complexity of the final goal, it could be very useful to have the easiest neutron

irradiation possible. This can be performed at the AMANDE facility (Accelerator for metrology and neutron applications for external dosimetry), where it is possible to perform irradiations with monoenergetic neutrons.
In fact, if the final aim is to understand whether different peak energies (cf. **Figure 1.4**) produce distinguishable LET_{nc} spectra, it could help having the simplest case possible.
Furthermore, from the analysis of these dosimeters, important data can be been produced in order to correct and improve the simulation, because they can help understand if there are details to be implemented in the code.

All these irradiations and code implementations are perfomed with a view to the real workplace neutron field. These fields indeed are very rarely well characterised and a calibration of the system is not possible. For this reason, this work aims at coding a simulation reliable enough to produce LET spectra which can then be used to deduce the source of the radiation field for real workplace. To do this it is necessary to rely on the data produced in these monoenergetic facilities.

3.1.1 Initial irradiation campaign planned

Thus the initial plan was to irradiate with two different neutron energies, because it is very time consuming, taking one full day to irradiate for each energy in order to have enough tracks to have reliable LET_{nc} distributions. Along with these dosimeters, the plan was to use

- *background dosimeters*, that is to say dosimeters not to be irradiated but stored and etched together with the exposed ones in order to study the background signal
- *calibration dosimeters*, both using a ^{252}Cf source, to be performed at Politecnico di Milano by prof. Caresana, and the new ^{241}Am source at IRSN, to define the new protocol for the V_b calibration.

The complete irradiation plan is presented in **Table 3-1**. For each of the irradiation condition in the table, the plan was to irradiate dosimeters from two different suppliers, to test a possible dependence of the final results on the initial characteristics of the CR-39 dosimeter.

***Table 3-1**: Initial irradiation plan to be performed for this study.*

facility	particle	type	angle of incidence	etching time	number of dosimeters
MIRCOM	proton	1,5 MeV	0°	1,5 h	4

				2.5 h	4
			20°	1,5 h	4
			40°	1,5 h	4
		2,5 MeV	0°	1,5 h	4
				2.5 h	4
			20°	1,5 h	4
			40°	1,5 h	4
AMANDE	neutron	144 keV	0°	1,5 h	10
		1,5 MeV	0°	1,5 h	10
		2,5 MeV	0°	1,5 h	10
Politecnico di Milano	α (^{252}Cf)	calibration	-	1,5 h	3
				2,5 h	3
IRSN (Fontenay-aux-Roses)	α (^{241}Am)	calibration	-	1,5 h	3
				2,5 h	3
-	-	background	-	1,5 h	5
				2,5 h	5

3.1.2 Development of this study: available dosimeters used

Due to the SARS-CoV 2 pandemic, on 27/03/2020 IRSN temporarily closed its non-essential research facilities[19], including both the laboratory in Fontenay-aux-Roses, where this study and the relative internship were performed, and AMANDE and MIRCOM facilities.

For this reason, the irradiation campaign already planned between the 4th and the 10th of April, where cancelled and the dosimeters could not be irradiated. On the contrary, the irradiation planned has been postponed to a date too far to be included in this work.

To substitute these dosimeters, old ones have been used, which were irradiated and analysed in the past years. The list of these available dosimeters used to perform the experimental study is presented in **Table 3-2**.

Table 3-2: Dosimeters actually used in this work.

Facility	Particle	Energy	Etching time	Removed layer
MIRCOM	proton	1,5 MeV	70 min	unknown
			90 min	unknown
		2,5 MeV	90 min	unknown
AMANDE	neutron	565 keV	90 min	15 µm
		2,5 MeV	90 min	15 µm
		5 MeV	90 min	15 µm
National Physical Laboratory (NPL)	neutron	565 keV	90 min	19,5 µm
		1,2 MeV	90 min	19,5 µm
		2,5 MeV	90 min	19,5 µm
		5 MeV	90 min	19,5 µm

The biggest problem in using these dosimeters is related to the ones irradiated at MIRCOM facility, and the table suggests the reason: the removed layer is unknown. As said in section 2.4.1, the calibration of the dosimeters has been critical in the laboratory where this study was performed, and in this case it did not work. It was not possible indeed to find a value of the removed layer for which the calibration dosimeters have the expected LET_{nc} spectrum. This means that there could have been problems with both the irradiation of calibration dosimeters, and the etching process.

Proceeding from these premises, the dosimeters have been used in this work to test the simulation, trying to find a value of the removed layer which is suitable for all the three combinations of energy and etching time. In fact, if for a specific value of h the distributions of LET_{nc} and LET_{sim} match, it could be a good hint about the potentialities of the simulation and the capacity of Politrack™ to estimate the LET_{nc} with the relative uncertainty.

Nonetheless it is important to remark that the lack of reliable dosimeters irradiated with protons is very negative for this work, since it is not possible to isolate the reasons for eventual incorrections of the simulations or limitations of the dosimetric system.

On the other hand, the neutron-irradiated dosimeters can be considered reliable and have been largely useful for the purpose of this work, as we will see in Chapter 6.

The list of dosimeters used also show that another facility added to the ones initially planned for the irradiations, namely the National Physical Laboratory (NPL) in Teddington (UK).

3.2 Description of the irradiation facilities involved

In the following the three irradiation facilities will be described. Starting from MIRCOM and AMANDE to then move to NPL. This part will be useful to understand how the irradiations in these facilities are performed from a technical point of view.

3.2.1 The AMANDE and MIRCOM facilities

MIRCOM and AMANDE are both located in Cadarache (France) in the IRSN's Neutron Metrology and Dosimetry Laboratory (LMDN), which is the national measurement standards laboratory in the field of neutron radiation for France. Not only they are in the same research facility, but they also share the initial stage, that is the accelerator (visible in **Figure 3.1**)

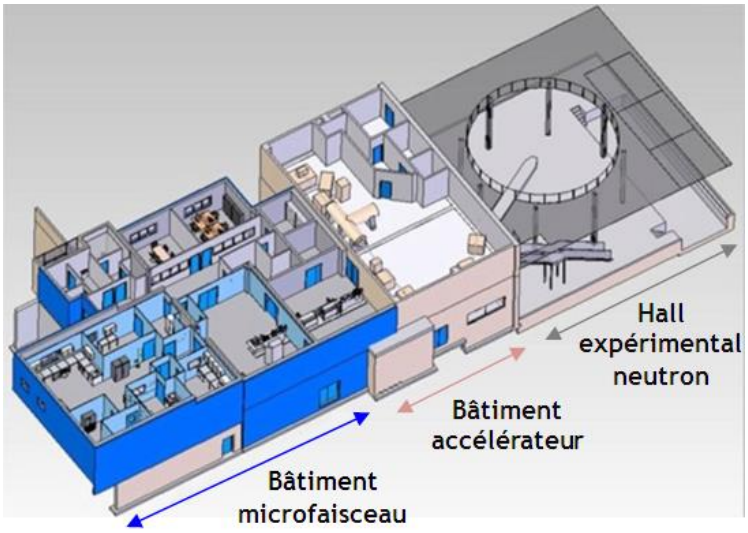

Figure 3.1 *– Facility hosting MIRCOM on the left and AMANDE on the right. (Source https://www.irsn.fr/FR/Larecherche/Actualites_Agenda/Actualites/Pages/2016-02-05-inauguration-installation-MIRCOM)*

The first to be built was AMANDE, commissioned in 2005, followed by MIRCOM which was completed in 2016 and started operations in 2018, following an upgrade of the whole facility (for example two ion sources were added)[20].

For this reason, let us start from the description of this component they have in common and then the two facilities will be described in detail.

3.2.1.1 Ion accelerator

The ion acceleration system is capable of accelerating beam of different ions with energies between 100 keV and 10 MeV both in contiuous mode (<500 eV resolution) and pulsed mode (<4 keV in resolution)[21].

The working principle is quite simple actually, and it all starts from the ion source. Negative ions are extracted at about 30 keV and sent through a 15° injector magnet, which selects the type of ion to accelerate. Indeed the possible ions produced are different, because the ion sources are three (cf. **Figure 3.2**):

- a source of H^- and D^- ions (Z=1), which was historically the first one to be installed for the AMANDE experiment;
- a source of helium ions (Z=2), which was installed, together with the next one, when MIRCOM was built;
- a source based on sputtered cesium, which produces negative ions heavier than bore (Z=5); principally bore itself, carbon (Z=6) and oxygen (Z=8).[22]

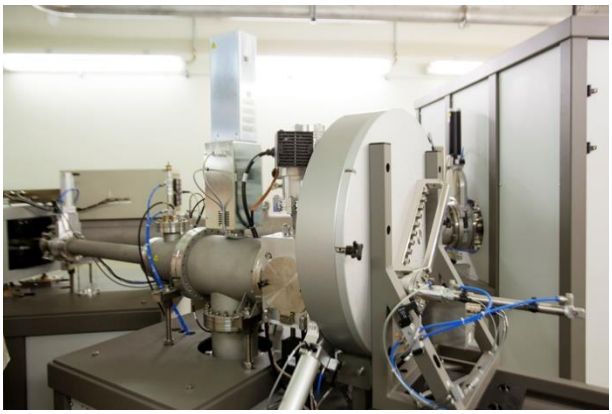

Figure 3.2 *– The system for the production of the initial negative ions, containing the sources. (Source https://www.irsn.fr/FR/Larecherche/outils-scientifiques/installations-moyens-experimentaux/microfaisceau-mircom/Pages/default.aspx)*

After the production and selection of ions, the acceleration stage comes through the operation of a 2 MV Tandetron™ tandem accelerator (cf. **Figure 3.3**). In this system, the incoming negative ions are accelareted towards the middle of the cylindric structure by a high voltage (up to 2 MV indeed). Here, the electrons are stripped from the ions through a nitrogen flow, thus

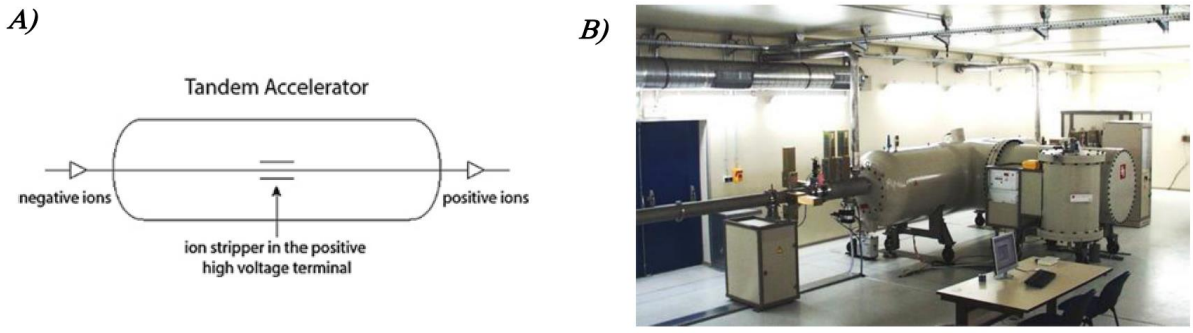

Figure 3.3 *– Tandem accelerator: A) sketch of the general structure; B) a real picture. (Source Bolzonella, M. (2019). Characterization of a passive dosimeter based on a CR-39 track detector for envoironmental and personal dosimetry in neutron mixed fields. Politecnico di Milano.)*

changing their charge. Once they are positive, the ions are repulsed by the same voltage, further accelerating them up to energies of 4, 6, and 8-10 MeV respectively for protons, aplhas, and heaviere ions.[22]

When out of the accelerator, the ions are passed through a 90° magnet. The actual magnets are two: the one circled in red in **Figure 3.4**, leading to MIRCOM, and the one just above in the same image, leading to AMANDE. Both are used to deviate the beam to the right irradiation chamber and for beam-energy stabilization and selection. In addition, the one leading to AMANDE is able to perform an absolute energy calibration[23] of the beam, which selects only the particles with a very specific energy, because AMANDE is used for the calibration of dosimeters and metrology purposes.

The operator then decides which one to turn on, in fact the two experiments cannot work at the same time.
The system up to now is the same for both AMANDE and MIRCOM, from now on the two have their own components.

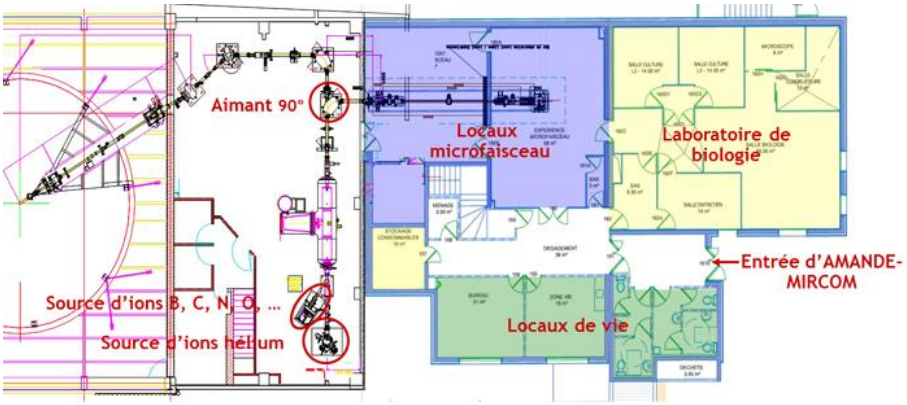

Figure 3.4 *– A part of the blueprint of the AMANDE/MIRCOM facility, where the first experiment is shown only in part. On the left AMANDE's irradiation room, in the middle the accelerator room and on the right the MIRCOM's irradiation rooms (blue), the ambient where biological samples are prepared (yellow) and the operation rooms (green). (Source https://www.irsn.fr/FR/Larecherche/outils-scientifiques/installations-moyens-experimentaux/microfaisceau-mircom/Pages/default.aspx)*

3.2.1.2 MIRCOM facility

Before starting to illustrate the technical part of MIRCOM, and its purpose in this work, it may be useful to introduce its conventional use. The main reason MIRCOM was built and is now operating, is to experimentally investigate the link between the physics of ionising radiation and the events induced by it at a molecular level, to directly and immediately (thanks to the optical system) see the effects on the living tissues. The final goal then is to expand the knowledge in the field of hadrontherapy (treating cancers using heavy charged particles) to increase its effectiveness and decrease detrimental side effects. The precision of this microbeam

indeed makes it possible to decide the number of particles to shoot and precisely target the area of the cell to be irradiated, and on the same time to see directly the modifications induced.

Following with the technical explanation, after the magnet, the beam has an intensity on the order of few µA. A series of collimators reduces the intensity (down to 1.000 - 15.000 particles per second), dimension, and dispersion of the beam, which in turns arrives at a focusing system, composed by four magnetic quadrupolar lenses. The beam obtained after this system can be up to 20 times smaller than previously. Before the extraction, there are an electrostatic deflector and an electrostatic displacement system. The first cuts the beams after either a certain time or number of ions, the latter is able to precisely choose the position of the beam on the target, generation particular irradiation patterns. All this is performed in vacuum and, at the end, a 150 nm thick Si_3N_4 window separates the beam line from the target, which is at atmospheric pressure (cf. **Figure 3.5**).

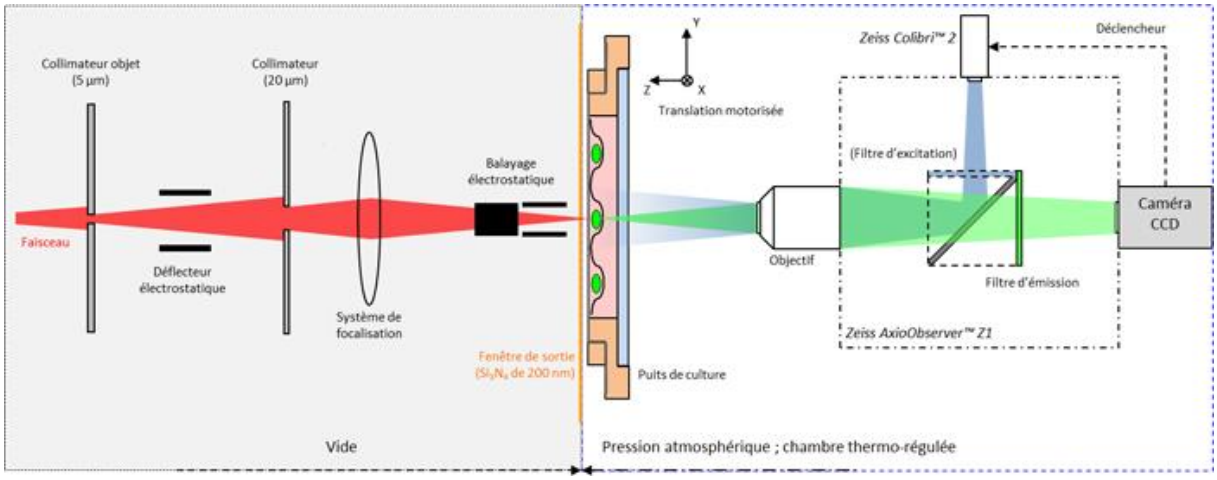

Figure 3.5 *– View of the final part of the MIRCOM's microbeam line, on the left. On the rigth, the the sample and the optical system to see the operations on the sample. (Source: https://www.irsn.fr/FR/Larecherche/outils-scientifiques/installations-moyens-experimentaux/microfaisceau-mircom/Pages/default.aspx)*

On the other side of the window, the sample, placed on a motorized plane, and a microscope are controlled by a specifically developed software, allowing the automation of the operations. One of the specific features of MIRCOM in fact is to perform online videomicroscopy, visualizing the radiation-induced effects occurring on the samples only a few seconds after the irradiation[22]. Although this feature has not been used in this work, it is one of the key features of MIRCOM during the usual operations, since allows to see almost immediately the effects of radiations on biological samples, through the use of fluorescent markers.

Figure 3.6 shows two very important abilities of MIRCOM; in fact the image on the left is a 4x4 grid of protons on CR-39 (after chemical etching), shooting just one particle per time, and

the one on the right makes evident the very complex irradiation patterns that MIRCOM can follow.

To help in studying biological effects on the samples, a biology laboratory is built next to irradiation room (cf. **Figure 3.4**). Such laboratory is very useful to prepare and then post-process samples, allowing their easy and fast transfer to and from the microbeam.

There are two reasons why MIRCOM has been chosen for the proton irradiations useful for this work:

- The very high precision in terms of energy, incidence angle and number of protons shot. This eliminates most of side effects in the LET_{nc} assessment, allowing to focus just on the correctness of Politrack™ and simulation.
- The quite ease of access to this facility in the context of the internship at the basis of this work, because the study has been performed at IRSN, the same institution operating MIRCOM.

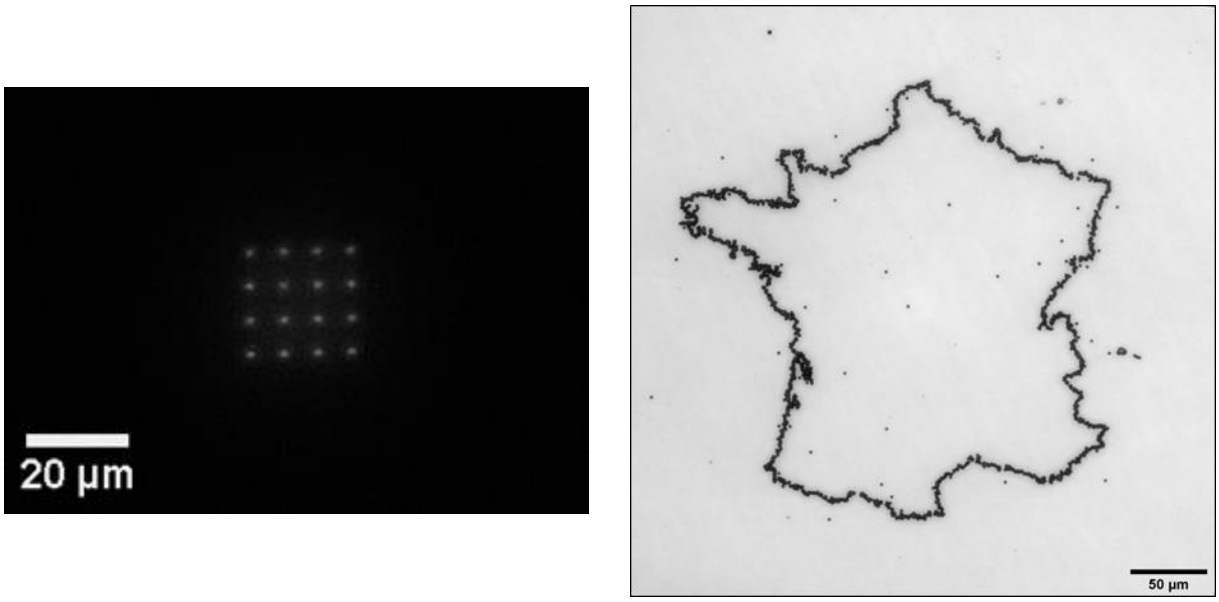

Figure 3.6 *– Examples of patterns produced by MIRCOM on track detectors. On the left a 4x4 grid using 4 MeV protons, on the right the shape of France using 6 MeV alpha particles. (Source https://www.irsn.fr/FR/Larecherche/outils-scientifiques/installations-moyens-experimentaux/microfaisceau-mircom/Pages/default.aspx)*

3.2.1.3 AMANDE facility

As for MIRCOM facility, even for AMANDE its main uses and the reasons it has been chosen for this work will initially be discussed, to focus then on the technical part.

The AMANDE facility is very useful in the characterisation of reference or standard detectors according to performance criteria defined by the International Organization for Standardization

(ISO). This facility is indeed used to study and characterise the response functions of the dosimeters to the very well-defined spectra of AMANDE. It is also a very good facility for the development of new dosimeters sensitive to neutrons and routines useful in the radiation protection, by implying it in the development, qualification, characterization and calibration phases (like in the case of this work) of these devices. In fact, it is very helpful when the dosimetric systems under study are used to determine the energy spectrum of a neutron field, as the spectra of AMANDE's fields are monoenergetic. This is exactly why the AMANDE facility has been chosen for the neutron irradiations useful for this thesis work.

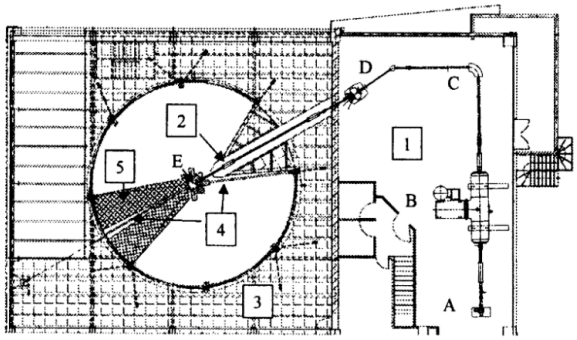

Accelerator:
A) Ion source
B) Tandetron
C) 90° Analysing Magnet
D) 35° bending and switching magnet
E) Neutron producing target

Building:
1) Accelerator room
2) Concrete platform supporting the beamline
3) Steel floor grating
4) Automated detector transport system
5) Removable access platform

Figure 3.7 *– AMANDE facility, before the construction of MIRCOM. On the right the accelerator room and on the left the irradiation one. (Source Gressier, V., Pelcot, G., Pochat, J. L., & Bolognese-Milstajn, T. (2003). New IRSN facilities for neutron production. Nuclear Instruments and Methods in Physics Research Section A: Accelerators, Spectrometers, Detectors and Associated Equipment, 505(1–2), 370–373. https://doi.org/10.1016/S0168-9002(03)01099-4)*

After the 90° magnet described in section 3.2.1.1, a second magnet of 35° (D in **Figure 3.7**) is present to compensate for timing differences created in the first one. At this point the beamline enters in the irradiation room (cf. **Figure 3.7**), where it is focused onto a thin foil made of scandium, lithium, deuterium, or tritium in titanium. The monoenergetic neutrons are indeed produced after the interaction of the charged incident particles (protons or deuterium) with the nuclei of the foil. The possible energies achievable are shown in **Table 3-3**. The energy of the neutrons produced depends on the material of the foil, its thickness, the emission angle and the energy of the incident particles (this is the reason why the ranges in the second to last column are so large).

***Table 3-3**: Nuclear reactions for achieving monoenergetic fields. Here energy of the incident particles means the one of protons and deuterons, while the reason for a big range in the energy of the neutrons is (Source modified from https://www.irsn.fr/EN/Research/Scientific-tools/experimental-facilities-means/Amande/Pages/Amande-facility.aspx)*

Incident particles	**Target**	**Reaction**	**Energy of incident particles [MeV]**	**Energy of neutrons on beam axis (0°)**	**Neutrons energy (ISO standard)**
Protons	Scandium	$^{45}Sc(p,n)^{45}Ti$	2,91 – 2,95	2 – 52 keV	24 keV
Protons	Lithium	$^{7}Li(p,n)^{7}Be$	1,9 – 2,5	120 – 650 keV	144 keV 250 keV 565 keV
Protons	Tritium	$^{3}H(p,n)^{3}He$	1,15 – 4	0,29 – 3,2 MeV	1,2 MeV 2,5 MeV 2,8 MeV
Deuterons	Deuterium	$^{2}H(d,n)^{3}He$	0,2 – 4	2,45 – 7,3 MeV	5 MeV
Deuterons	Tritium	$^{3}H(d,n)^{4}He$	0,1 – 4	14,7 – 20,8 MeV	14,8 MeV 19 MeV

It is possible to position the detectors to be irradiated at angles different from 0°, even up to ±150° to achieve peak energies different from the ones in the last column of the table; however it is preferred to put the targets on the beam axis, as the characteristics are the best in terms of energy resolution, intensity of the flux, and, among other things, the contribution of scattered neutrons.

As for as this last aspect, the contribution of neutrons scattered, a great effort has been put in order to minimize the background. The target, in fact, is located 7,2 meters above the ground,

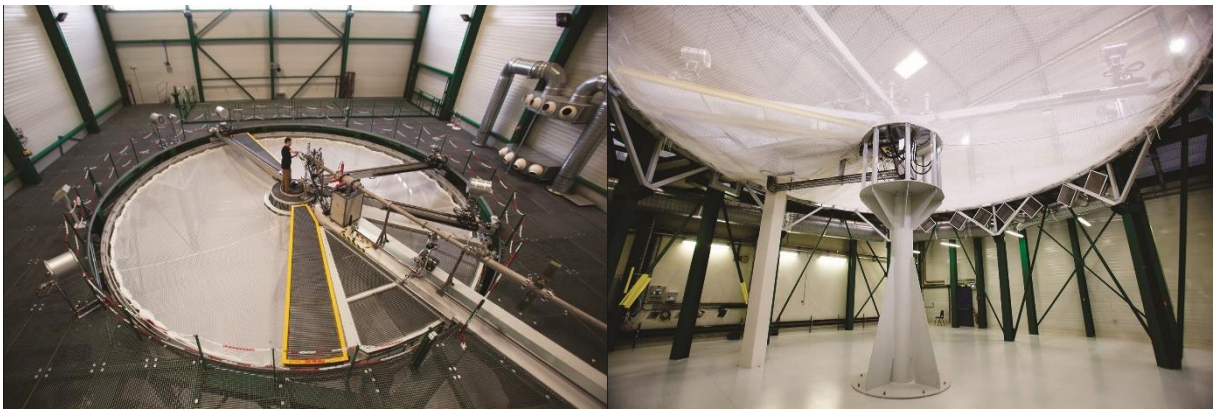

***Figure 3.8** – Views of AMANDE's experimental hall: on the left, the irradiation zone, above the ground (with the target at the center), on the right the the pillar supporting the experimental device (visible through the net) and the relative room, located below the ground. (Source: https://www.irsn.fr/FR/Larecherche/outils-scientifiques/installations-moyens-experimentaux/installation-amande/Pages/default.aspx)*

and around it a hole of 6 meters in radius, surrounded by meatal gratings. Furthermore, there are two moving metal gangways, to access the target, and three moving arms makes it possible to position the dosimeter at a distance between 50 cm and 6 meters, and an angular range of ±150°. Finally, the hall is surrounded by metal walls, instead of concrete, to again limit the backscattered neutrons and then the background. The resulting uncertainty on the energy of the neutron flux is less than 0,1%[24].

3.2.2 National Physical Laboratory (NPL)

NPL is the national measurement standards laboratory for the United Kingdom, founded in 1900 for "standardising and verifying instruments, for testing materials, and for the determination of physical constants". Over the years, the research activities in this laboratory included not only dosimetry and nuclear physics, but also all the other branches of physics, alongside with many engineering disciplines, like aeronautics, ship design and communications [25], [26].

In 1962 the facility shown in part in **Figure 3.9** has been installed for the production of monoenergetic neutron fields. The working principle of this system is very similar to the one of AMANDE, being a proton and deuteron accelerator shooting particles onto a target to achieve nuclear reactions, and in turns monoenergetic neutrons.

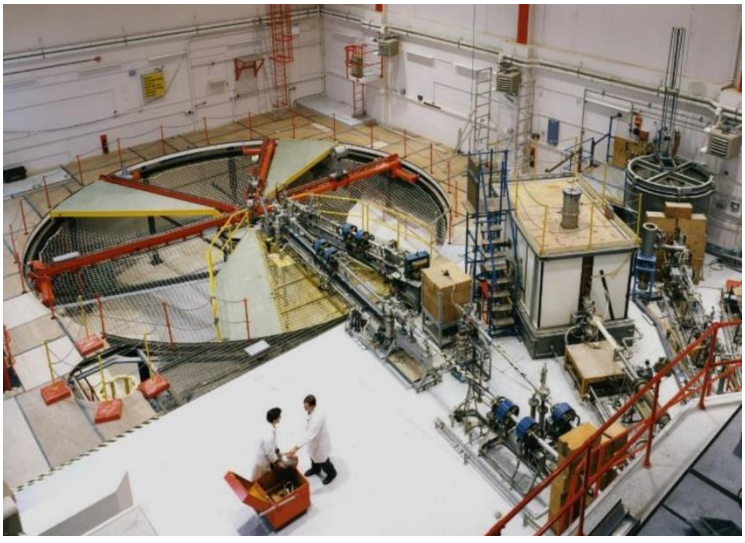

Figure 3.9 *– Irradiation hall at NPL facility, where it is possible to see the end of the beamline and the target zone. (Source: Castiñeira, S.-, Göök, A. B., Vidali, M., Hawkes, N. P., Roberts, N. J., Taylor, G. C., & Thomas. (2020.). Towards the adoption of 238-U(n,f) and 237-Np(n,f) as primary standards for fast neutron energies Welcome to the National Physical Laboratory.)*

The main difference between NPL's facility and AMANDE's one is the acceleration stage, where the Tandetron™ is replaced by a Van de Graaff accelerator, where voltages up to 3,5 MV are generated. This facility is, like AMANDE, capable of producing monoenergetic

neutron fields form the keV region to 20 MeV[27] according to the specification of the ISO standard for the neutron reference fields[28].

4 Computational model

In this chapter few introductory elements will be given to understand the simulation built, before presenting the actual working principles of the program. Once the structure of the code and the way it performs the LET_{sim} calculation have been explained, there will be presented ways to validate the physical model by comparing the simulation data to other reliable software.

4.1 Introduction to object-oriented programming and C++

The simulation used in this thesis work has been performed using a program developed in the programming language C++. A programming language is a series of words through which the user can give instructions to a computing machine; in simpler words it is the link between the user and the computer. In fact computer language is very different from any human language, so since the first days of computing different programming languages have been developed to translate the users' requests into instructions which can be understood by machines. Every programming language differs from each other for a great variety of elements, beginning with the whole programming paradigm, which is a sort of "philosophy" of the language. C++ is an *object-oriented programming* (*OOP*) language. Historically, a series of steps brought from the very first paradigm to OOP.

4.1.1 A brief history of programming

***Figure 4.1**: Scheme of non-structured programming.(Source: adapted from https://www.html.it/guide/guida-c2/)*

The simplest and historically earliest programming paradigm was the *non-structured programming*. In this case the program is composed by just one unique code block, called *main*, inside which all data are processed in sequence and are accessible by everything inside main, like exemplified in **Figure 4.1**.

This structure presents a lot of limitations if it is not used for very simple tasks. A first evolution was *procedural programming*, which introduced *procedures*, a series of computational steps to be carried out, defined in abstract, which can then be called in the execution of main (they can

also be called *functions*, *routines* and *subroutines*). This was a first step toward a major modularity of coding, simplifying the structure and enhancing the readability of programs.

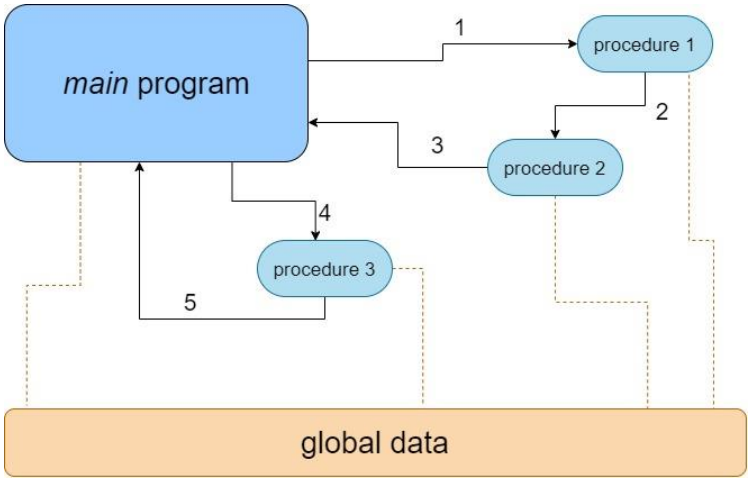

***Figure 4.2**: Scheme of procedural programming. (Source: adapted from https://www.html.it/guide/guida-c2/)*

In **Figure 4.2** it is shown how each part of the program uses the same input data. This means that each procedure must be written specifically in order to work with a given set of data with the disadvantage of a low flexibility.

This problem was partially overcome with the development of *modular programming* (cf. **Figure 4.3**) and the introduction of *modules*, independent parts of code each with its purpose and its internal set of data, that combined with data given by main can perform their specific operations. These modules are very flexible and can be used in different programs.

So now a single program is not composed by just one file, instead by as many as the number of modules used.

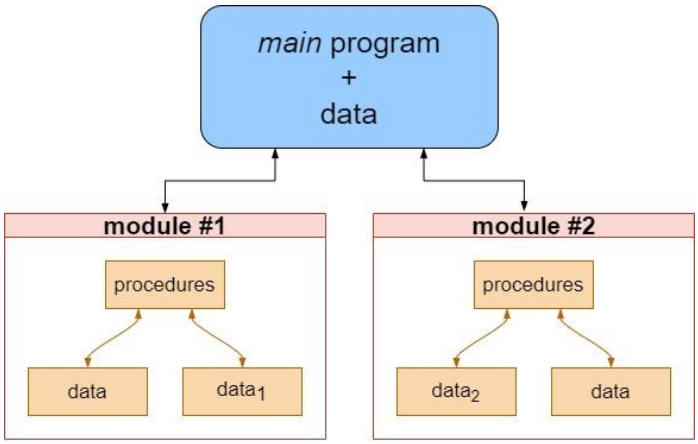

***Figure 4.3** – Scheme of modular programming. (Source: adapted from https://www.html.it/guide/guida-c2/)*

Over the years, this paradigm was widely used but showed more and more its limits as the complexity of the applications grew, and a major independence of the single modules was needed.

4.1.2 Object-oriented programming

The *object-oriented programming* was born from this necessity because it introduced more self-sufficient modules, which now are called objects; in OOP they are capable of interacting with one another and not just with main, unlike in modular programming. Each object is characterized by *methods* and *properties*, the first are the actions that it can perform, while the latter are the input data that are required to perform the actions. When coding using OOP the approach is no more top-down, starting from the main and building procedures to obtain the required program, instead the focus is on defining objects and connecting them, as summarised in **Figure 4.4**.

In OOP the objects having the same properties and methods are then gathered in *classes*. For example, if using an integer number, the number will be the object, while the class will be the whole integer type.

The philosophy behind the OOP is to build only once the classes and the methods in order to let them communicate with each other, and then to recall and use objects of the different classes. This way of coding is much clearer and simpler when dealing with complex and large projects and presents less redundant pieces of code enhancing the computing power and the readability. Another useful aspect is that a class, when properly built, can be used in different situations and

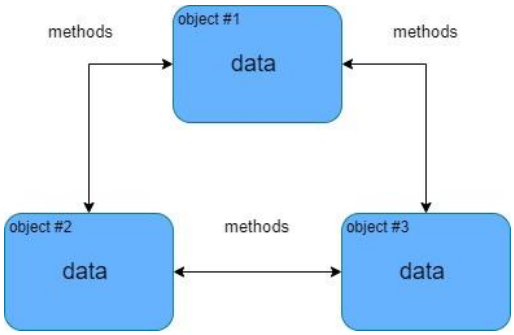

Figure 4.4 *– Scheme of object-oriented programming. (Source: adapted from https://www.html.it/guide/guida-c2/).*

by many people in different projects.[29]

4.1.2.1 C++

On this basis, in 1979 Bjarne Stroustrup started developing C++ which originally was called "C with classes", since it was born as an improvement of the procedural language C with the addition of the potentialities of the classes and the OOP in general. Since that moment, C++ kept evolving and gaining popularity to the point that it is nowadays one of the most used programming languages.

The heritage of procedural programming in C++ is testified by the coexistence of both a main() file and classes. The first one, like in the older programming paradigms, encloses the steps performed calling the members of the classes and defines the way they interact in the execution of the program.

It is easy to understand that the focus coding in C++ is on the classes, which can be seen as pieces of an engine, each one with its own structure and purpose and specifically built to interact with others in a well-defined way. Once the piece has been built, it is not important its internal composition provided that it can cooperate with others. This parallelism is useful to also explain another important step, that is a programmer does not need to build classes (or pieces) from scratch to build a program (or engine). In fact a lot of pre-built objects and classes exist, gathered in *toolkits*, which the programmer can use, modify and adapt for the specific purpose of his or her code, and this modularity and shareability are at the basis of the success of C++. In the development of the simulation used for this work, one of these toolkit named Geant4 has been used.

4.2 Geant4

Geant4 (which stands for *GEometry ANd Tracking*) "is a free software package composed of tools which can be used to accurately simulate the passage of particles through matter."[30]
The development of this toolkit started in 1994 as a joint effort between CERN and the High Energy Accelerator Research Organization, and has become over the years an international collaboration between physicists and software engineers from all over the world, who keep updating the code, including new features and providing support to other users.

The Geant4 tools are mainly pre-built classes for each aspect of an irradiation simulation, like geometry and materials, the physics of the interaction, the visualization of the events, the generation of data and so on. The programmer can select the aspects to control and modify the correspondent class.

The core of Geant4 is the large set of physical models for the interaction between particles, each optimized for a certain situation (specific particles involved, type of interaction, energy range and so on), in order to maximize computational power. The programmer must select a series specific physical models for the different types of interaction, and then collect them in a class called Physics List. Using these models, the simulation is performed using Monte Carlo

methods, meaning that the outcome of a physical interaction is not assessed using the real solution of physical equations but by means of random sampling by specific probability distributions. The Geant4 collaboration already created a series of pre-built physics list to use in wide range of situations.[31]

Then the user must set the experimental setup by defining:

- Geometry and materials of the target: in principle any geometry of whatever complexity can be coded, from a simple series of squares to very complex geometries (like CERN experiments). At this point one can also define a *detector region*, which is a region of the dosimeter where the program can collect specific data for the events.
- Primary generation of particles: the programmer must decide the features of the primary particles, such as energy, spatial and angular distributions, position and many more. By properly tuning all these parameters, one can simulate all kind of radiation sources.

Physics, geometry and primary particles are only the mandatory components of the simulation but are almost useless without adding other modules. Other very useful classes used in almost all simulations are the *visualization* and the *analysis* ones, which enable respectively the functions to display the simulation in a graphical way and to extract numerical data and histograms.

While a further explanation of the different classes in general is beyond the scope of this thesis, it can be useful to present the other three modules used in the simulation developed for this work. They are:

- RunAction: it concerns the whole process, so we enable the possibility to perform actions at the beginning and the end of the production of the single events. We can, for example, sum the whole energy deposited during the irradiation and calculate the dose (this could be a future development of the code);
- EventAction: the same as the previous but concerning a single primary particle produced. In this case, for example, we can sum the energy deposited by all the interactions, as it actually happens in the code and will be explained later;
- SteppingAction: enables the possibility to control what happens and extract data at the end of each step (for both primary and secondary particles).

In the following, the words *run*, *event* and *step* will be used to refer to these three different levels of action. In the next part the structure of the simulation developed for this work will be presented and a deeper understanding of all the concepts given previously can be possible.

4.3 Solid State Nuclear Track Detector (SSNTD) Simulation

The application has been coded with the clear goal to mimic the response of the Politrack to an irradiation with neutrons in the energy range between few hundreds of keV and 5 MeV. The aim of the simulation in fact is to analyse the energy and the range of the particles hitting the dosimeter and to try to give, for each of these particles, an LET_{sim} value as close to the LET_{nc} as possible. For this reason, the whole structure of the simulation relies on few preliminary hypotheses:

- In the energy range considered, the only secondary particle considered producing damage are protons, the reason has already been explained in Section 2.2;
- Events during which a primary neutron can produce two recoil protons leaving a track are neglected. This is a very rare situation due to the already low probability of a single interaction in the very small sensitive zone.

All the different modules previously introduced interact one with each other in a complex way to have a work flow which can be summarized as in **Figure 4.5**, and will be explained in the following.

4.3.1 Structure of a simulation

A simulation is divided into three nested levels, *run*, *event* and *step level* in a hierarchical order, meaning that a level can access to the information produced in the enclosed ones and also modify them, while it is not possible the contrary; this is a way of keeping safe the general behaviour when something unexpected happens in the simulation of a single event or step.

The simulation starts with preliminary operations useful to perform the calculations and specific of the C++ environment, then the physics list, the source and the geometry are acknowledged and set and the analysis instruments are initialized, with the creation of a file to store the final data.

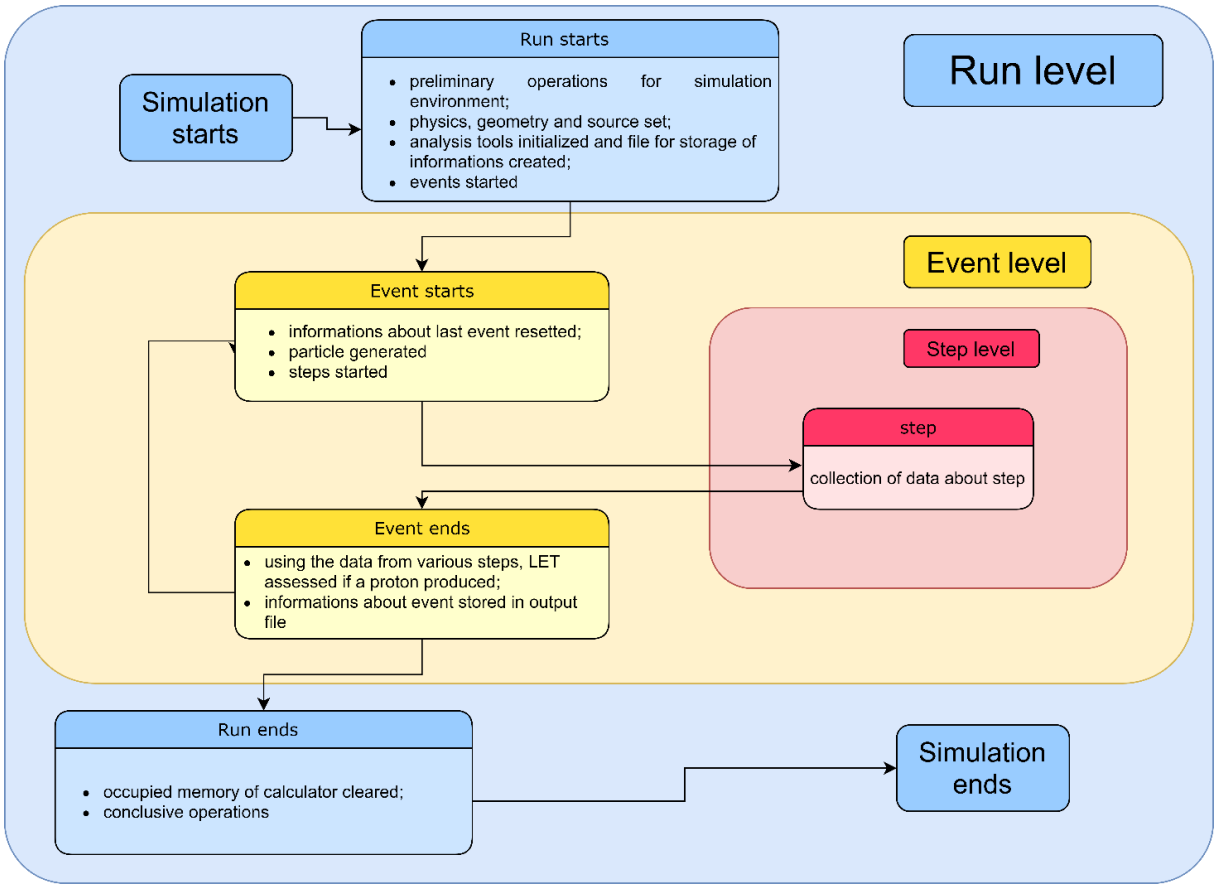

Figure 4.5 *– Conceptual flux of the SSNTD simulation in Geant4.*

For the SSNTD simulation the preliminary conditions are:

- Physics list: the used is the one called *QBBC*, a pre-built and largely tested physics list with an important modification, that is a method to fix a maximum limit to the length of the steps to 0.1 µm. In the following discussion an explanation will be presented on why such a modification was implemented.
- Source: the simulation has been built to include both monoenergetic protons and neutrons, at whatever energy, and broad neutron spectra of bare AmBe and bare ^{252}Cf sources. The incidence is always orthogonal to the surface and the geometry is planar. This means that the particles are produced homogenously in random positions of an area of the same dimensions of the dosimeter parallel to it.
- Geometry: it can be visualized in **Figure 4.6** and it depends on the type of irradiation.
    - Proton: it is composed by two regions, one for the dosimeter, made of CR-39 with dimensions 2,5 cm x 2,5 cm x 1,5 mm, and one for the window made of Si_3N_4 of the same area but 150 nm of thickness, to simulate the irradiation at MIRCOM. The gap is 250 µm and is filled with air, like all the surroundings of the geometries.

- Neutron: is composed by three regions, one for the PMMA radiator (cf. the close up of **Figure 4.10** at page 75) having the same area and 10 mm of thickness, one again for the dosimeter (the same as for proton irradiation) and one for the ICRU soft tissue phantom with dimensions 15 cm x 30 cm x 30 cm.

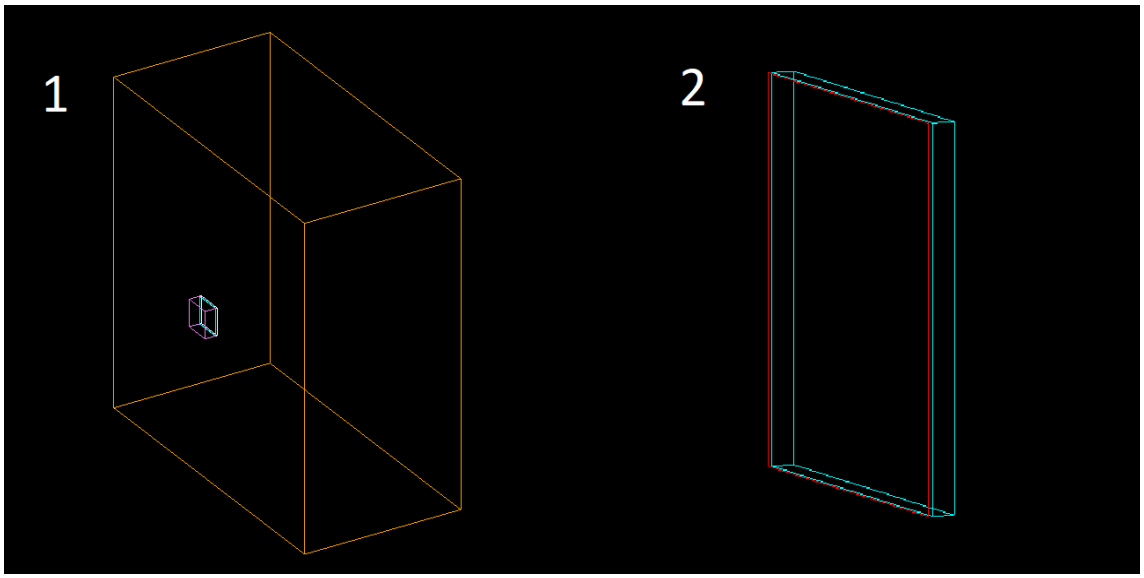

Figure 4.6 *– Geometry of the simulation. On the left in the case of neutron irradiation and on the right for proton irradiation. In blue the dosimeter, red the window, violet the converter, and orange the phantom.*

At this point, sequentially, a series of events (the number is chosen by the user) is started, each one independent from the others, which represent the life of a single primary particle.

The simulation of an event is performed as a series of point interactions between the particle and the atoms of the material. The path of the particle is thus divided into steps, each one normally being the part of the event between two interactions promoting the production of a secondary particle: production of electrons if the particle is a proton and of a proton if the primary particles are neutrons. As for as neutrons, this is not in contrast with the hypothesis at page 68 because the neglected neutrons are those producing two protons in the range between the surface of CR-39 and the removed layer.

In this context the word “production” is meant in a computational way that is to say that a secondary particle will be simulated and have a history on its own. The threshold of production (called *cut*) can be set and is a very crucial point of a simulation since it highly influences the computational time: if the threshold is too low, particles at very low energies will be produced which means that the steps will be very short and the simulation will take more time without any real advantage. On the contrary, if the threshold is too high, only high energy secondaries will be simulated and LET_{sim} assessment could not be possible.

It is crucial to understand that from a physical point of view, the occurrence of interactions which should produce particles under the cut is not prohibited; on the contrary this kind of interactions constantly occur but the secondaries produced are not simulated. In this case, for energy conservation, the kinetic energy lost by the primary particle in the production of a secondary which is not simulated is accounted as energy deposited during the step, and it sums up to the energy lost by the particle in excitation of the target material. To sum up, at the end of the step, from a computational point of view, two different figures will account for the energy lost by a particle (mainly protons): the deposited energy during the step (which in turns is the sum of ionization processes and production of electrons under the cut) and the kinetic energy of the secondaries (electrons above the cut). To know the total energy deposited during a step, then it is necessary to add the energy deposited during the step and the initial kinetic energy of the secondaries ionized.

It is possible to understand now that the length of the step can be highly affected by the probability of interaction between a proton and an electron, and so varies with the energy of the primary particle along its path. To prevent this variability, a method to fix the maximum length of the step has been added to the Physics List, in order to put a high cut energy (no secondary electrons will be produced, fastening the simulation) but in the meantime to have an optimal segmentation of the track of the proton for the LET_{sim} assessment.

The process to calculate the LET_{sim} indeed starts at the step level where data about it is stored in unidimensional matrixes, called *vectors*, for protons, provided that they can reach the volume between the surface of the dosimeter and the removed layer. The most important data stored for each step of the proton are:

- position at the beginning and end of the step;
- length of the step;
- kinetic energy at the beginning and end of the step;
- deposited energy;
- incidence angle.

These vectors are then processed at the event level where therefore the program has access to all the information belonging to each relevant step.

For the purpose of this work, two different ways for the calculation of LET_{sim} on this basis have been developed. A first version, based on an integration of the energy from the initial to the

final points of the particle inside CR-39 and a second one, described later better suited to predict the morphology of the track after the chemical etching. Since the aim is to simulate as accurately as possible the Politrack^{TM}'s results, the second version has been introduced because, as the work proceeded, it has been clearer and clearer that the first approach could not include a series of events (mainly overetched tracks) in an accurate way.

These two procedures will be described in the next two sections, starting from the first one. It is important to illustrate both of them to show the evolution of the simulation and the studies performed.

4.3.2 LET_{sim} assessment through integration

This procedure will be described starting from the protons, and then generalising to neutrons, since the theoretical basis is the same, but the procedure is slightly more complex in the second case because of the kinematic of the elastic scattering. This difference makes the LET_{sim} assessment, and so the code, more complex when the primary particles are neutrons, because not all recoil protons are capable of producing tracks.

4.3.2.1 Protons

The simulation has been built to reproduce an irradiation at MIRCOM, as it can be seen in **Figure 4.7**, where each yellow dot is a proton. To understand the LET_{sim} assessment procedure, it is important to remember that protons are all shot at the same position along the x-axis, which is behind the Si_3N_4 window, and all perpendicular to the surface as in **Figure 4.8**.

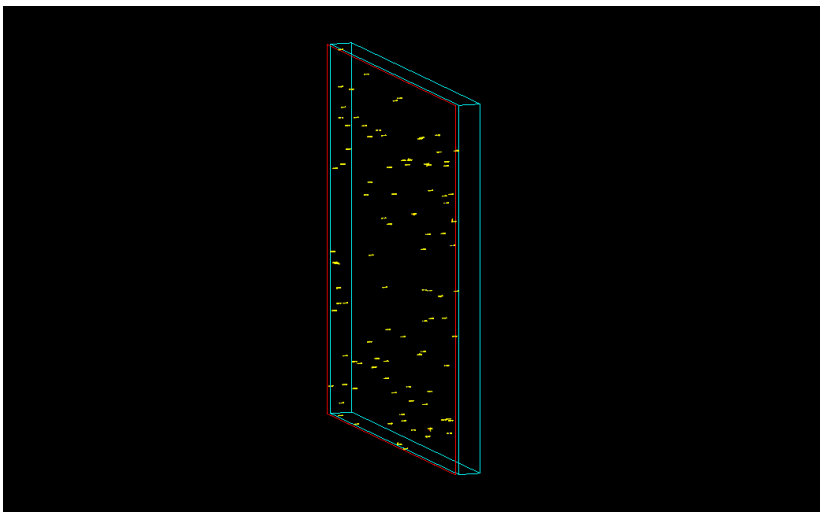

Figure 4.7 *– Simulation of a proton irradiation.*

Due to the geometry, the behaviour of the protons is very predictable, and it has been possible to focus just on the routine for LET_{sim} calculation.

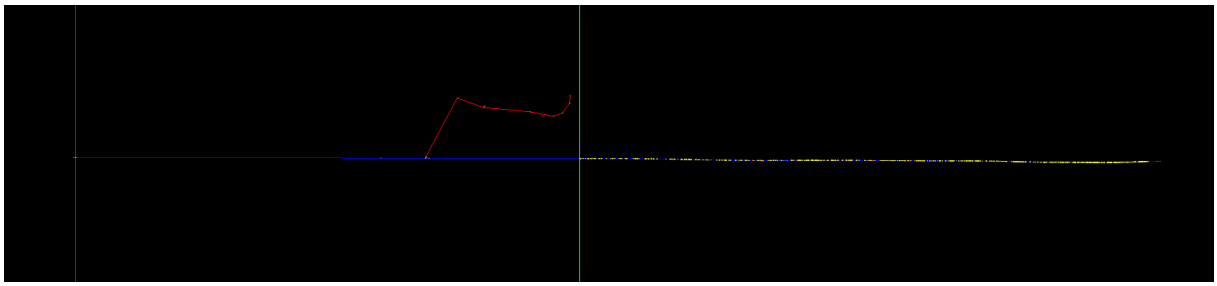

Figure 4.8 *– Visualization of the path of a single proton. The blue line is the trajectory of the proton, while the red one is a secondary electron. Yellow dots are the steps. The two vertical lines are the surfaces of the window (red) and CR-39 (cyan) with the air gap in between.*

The first action the code performs using data from the steps, is to calculate the theoretical end of the track, which is necessary to collect the deposited energy from the initial point, at the entrance of CR-39, to the pit of the etched track.

To know the length of the track l we need to multiply the track etch rate V_t for the etching time t, so it is possible to write:

$$l = V_t \cdot t = \frac{V_t}{V_b} \cdot V_b t = V \cdot h \tag{4-1}$$

Where we introduced the bulk etch rate V_b, the mean etch rate ratio $V=V_{mean}=V_t/V_b$, and the etched depth h.

While h depends on the particular etching process, supplier and even production batch, and is a known quantity set at the beginning of the simulation, V has to be calculated. This is done inverting the relation from Caresana et al.[13], for $LET_{nc}=f(V_{mean})$, which is the equation that Politrack uses, to obtain $V_{mean}=f(LET_{nc})$ as follows:

$$\begin{aligned} V_{mean} = {} & -2{,}339 \cdot 10^{-12} LET^6 + 1{,}162 \cdot 10^{-9} LET^5 - 2{,}222 \cdot 10^{-7} LET^4 \\ & + 2{,}083 \cdot 10^{-5} LET^3 - 9{,}926 \cdot 10^{-4} LET^2 + 3{,}212 \\ & \cdot 10^{-2} LET + 8{,}999 \cdot 10^{-1} \end{aligned} \tag{4-2}$$

It is possible to notice that to calculate V_{mean} it is necessary to know the LET_{nc}, and this can seem a recursive problem. The proposed solution is to use SRIM code[32] to calculate the average LET ($\overline{LET}$) as a function of the kinetic energy of the proton at the surface of CR-39 (or the starting one in case of self-radiation, cf. **Figure 4.11**), which is known because it is a quantity provided by Geant4. Thus this whole routine, summarized in **Figure 4.9**, is executed

by the program (in the reverse order), which takes the energy of the step at the surface, using SRIM calculates $\overline{LET}$, then V_{mean} to finally know the theoretical depth of the track.

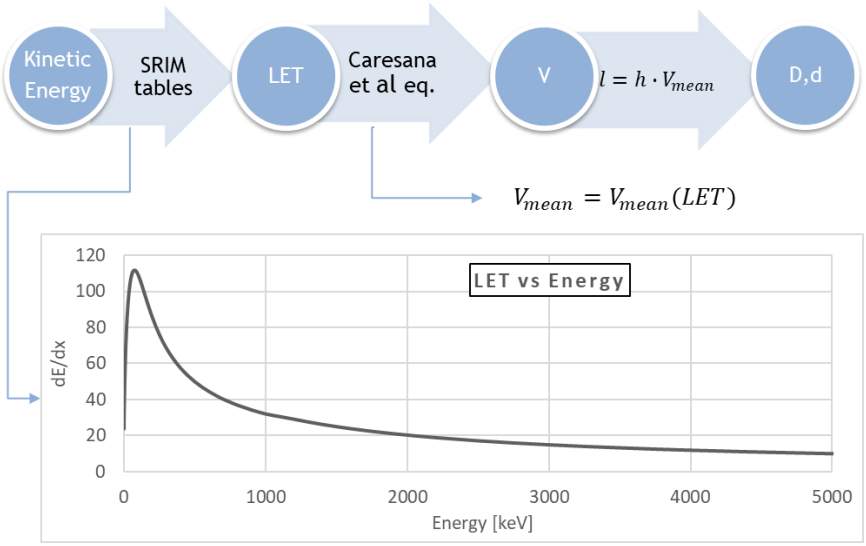

Figure 4.9 *– Schematization of the routine to calculate the theoretical etched depth.*

Once the theoretical length of the track is known, the program simply sums the energy deposited and the length of the steps, for all the steps between the entrance inside CR-39 and the end of the track, to obtain the deposited energy E_{dep} and the total length of the track x Finally the LET_{sim} is:

$$LET_{sim} = \frac{E_{dep}}{x}$$

This whole process is performed for each proton inside CR-39 and is at the basis for the more complex case of neutron irradiation.

4.3.2.2 Neutrons

Neutrons leave tracks thanks to recoil protons, as already stated more than once, and this is why the core of the LET_{sim} assessment is the same in the two cases. In this second case (cf. **Figure 4.10** for a visual representation), however, it has been necessary to implement methods to consider a more complex geometry (due to the addition of radiator and phantom) and set of cases, because now protons can be produced at any point, with any energy from zero to the energy of primary neutrons, and any incidence angle. In **Figure 4.11** one can see the possible proton paths that can lead to a track during the simulation.

To accurately reproduce the irradiation setup, an event starts with a neutron shot perpendicularly to the surface of the radiator, if it interacts with the material it produces a proton

and the following procedure takes place, otherwise the event is killed, meaning that no further analysis is performed and no information about it is displayed at the end of the simulation.

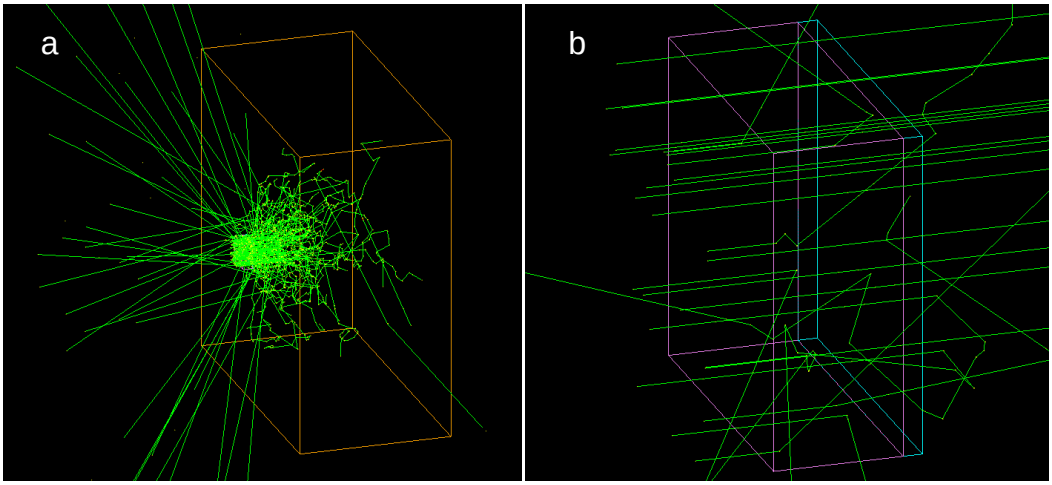

Figure 4.10 *– Visualization of a neutron irradiation; a) is the whole geometry, b) a close up of converter and detector.*

Once the proton has been produced, the first passage for the code is to check if the position is inside the so-called *sensitive region*. This is a volume defined in order to be large enough to include all the possible protons capable of reaching the volume between CR-39 surface and *h*, and this leaving a track. Since at 5 MeV the protons have a residual range of 281 μm, and to also include the proton with the highest energy with a very high degree of confidence, the sensitive region is centred in *h* and has a thickness of 800 μm. This phase is useful to reduce the calculation time, because if the proton is outside the sensitive region the event is killed. If

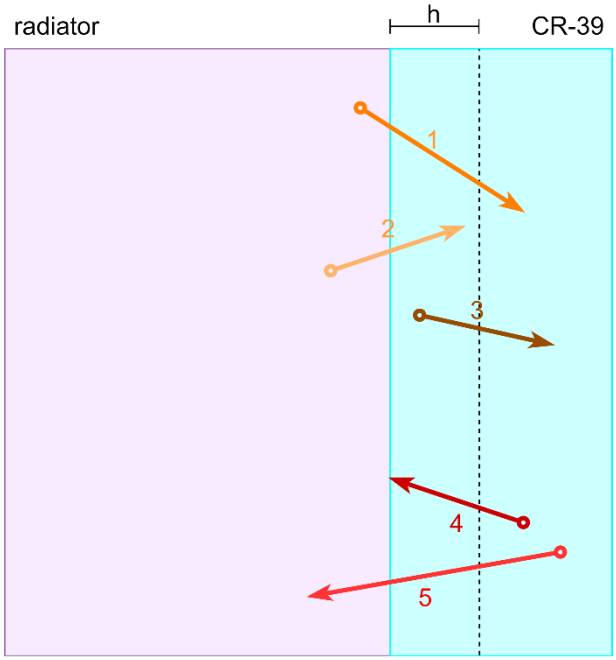

Figure 4.11 *– Schematization of the possible proton paths leading to a track in the simulation. (1), (2), and (3) are moving forward. while (4) and (5) backward. (1) are underetched tracks, (2) overetched tracks, (3) self-radiation.*

the control is positive, the software checks which of the cases represented in **Figure 4.11** the proton follows. On this basis, it fixes two points and between them it integrates over all the steps the energy deposit and the length travelled.

1. Underetched tracks which are the easiest particles to calculate because their etching dynamics is more predictable:
    a. initial point: surface between CR-39 and radiator;
    b. final point: theoretical depth of the track.
2. Overetched tracks (cf. section 2.2.2) are way more complex than the previous case. For them, the two points are:
    a. initial point: surface between CR-39 radiator or initial position, if they are coming from auto-radiation;
    b. final position: point where the particle stops.

    This is an approximation, because in the reality the track development of overetched tracks is far more complex, as already introduced in section 2.2.2.
3. Tracks from self-radiation can actually be both under- and overetched, depending on if they stop either before or after they reach h. The underetched ones become more and more important as the energy decreases, because at very low energies the range of protons is too low for them to reach *h* when produced in the radiator:
    a. initial point: initial position between surface and *h;*
    b. final position: theoretical depth of the track (as illustrated) or even the point where the particle stops before *h*.
4. Tracks moving backward are rare in this geometry and almost negligible, because they can mainly be produced by neutrons backscattered by the phantom but are of high importance when the dosimeters are used in real working conditions. For this reason, a piece of code considering also these events has been added for future developments. The two points in this case are:
    a. initial point: where the particle stops;
    b. final point: theoretical end of the track.
5. These tracks are the same as (4) with the difference that travel for the whole volume between the surface and *h*, then the only difference is the initial position, which is indeed the surface.

At this point the code applies three filters to the event, meaning that there are three conditions to be fulfilled to consider the event valid:

a) Proton direction needs to respect the already mentioned condition on the dip angle θ

$$sin\ \theta > \frac{1}{V}$$

b) At the time they are produced, proton must be moving toward *h* and not away from it (this does not exclude backscattered neutrons, which indeed move toward *h*);

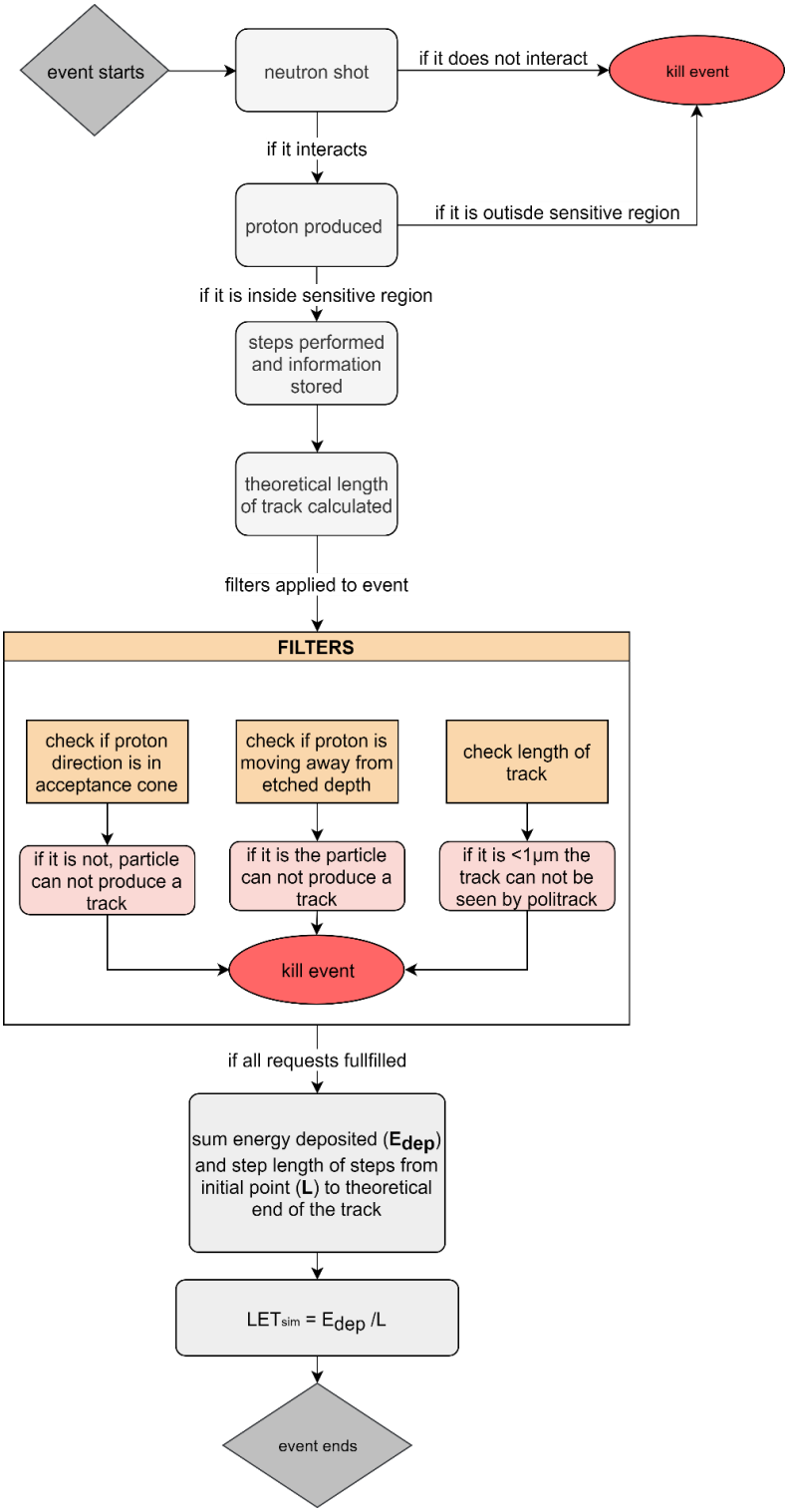

Figure 4.12 *– Flux scheme of the simulation performed of an event using the first version of the code.*

c) The length of the track *l* must be $l \geq 1\mu m$ in order to be detected by the optical system.

If one or more of these are not fulfilled, the event is killed; on the other hand, if it passes all the previous "tests", it is a valid track and the simulation calculates the LET_{sim} the same way it is calculated when the primary particles are protons. All this process is summarized in **Figure 4.12**.

Once the calculation of the LET_{sim} for each single event has been performed, the program stores a series of data in a file to work on at the end of the run.

Between the many available data, the program shows:

- initial position;
- final position;
- initial energy;
- energy deposited E_{dep};
- dip angle;
- LET_{sim}.

The final output of the simulation is a file containing all the tracks and these data for each. Note that all these quantities refer to the recoil proton.

It is important to point out that, due to the high flexibility of the code, the user can decide to change the output quantities at any time and depending on what he or she is interested in, without interfering with the physical model, because the two parts of the code are completely independent thanks to the object-oriented philosophy of the code.

4.3.2.3 Limits

During the development and optimization of this routine, it became clearer and clearer that the procedure for the LET_{sim} assessment fails to model the protons which do not reach the etched depth *h*. These particles indeed leave tracks which have a morphology dependent not only on the specific energy, but also on the successive etching process, which tends to give a final spherical shape to the section of the track, as explained in Section 2.2.2. For this reason, the code has been modified and a it has been written according to a new philosophy which is described in the next section.

4.3.3 LET assessment through track morphology

The first version of the code had the problem to be too far from the real evolution of the track morphology. To solve this problem, the LET_{sim} assessment has been changed profoundly without however modifying all the remaining code, that is to say until the storage of information about the steps.

Now the simulation, after having produced and followed the recoil protons from the production moment to its complete stopping, understands if they have travelled in a volume where a track can be produced and then calculates what would be the morphology of an hypothetical track induced by its passage. At the end of this step, the code generates an estimation of major and minor axes *D* and *d* of the hypothetical hole. This procedure is based on the model by Somogyi and Szalay [33] of the track diameter kinetics in solid state nuclear track detectors under the assumption of constant V_t, which is presented in the following in order to understand the code.

After this stage, the simulation calculates the LET_{sim} with the same equations used by the Politrack™ using the simulated *D* and *d* to give an estimation of what would be the *LETnc* distribution produced by the device.

4.3.3.1 Morphology model

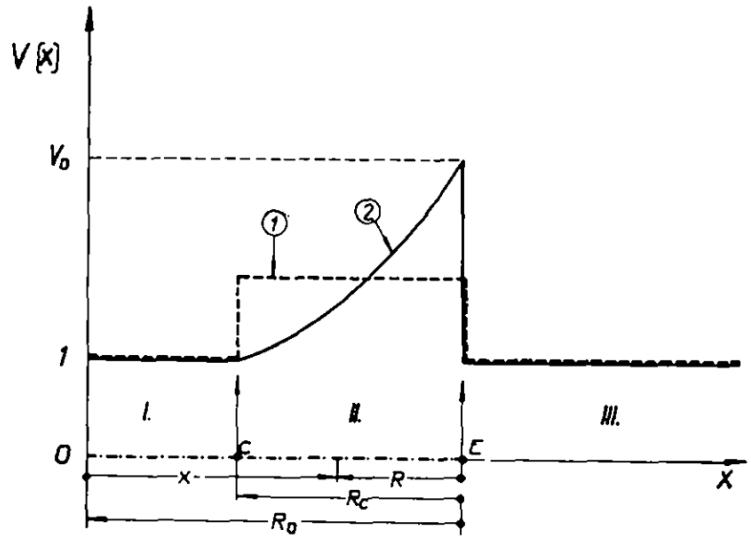

Figure 4.13 *– Variation of the etch rate ratio V along the etching direction x. Solid line (curve 1) represents the realistic case for variable V_t, while the dashed line (curve 2) stands for the approximation of constant V_t.(Source Somogyi, G., & Szalay, S. A. (1973). Track-diameter kinetics in dielectric track detectors. Nuclear Instruments and Methods, 109(2), 211–232. https://doi.org/10.1016/0029-554X(73)90265-6)*

To describe the kinetics of track formation, it is useful to introduce the most characteristic track parameters. With reference to **Figure 4.13**, let use suppose that a neutron interacts in the point C and produces a proton which then travels up to E, where it stops having released all the

energy. We can then define three regions, two (I and III) where the etching ratio is equal to one, meaning that no damage has been produced, and one (II) corresponding to the path of the particle, where the ratio increases as the linear energy transfer increases, due to the higher density of defects. These regions are described introducing a *critical residual range* R_c, along which $V > 1$, and the *etchable range* R_0.

Somogyi and Szalay started by assuming that the known quantities for a particle are the mean value for the etch rate ratio V_{mean}, the incidence angle θ, and R_0 to finally obtain the major and minor axes of the hole (D and d). They identified three phases of track etching for D and two for d, denoted respectively by D_1, D_2, D_3 and d_1, d_2, each one defined by an equation (which will be presented later). Then, depending on the depth of the removed layer compared to certain validity ranges(H_1, H_2, h_1), it is possible to determine in which phase of the etching development the track is, and in turns which will be the value of D and d. In **Figure 4.14** it is possible to see the various phases.

In the phase when D is equal to D_1 the curve constituting the opening of the pit is an ellipse, while it is a circle for D_3 and a transition between the two for D_2.

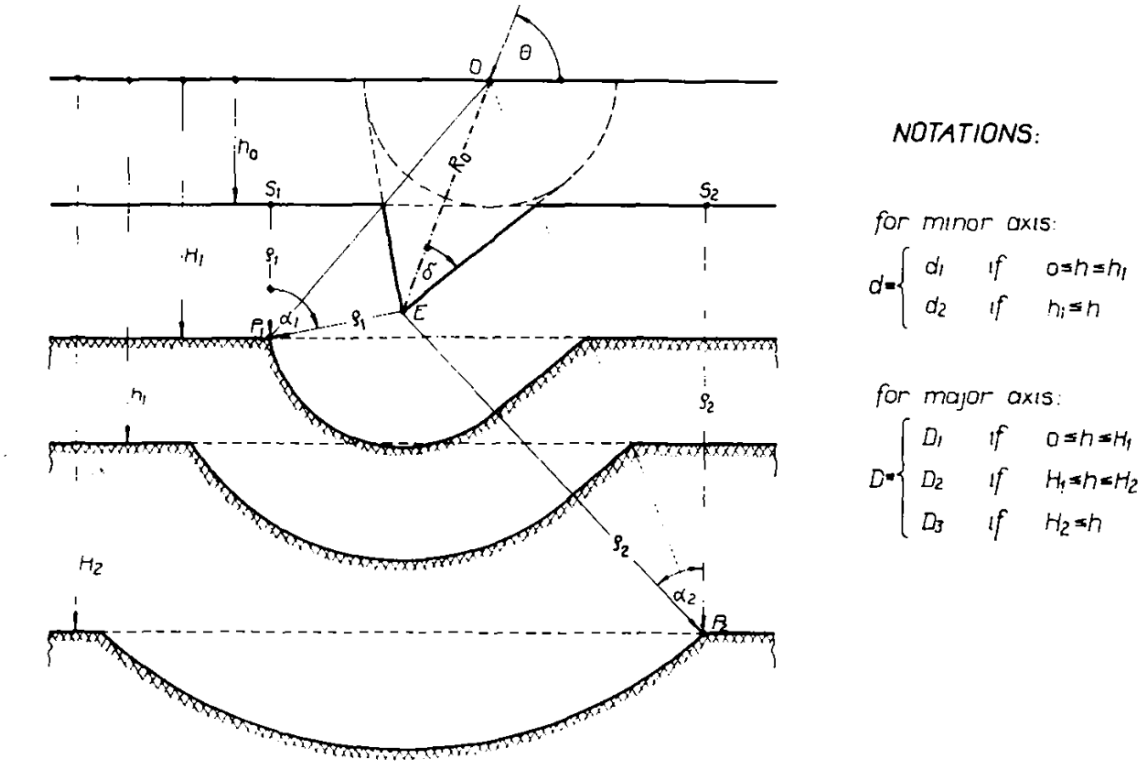

Figure 4.14 *– Typical phases of etch-pit evolution in an isotropic solid for a particle of entrance angle θ. (Source: Somogyi, G., & Szalay, S. A. (1973). Track-diameter kinetics in dielectric track detectors. Nuclear Instruments and Methods, 109(2), 211–232.*

On the other hand, in the first etching phase, the minor axis is represented by the minor axis of the ellipse; in the second, it is equal to the diameter for the circle.

The mathematical demonstration of the equations used in the model goes beyond the aim of this work but more details can be found in the work "Track-diameter kinetics in dielectric track detectors" by Somogyi G., & Szalay S. A. (1973). Anyway, it may be useful to present them in the following table.

***Table 4-1**:: Formulas for calculating the minor and major axes of etch-pits in an isotropic solid at constant V.*

Notation	Formula	Validity range
Minor axis (d)	$d_1 = 2h\sqrt{\frac{V\sin\theta - 1}{V\sin\theta + 1}}$	$0 < h < h_1$
	$d_2 = D_3$	$h_1 < h$
Major axis (D)	$D_1 = 2h\frac{\sqrt{V^2 - 1}}{V\sin\theta + 1}$	$0 < h < H_1$
	$D_2 = \frac{1}{2}(D_1 + D_3) + \left(R_0 - \frac{hV}{V\sin\theta + 1}\right)\cos\theta$	$H_1 < h < H_2$
	$D_3 = 2\sqrt{\left\{R_0\left(\sin\theta - \frac{1}{V}\right)\left[2h - R_0\left(\sin\theta + \frac{1}{V}\right)\right]\right\}}$	$H_2 < h$

Where:

$$h_1 = \left(\frac{R_0}{V}\right) + R_0\sin\theta$$

$$H_1 = \left(\frac{R_0}{V}\right) + R_0\frac{\mathrm{V}\sin\theta - 1}{\mathrm{V} - \sin\theta + \cos\theta\sqrt{V^2 - 1}}$$

$$H_2 = \left(\frac{R_0}{V}\right) + R_0\frac{\mathrm{V}\sin\theta - 1}{\mathrm{V} - \sin\theta - \cos\theta\sqrt{V^2 - 1}}$$

It is possible to see that, once the incidence angle, the etchable range, and the mean etching rate ratio are known, using this model one can calculate the major and minor axes whether a track is either over- or under-etched. This enhances the possibility to have a match between LET_{sim} and LET_{nc} with respect to the previous version of the code.

To do so, the software follows a procedure very similar to the previous one (cf. **Figure 4.9**), different only in two steps:

- instead of using the SRIM tables to calculate the LET, the code now divides the initial energy (the one at the interface or the initial one if the proton is produced in between the surface and h) by the total range;
- instead of calculating the theoretical etched depth, the code calculates the theoretical major and minor axes of the hole like in **Figure 4.15** using the equations of **Table 4-1**.

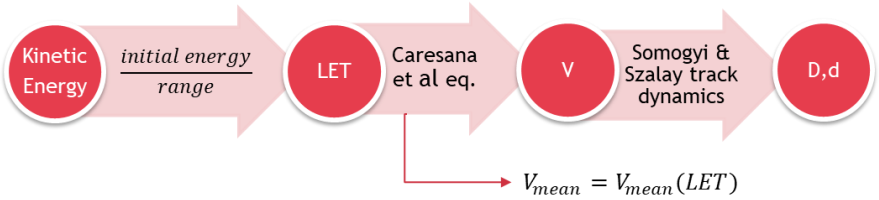

Figure 4.15 *– Schematization of the routine to calculate theoretical major and minor axes*

The theoretical D and d calculated in this way, are in principle the computational equivalent of the quantities that Politrack™ measures. Thus it is possible to use the same equations that its analysis system uses to calculate the LET_{nc} (cf. Section 2.2.3) to calculate the theoretical LET_{sim}. What explained above is the routine followed for each particle by the simulation code and it is summarized in **Figure 4.16**. In the figure, the denomination "*dosimeter region*" is used to refer to the volume included between the surface of CR-39 and the etched depth.

Like in the previous version of the code, once the program calculates the final LET_{sim} value, it stores a series of information and goes to the following event.

Thanks to an improvement of the code, it stores more data about the protons, namely:

- initial and final position;
- energy at the production moment and when it crosses the boundary of the dosimeter region;
- V;
- dip angle;
- D and d;
- LET_{sim}.

At the end of the simulation, these quantities are contained in a file ready to be used for the following data analysis.

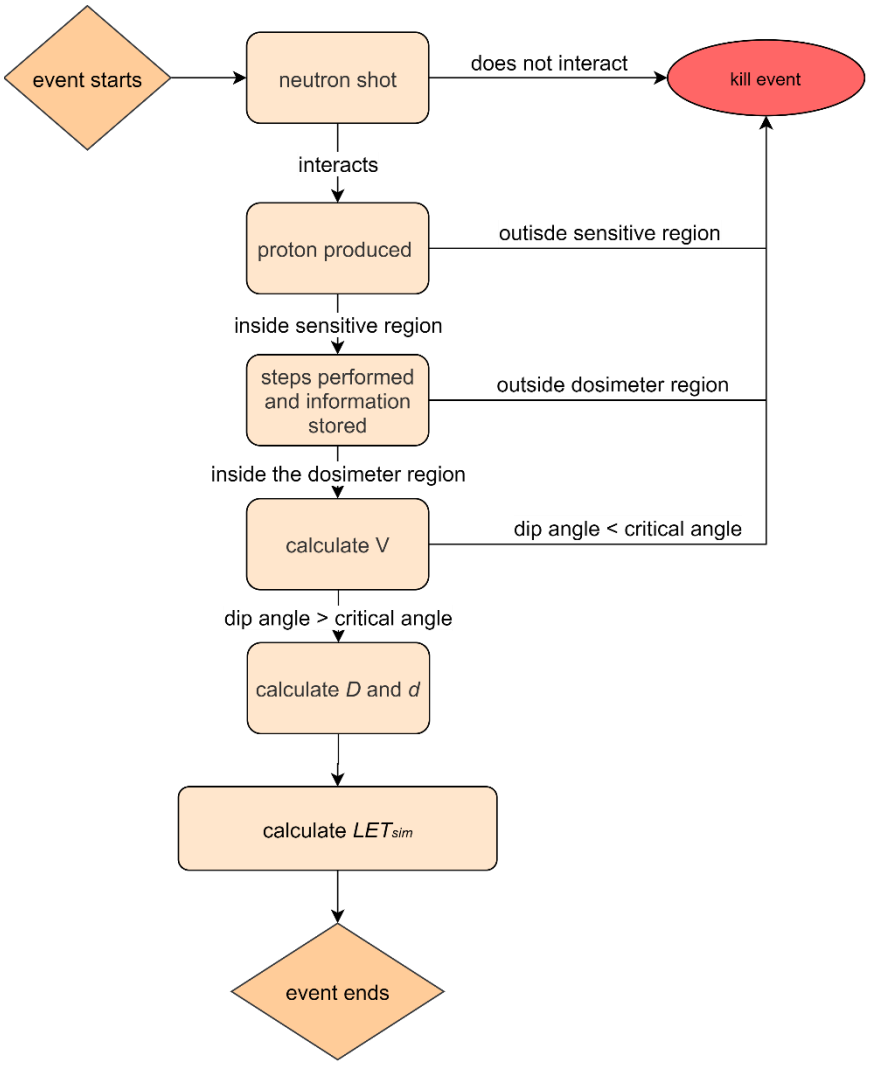

Figure 4.16 *– Flux scheme of the simulation performed of an event using the first version of the code.*

There are few advantages that make this version of the code preferable with respect to the previous:

a) It is based on an already studied physical model, more solid than the previous LET assessment routine.
b) This procedure includes the overetched tracks and self-radiation, not just the under-etched tracks and enhances the possibility to have a match between LET_{sim} and LET_{nc} with respect to the previous version of the code.
c) The code is written in such a way that in future improvements, the model can easily be substituted in favour of a more accurate one.

For all these reasons, the final results have been simulated using this version.

4.3.4 Validation of the physical model

Before using a new application built with G4, it is good practice to compare the results of the simulation to experimental data or to other well characterized and tested simulations, in order to have either proofs of the validity of the program developed. In fact, being new applications, they have never been tested and their reliability has to be demonstrated.

Obviously, a lot of physical process could be tested, but for the purpose of this work, the choice has been to test the two main process leading to a track:

- the release of energy of the protons traveling inside CR-39;
- the production of the recoil protons due to a neutron irradiation.

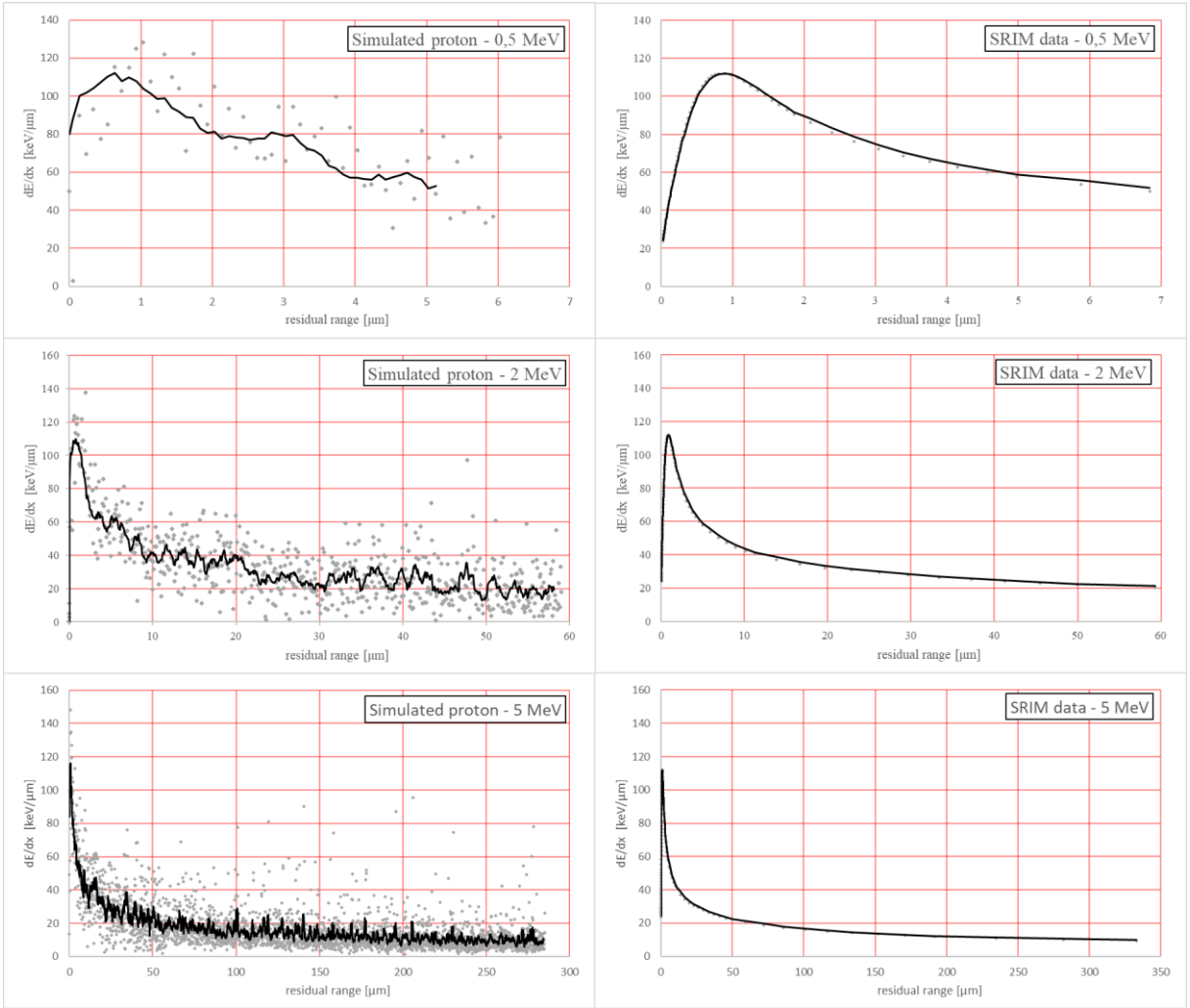

Figure 4.17 *– Comparison between data from the simulation (left) and the SRIM code (right) for three reference energies.*

In the first case, the physical model has been tested by comparing the linear energy transfer *dE/dx* as a function of the residual range of the single steps to the theoretical tendency computed

using the SRIM code. **Figure 4.17** shows on the left the simulation data, where grey dots are the single steps value, and the black line is the 10-steps moving average.

For the latter, the validation consists in comparing (**Figure 4.18**) the energy and angle distributions to the theoretical ones[34], and by showing the variation of the recoil angle θ in the centre of mass reference system, with respect to the energy of the recoil proton Ep , calculated starting from the equation[34]:

$$E_p = E_n \frac{1 - cos\theta}{2}$$

where E_n is the energy of the neutron.

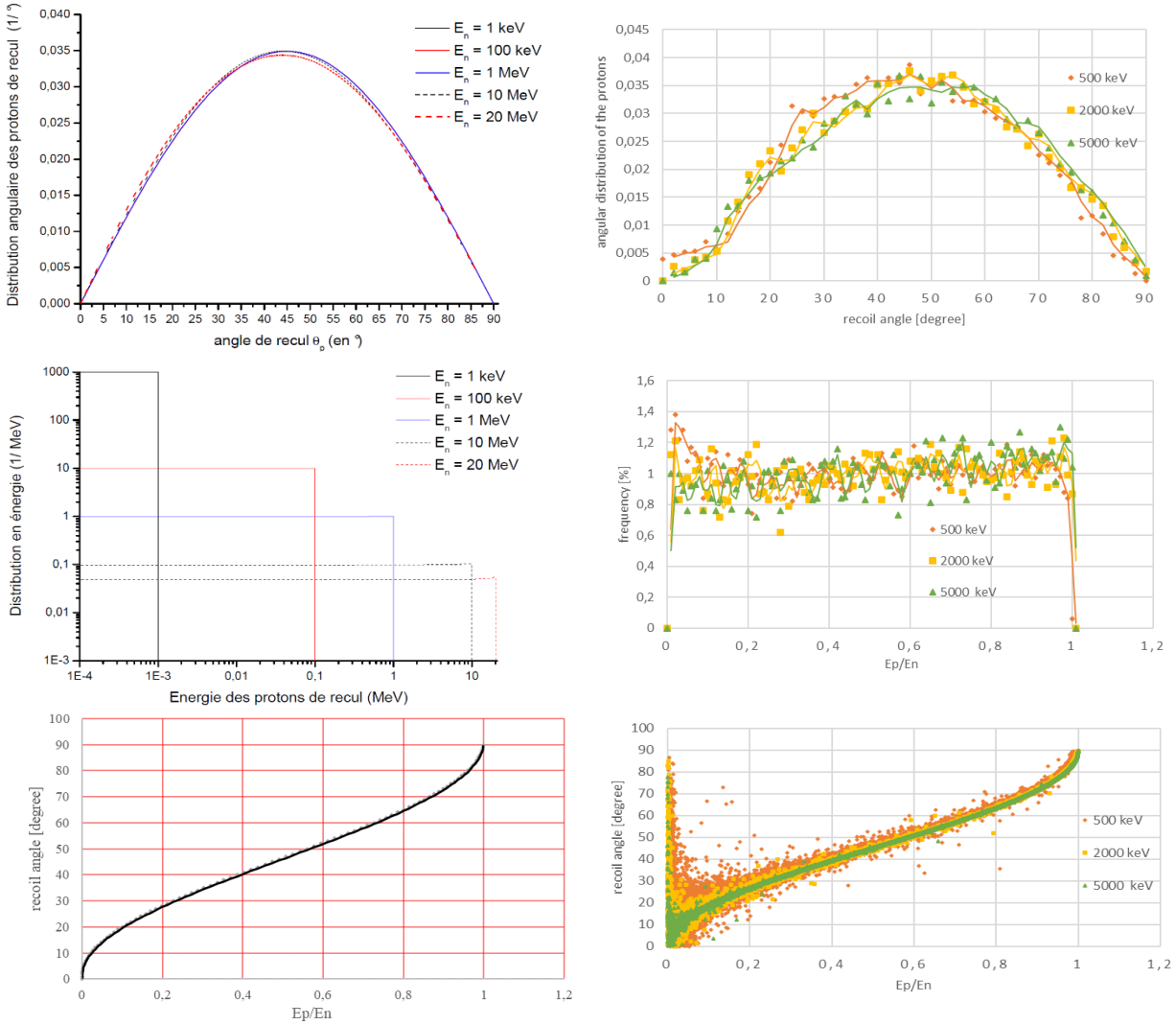

Figure 4.18 *– Graphs showing the correspondence between theoretical and simulation data for the production of recoil protons. From top to bottom they are: distribution of recoil angles, distribution of recoil energies and the recoil angles as a function of the (normalized) energy.*

5 Experimental vs simulated data: proton irradiation

At the beginning of this chapter, the intent of the comparison between experimental and simulated data will be explained, both as initially planned and as at the end was performed. Then the focus will be on what can be inferred by the study.

5.1 Objective of the comparison

The irradiation with protons should have given data about the capability of the analysis of CR-39 using Politrack™ of discriminating the protons at different energies and angles. As already introduced in Section 513.1.1, such experimental aims indeed to quantify to which degree of precision the LET and the impinging angle assessments are performed through the Politrack™ system, and what are then the key factors driving the eventual uncertainties. Under the assumption of a properly characterized system (including a correct calibration), the expected result was to have a series of holes, all with very similar characteristics. This in turns means an expected LET_{nc} distribution with a very sharp peak at a variable position dependant on the energy and incidence angle of the protons. The peak was expected to move to lower mean LET values as the energy of the irradiating particles grows, because higher energies correspond to a lower energy transfer.

The analysis was set to have two different steps and goals.

1) A first one by comparing the different dosimeters and the relative peaks, to investigate the resolution of the analysis. If, for example, the peaks relative to two different energies are at the same LET_{nc} value, there may be some problems with the capability of this system to discriminate protons with different energies.
2) By then setting the same conditions in the simulation (energy, angle, and removed later) the goal was to achieve an LET_{sim} distribution with a peak around the same position of the experimental one. In case the two did not match, the plan was to find and fix bugs in the code in order to improve the methods and reproduce better and better the experimental data.

As already explained in Section 3.1.2, this has not been possible, and a different approach has been tried. The dosimeters used in this work indeed are not well characterized, lacking a good calibration. Without knowing the removed layer, it is impossible to use these dosimeters to compare experimental and simulation data in any way.

The approach used in this work aims at finding a value of the track etching rate which gives similar peak values for both the experimental and simulated LET distributions. In other simple words, this can be seen as an indirect calibration of the dosimeters using the simulation. It is well-known by the author of this work that a real calibration using this method is not possible until the simulation is proven to be working. This method indeed has been used just as an indirect way to test the features of the simulation. Neither a positive result would imply a validation of the simulation, even if it would be a good news, nor a negative one would certainly mean that the simulation may be improved, since it may be due to a problem related to the analysis.

5.1.1 Method

As explained in Section 2.3, the Politrack™ analysis relies on the initial setting of the bulk etching rate. Using this value, the system can assess the LET_{nc} value of the track from its morphology. Changing the value of the V_b, then, the LET_{nc} distribution changes and can differ a lot from the real one if the value of the removed layer is wrong, hence the importance of a reliable calibration.

To find a V_b suitable for the different irradiation conditions, the method used has been to progressively change the value of the bulk etching rate for both the analysis performed with Politrack™ and the simulation, and to register the correspondent LET_{nc} value of the peak, starting from the 1,5 MeV-irradiated dosimeters etched for 70 minutes (cf. **Table 5-1** and **Figure 5.1**). Once the V_b has been found, it can be used for the other conditions (energy and etching time) to see if the peaks match again or not.

In principle if the system works properly, the result should be that, using the same value of bulk etch rate, all the experimental values match the correspondent simulations, because the code should be efficient enough to reproduce the experimental processes.

5.2 Results

Progressively changing the V_b value for both the experimental data and the simulation, it is possible to fill in **Table 5-1** and draw the graph of **Figure 5.1**. In this table, the peak values are presented for both experimental and simulated data, meaning the value of the most “occupied” bin of the distribution. This has been taken as reference value for the comparison just because all the distributions are peaks, and this is the best figure to compare all of them.

***Table 5-1**: Values of experimental and simulated peak value as a function of the bulk etching rate for 1,5 MeV protons shot perpendicularly with respect to the detector surface and after an etching of 70 minutes.*

V_b	h	LET_{nc} peak value (keV/µm)	LET_{sim} peak value (keV/µm)
7,28	8,5	52	40
7,71	9	44	40
8,15	9,5	37	39
8,57	10	31	39
9	10,5	27	39

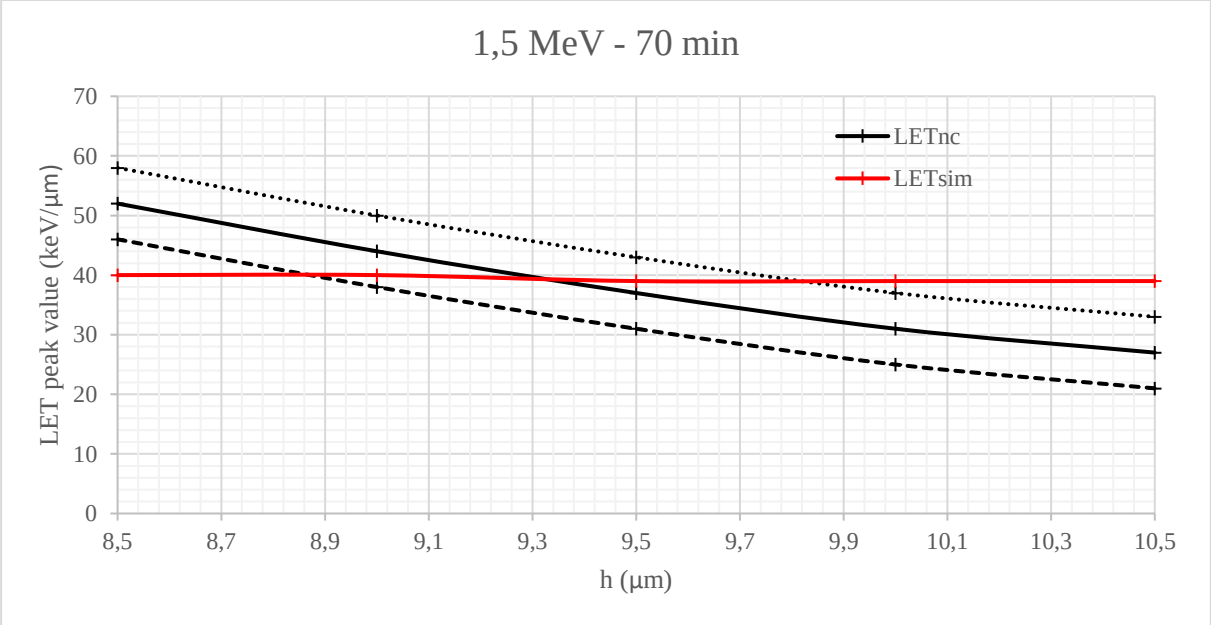

***Figure 5.1** – Trend of the LET peak value with respect to the removed layer, for both the simulations and the experimental data. Dosimeters irradiated with protons at 1,5 MeV and etched for 70 minutes. Dotted lines correspond to the LET_{nc} line plus or minus the standard deviation.*

There are three very important things that can be easily highlighted:

- The experimental peak value highly depends on the removed layer. This confirms once again that the calibration of the system is very important and upon this relies the whole dose assessment.
- The simulated peak value does not change too much. This flat trend is not what expected. Looking at the Bragg curve for these protons (cf. **Figure 5.2**) in fact, one can see that 1,5 MeV protons entering CR-39 have a residual range of 37,2 µm and an LET of 25,1 keV/ µm.

  After 10 µm, the LET is not too different (around 29,5 keV/µm), meaning that the energy deposition is both low and almost constant in this part of the proton path. This

could explain a small difference between the LET_{nc} distributions but not a clear equivalence.

- Taking into account also the standard deviation (cf. **Figure 5.1**), one can see that actually the interval where the result of experimental and simulated distributions could match is very broad: from 8,8 to 9,8 circa.

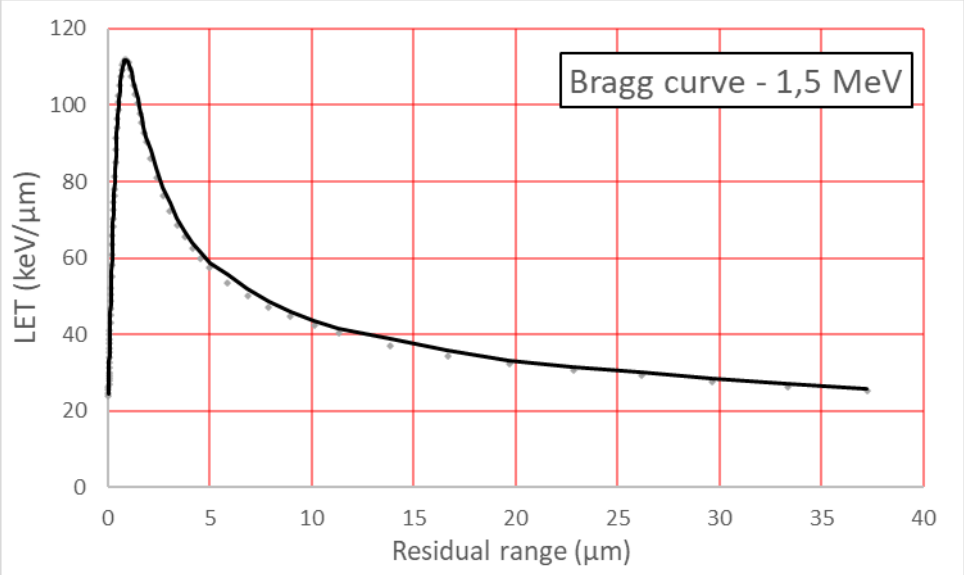

Figure 5.2 *– Bragg curve for protons in CR-39 entering the surface at 1,5 MeV. (Source SRIM)*

The comparison between the two distributions is shown in **Figure 5.3**, after choosing as value for the removed layer 9,5 µm (thus $V_b = 8{,}15\ \mu m/h$). The two distributions have been

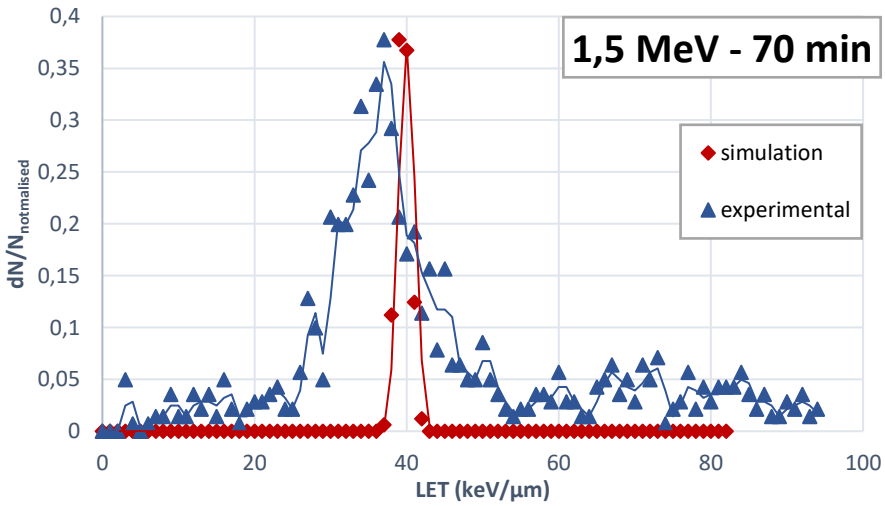

Figure 5.3 *– LETnc and LETsim distributions for an irradiation with protons at 1,5 MeV and 70 minutes of etching time.*

normalized so that the *dN/N* of the two peak values are the same. In the graph it is possible to see that the two distributions are both peaked, ate the values of $LET_{nc} = 37\ keV/\mu m$ and

$LET_{nc} = 39 \pm 1\ keV/\mu m$ but the simulated one is much sharper because does not take into account the resolution of the Politraclk™ system, and, to a lesser extent, defects, the background radiation, and other secondary events.

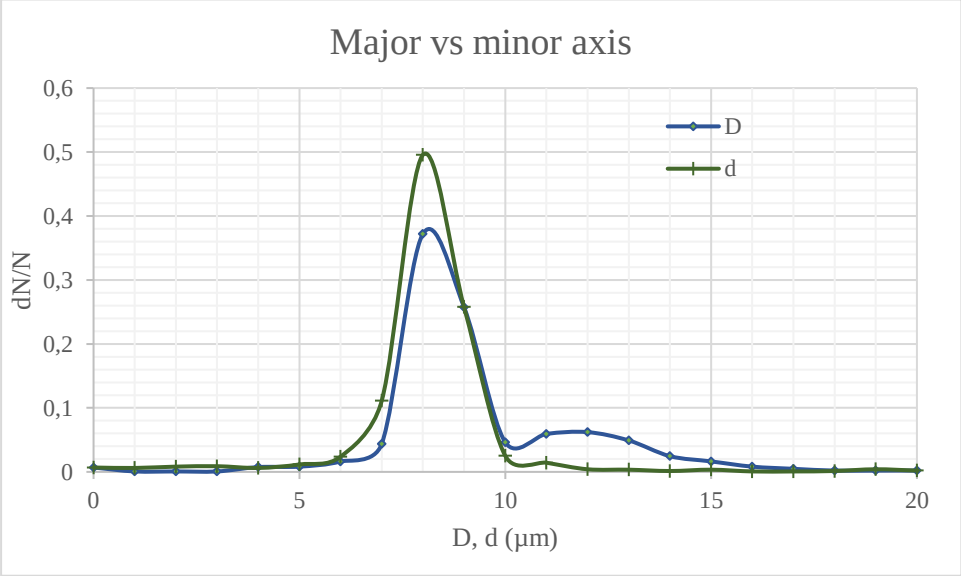

Figure 5.4 *– Major and minor axes distribtuions for dosimeters irradiated with protons at 1,5 MeV and etched for 70 minutes.*

Actually, these effects are probably negligible, because **Figure 5.4** shows that the axes distributions are very sharp, narrow, and almost equal, meaning that essentially all the tracks have similar diameters and a circular shape (the characteristic of normal incidence, exactly like

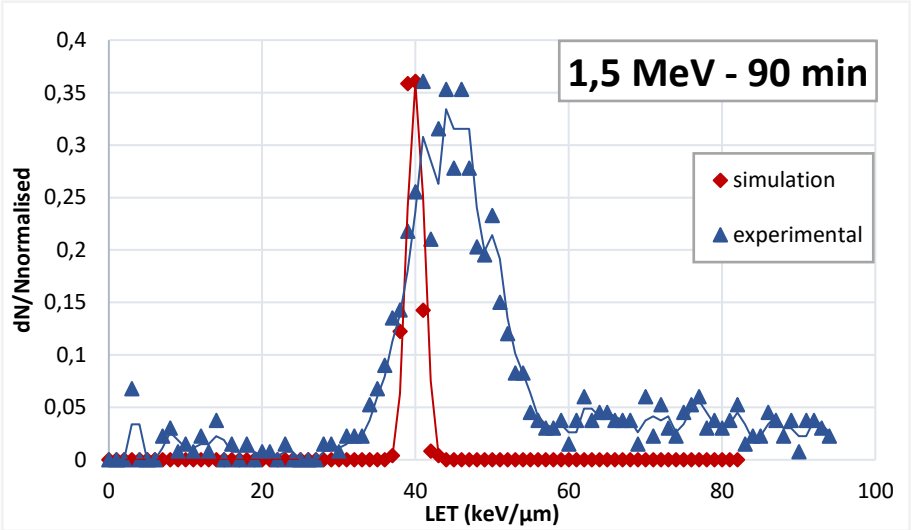

Figure 5.5 *– LET_{nc} and LET_{sim} distributions for an irradiation with protons at 1,5 MeV and 90 minutes of etching time.*

the protons).

Applying then the same $V_b = 8{,}15\ \mu m/h$ to the case of 1,5 MeV protons but 90 minutes of etching time, the result is the graph presented in **Figure 5.5**. Here the two peaks are still close,

since the experimental presents the peak at $LET_{nc} = 43 \pm 3\ keV/\mu m$, while the simulated one is at 40 keV/µm.

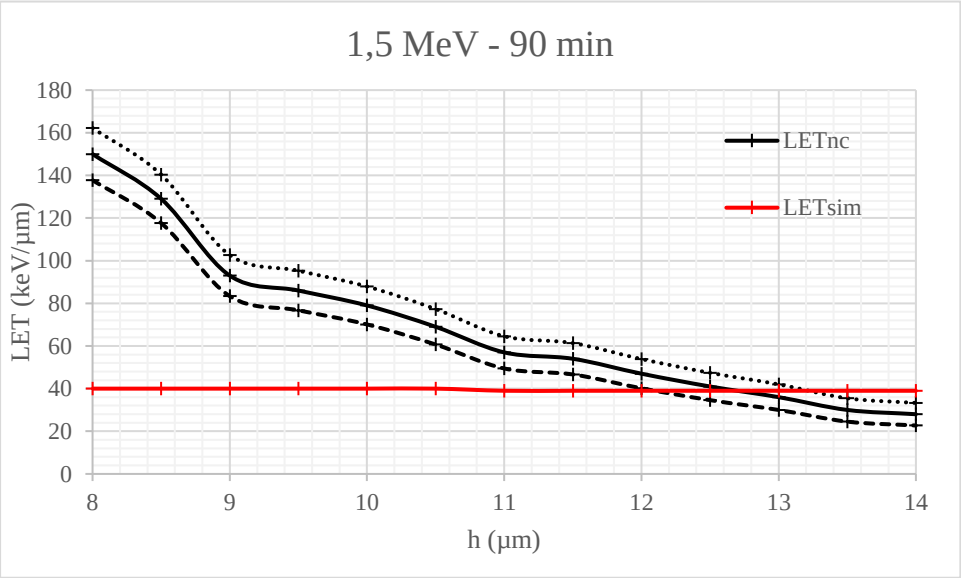

Figure 5.6 *– Trend of the LET peak value with respect to the removed layer, for both the simulations and the experimental data. Dosimeters irradiated with protons at 1,5 MeV and etched for 90 minutes. Dotted lines correspond to the LETnc line plus or minus the standard deviation.*

Even for these dosimeters, the good estimation of V_b has an important effect on the correct assessment of the LET, as **Figure 5.6** clearly shows.

If for the 1,5 MeV the distributions are quite consistent, the comparison between experimental and simulation data for the 2,5 MeV / 90 min shows the existence of some problem using $V_b = 8{,}15\ \mu m/h$ as calculated above.

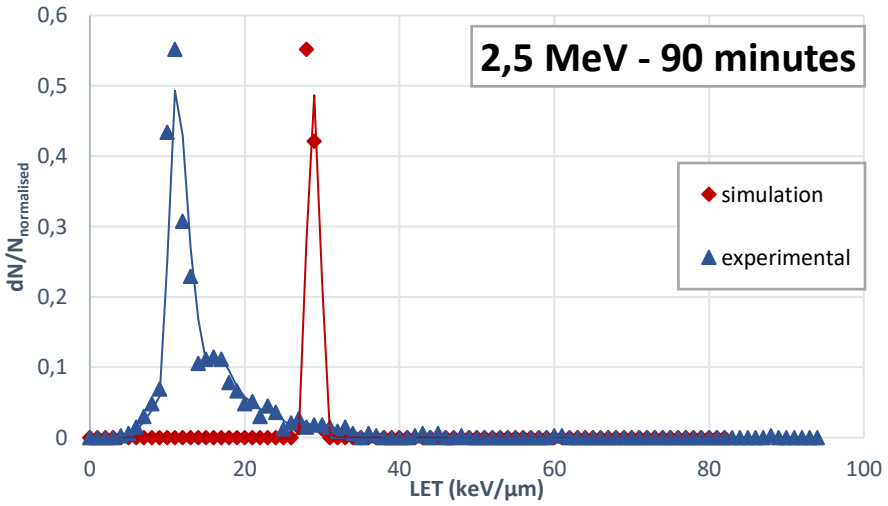

Figure 5.7 *– LETnc and LETsim distributions for an irradiation with protons at 2,5 MeV and 90 minutes of etching time.*

In **Figure 5.7** in fact it is possible to see the quite large difference in the peak value between the two distributions, where $LET_{nc} = 11 \pm 1\ keV/\mu m$ and $LET_{sim} = 28\ keV/\mu m$.

In **Figure 5.8**, once again the huge importance of the good estimation of V_b on the assessment of the LET distribution is showed.

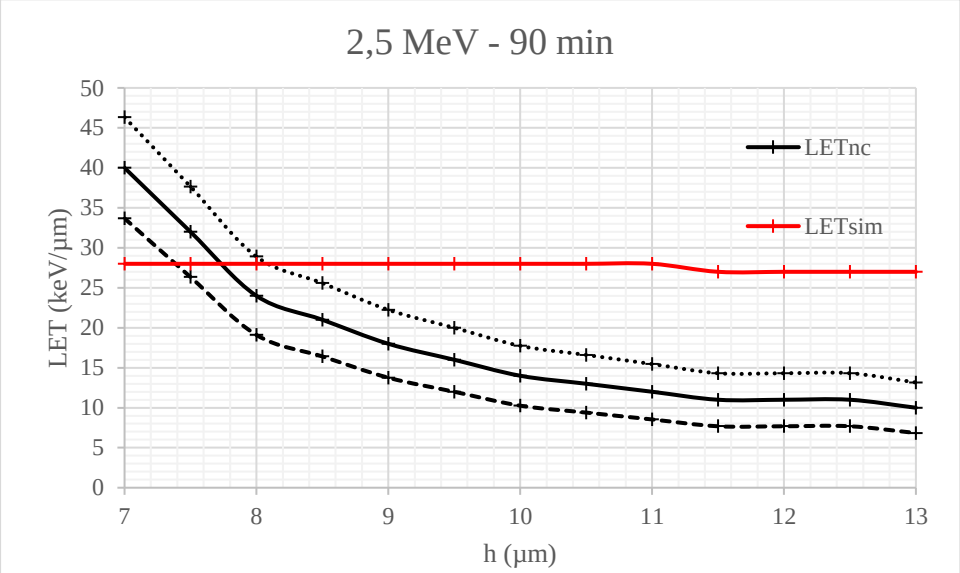

Figure 5.8 *– Trend of the LET peak value with respect to the removed layer, for both the simulations and the experimental data. Dosimeters irradiated with protons at 2,5 MeV and etched for 90 minutes. Dotted lines correspond to the LETnc line plus or minus the standard deviation.*

To sum up, it is evident that there are differences between experimental and simulated data for both the energies considered but it is impossible to determine if an error is present and, if so, where it is.

A possible source of error can be present in the relation between V and LET used by both the Politrack™ and the simulations, that is eq. (2-8). Here, the range $1{,}04 < V < 2{,}1$, covering mainly the LET values characteristic of protons, has not been experimentally tested unlike the

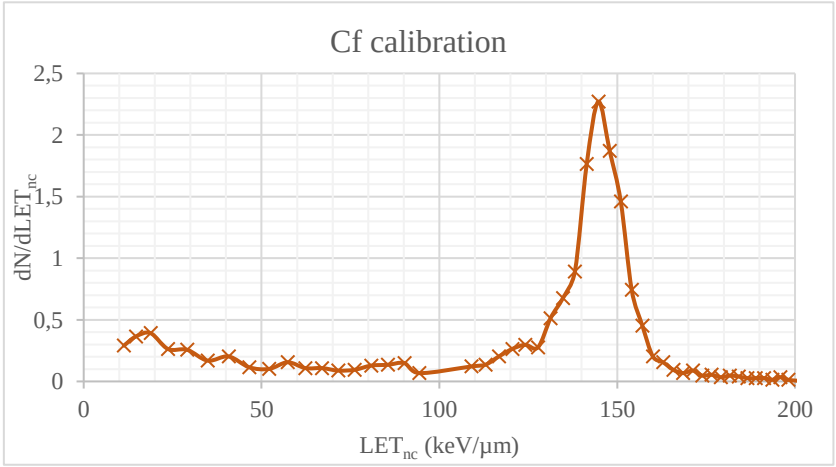

Figure 5.9 *- LET_{nc} distribution of a CR-39 dosimeter irradiated using a Cf calibration source.*

other ranges. Taking as a reference the calibration irradiations using a Cf source, the LET_{nc} distribution obtained is the one shown in **Figure 5.9**. This source emits alpha particles which cover an LET range different from the protons (cf. **Figure 5.10**) and which has been already tested.

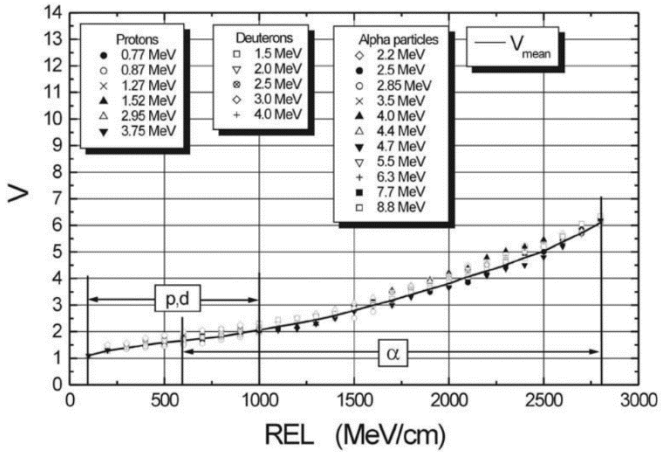

Figure 5.10 *– Etch rate ratio, V, as a function of restricted energy loss, REL, for protons, deuterons and alpha particles of various initial energy. (Source: B. Dörschel, D. Hermsdorf, K. Kadner, S. Starke, Dependence of the etch rate ratio on the energy loss of light ions in CR-39, Radiation Measurements, 35, pp.287- 292, 2002).*

This clearly explains the reasons why a necessary irradiation was planned and studied in detail as shown in Section 3.1.1, and the impact that the shutdown of all the research facilities had on this work. In fact, this irradiation using a microbeam could have been very useful also to test the validity of eq. (2-8), which is a necessary step in the enhancement of neutron personal dosimetry in this energy range.

This can be however a basis for future development of this work, by performing the planned irradiations. Once the useful data will be collected, they can be studied more in detail since the code for simulation has already been written. Successive works in fact can focus on the enhancement and improvement of the code on the basis of reliable experimental data.

6 Experimental vs simulated data: neutron irradiations

This chapter will show the study of both experimental and simulation data in the case of a neutron irradiation. It will be divided into three parts, the first two for experimental and simulation analyses separately and the last for the comparison between the two.

6.1 Presentation of the analyses

Despite the lack of the proper irradiation planned for this work, the number and type of dosimeters implied in this work is still satisfying, since they cover a good energy range and they belong to two different irradiation campaigns, as shown in **Table 6-1**. Moreover, unlike the dosimeters irradiated with protons, both the irradiation campaign these dosimeters come from, have a reliable calibration, thus a well-characterized value of the removed layer.

Facility	Particle	Energy	Etching time	Removed layer
AMANDE	neutron	565 keV	90 min	15 µm
		2,5 MeV	90 min	15 µm
		5 MeV	90 min	15 µm
National Physical Laboratory (NPL)	neutron	565 keV	90 min	19,5 µm
		1,2 MeV	90 min	19,5 µm
		2,5 MeV	90 min	19,5 µm
		5 MeV	90 min	19,5 µm

***Table 6-1**: Dosimeters used for this work.*

It is even possible an initial comparison between them. In fact, having dosimeters irradiated during separate irradiation campaigns in two different facilities (and thus etched independently) for each of the three energies, we can study the producibility of the LET assessment. If, for example, both dosimeters show the same behaviour, then the reliability is high. For this reason, initially, the discussion will focus on the study of the experimental data coming from the analysis of the dosimeters, to move then to data obtained through the simulations, to finally present a comparison between them.

The studied is focused mainly on three parameters: one is obviously the LET_{nc} and the other two are the major and minor axes. The last two have been chosen because they will be very useful to understand the effectiveness of the simulation. As shown in Section 2.3.2 and 4.3.3, they are indeed at the basis of the calculation of both LET_{nc} and LET_{sim}. Thus, we will initially

see the trends for the experimental data of these three distributions, then the same will be done for the data produced through the simulation, and finally it will be presented a comparison between experimental and simulated distributions.

6.2 Analysis of experimental data

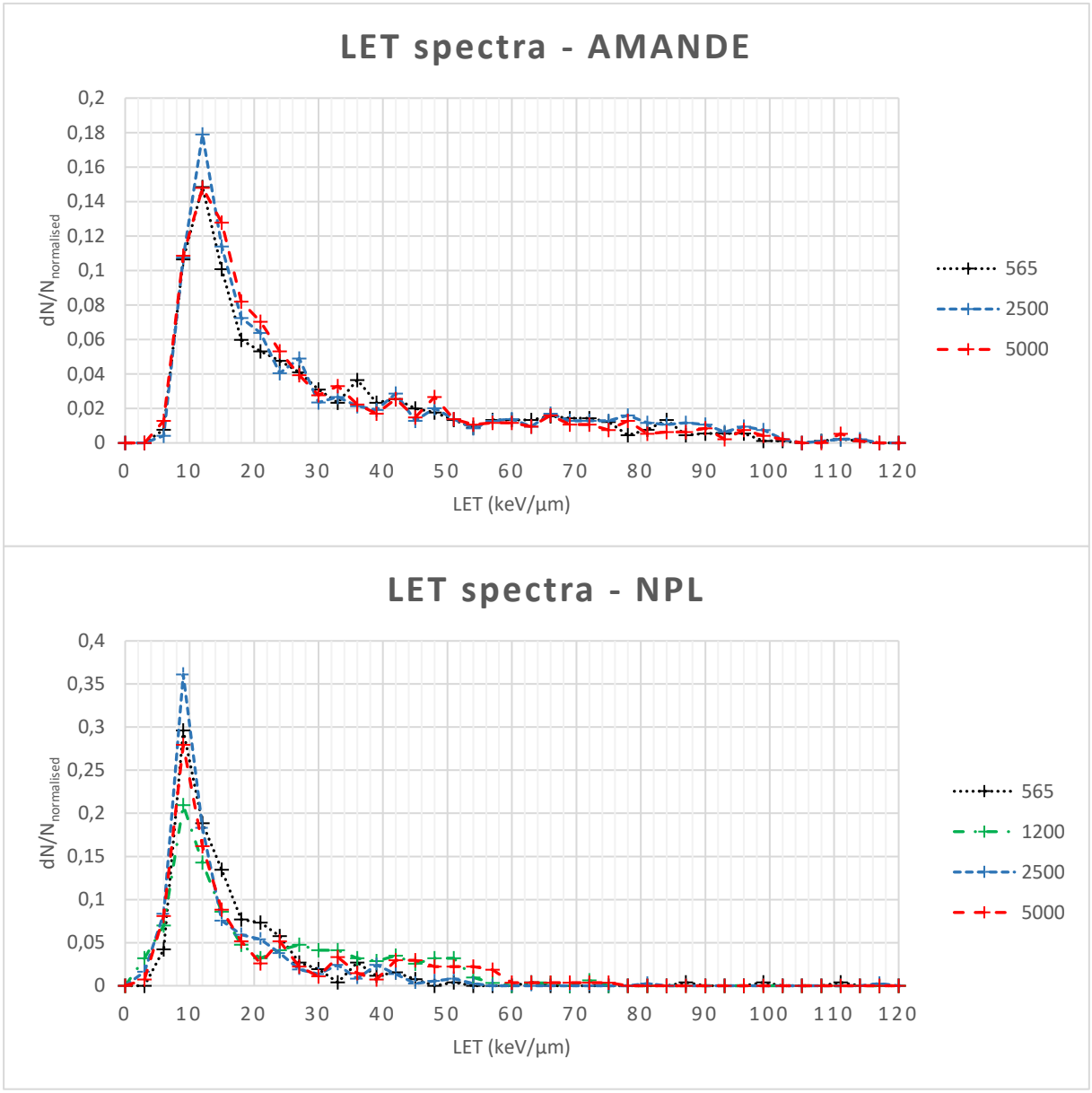

Figure 6.1 *– LET_{nc} spectra for AMANDE and NPL dosimeters irradiated at various energies.*

The first step of the analysis of all the experimental data has been to filter them out. In fact the raw data produced by the Politrack™, as explained in Section 2.3.2, has been filtered, trying to eliminate as much as possible the background, and without eliminating the neutron tracks at the same time. To do so, two different filters have been used, explained below.

- $V_{recalculated} < 2{,}2$: this value corresponds roughly to the maximum LET the protons can have. Above this threshold, the tracks can be produced only by heavier particles, like radon.
- $residual < 20$: the residual is a measure of the distance among the track contour points and the ones of the fitted ellipse. In other words, it is an estimation of how much the contour differs from an ellipse, thus lower numbers mean better fit. This filter is useful to eliminate those tracks coming from defects and scratches in the glass.

After applying the filters, the data corresponding to dosimeters irradiated at different neutron energies can be compared between them to understand if there are significative changes in the LET_{nc} distributions. Such changes could give hints about the possibility to use the dosimeters for a rough spectroscopy. This has been done for the dosimeters irradiated both at AMANDE and NPL facilities.

Looking at **Figure 6.1** it is easy to understand that all the dosimeters unfortunately show exactly the same behaviour, with a peak at very low LET values (high energy recoil protons) and a long tail of tracks up to 120 keV/µm for the AMANDE dosimeters and 60 keV/µm for the NPL ones. There is nothing which can be recognized as a clear trend, except for the fact that in both cases 1200 keV is the energy which gives back the spectrum with the highest number of tracks in the bin corresponding to the peak, while the ones related to 565 and 5000 keV are almost equal and lower. This, for now, is clearly not enough to base a spectroscopic method on.

Another thing to note is that the position of the peak is exactly the same between dosimeters belonging to the same irradiation campaign, while differs when compared to another campaign, being 12 keV/µm for the AMANDE's irradiation and 9 keV/ µm for NPL's. This may be due to differences between the specific etching processes, imperfect estimations of the removed layer, uneven fading times or due to differences in CR-39 material as well.

Anyway, the consistency of the trend is remarkable and gains in reliability as it is shown by dosimeters which have been irradiated in two different facilities, etched in two distinct laboratories and analysed by two diverse Politrack™ devices. However, without further data, it is not possible to understand why this happens and if it is possible to modify the system in such a way to have different spectra for different energies.

It may also be interesting to see a comparison between the distributions of major and minor axes of the fitted ellipse, and how they change with the energy. This comparison is presented

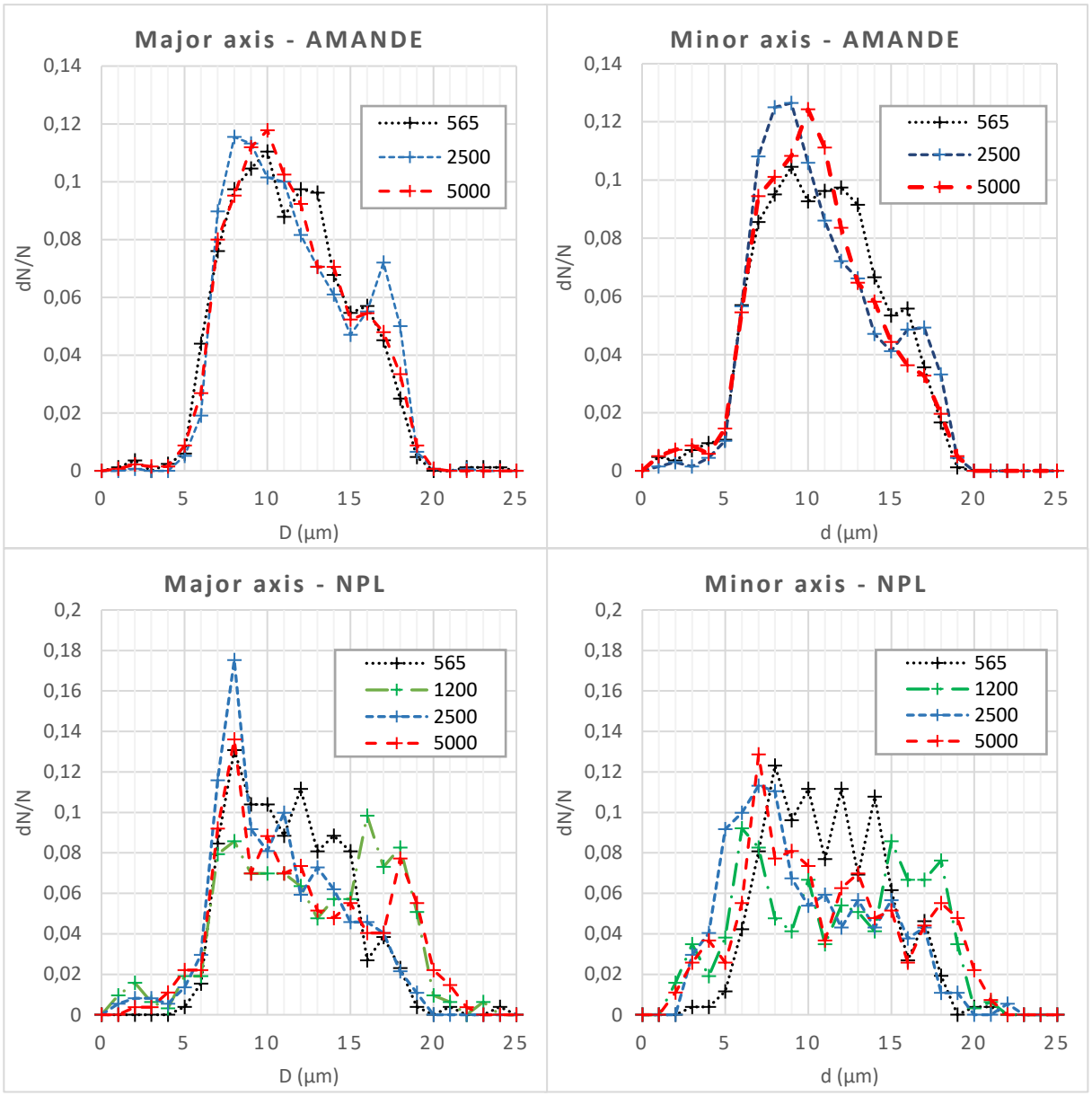

Figure 6.2 *– Major and minor axis distributions for various energies for both AMANDE and NPL irradiation campaigns.*

in **Figure 6.2**. Looking at the data and especially AMANDE's, it is possible to realise that the distributions do not change much with the energy and are quite similar between them. In fact, looking at **Figure 6.3** which presents the distribution of the ratio between *d* and *D*, it is evident that, for the majority of the tracks, this ratio lies in the bin between 0,9 and 1. This means that the tracks have a section very similar to a circle instead of an oblong ellipse.

As a reference, let us take the same distribution in a very different case (cf. **Figure 6.4**), that is a calibration dosimeter, irradiated with a ^{252}Cf α particles source, having a peak in the emission spectrum of 6.1 MeV. It is important to underline that the two situations are very different because the way α particles release energy is very different from the one of neutrons. Anyway, it may be interesting to see the difference with respect to a reference dosimeter.

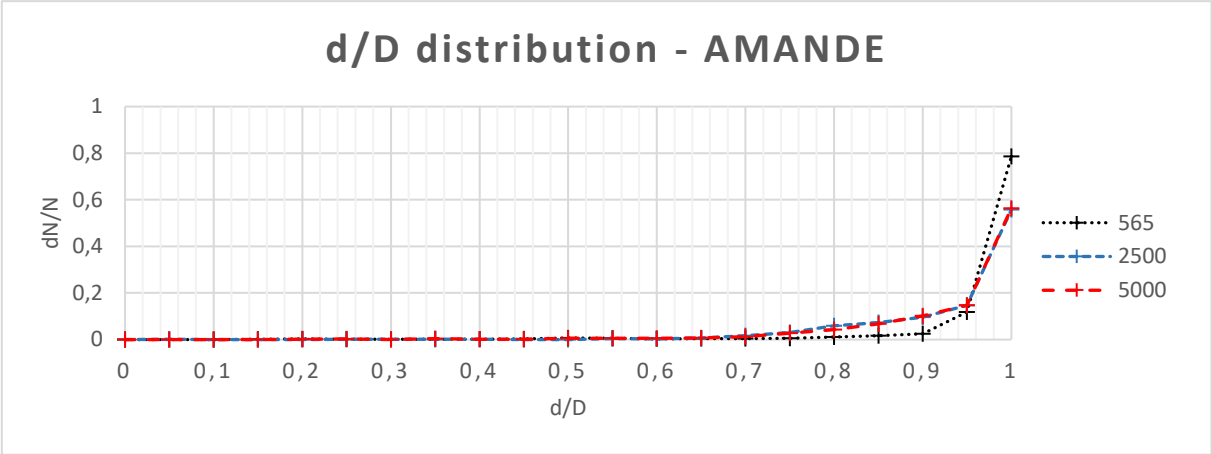

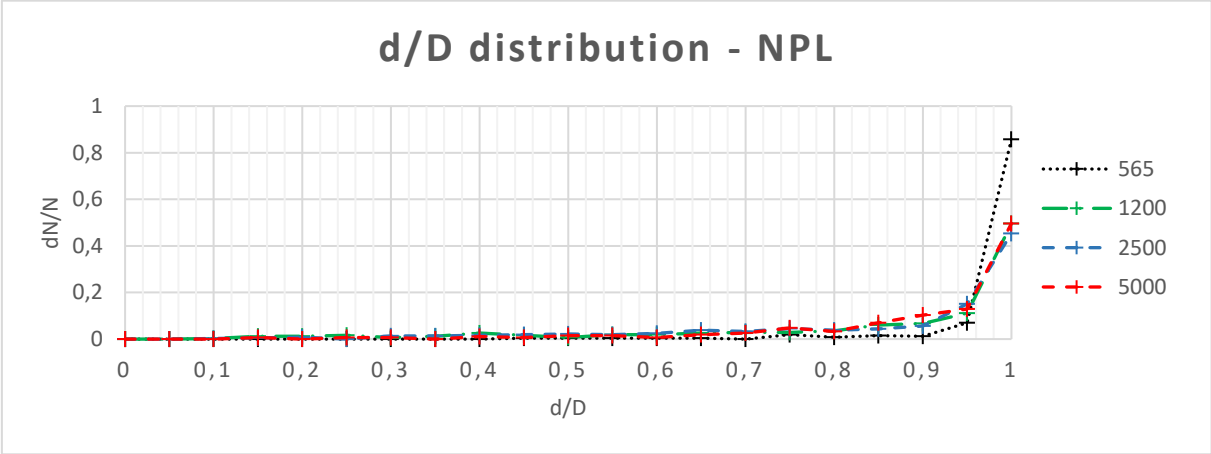

Figure 6.3 *– Distribution of the ratio between minor and minor axis among the tracks of the dosimeters irradiated both at AMANDE and NPL.*

In this case the ratio distribution covers a much broader range of values in an almost uniform way, meaning that the holes are in most of the cases more similar to ellipses than circles. The difference is quite impressive and highlights the disproportion between the highest bin and the others in the experimental data.

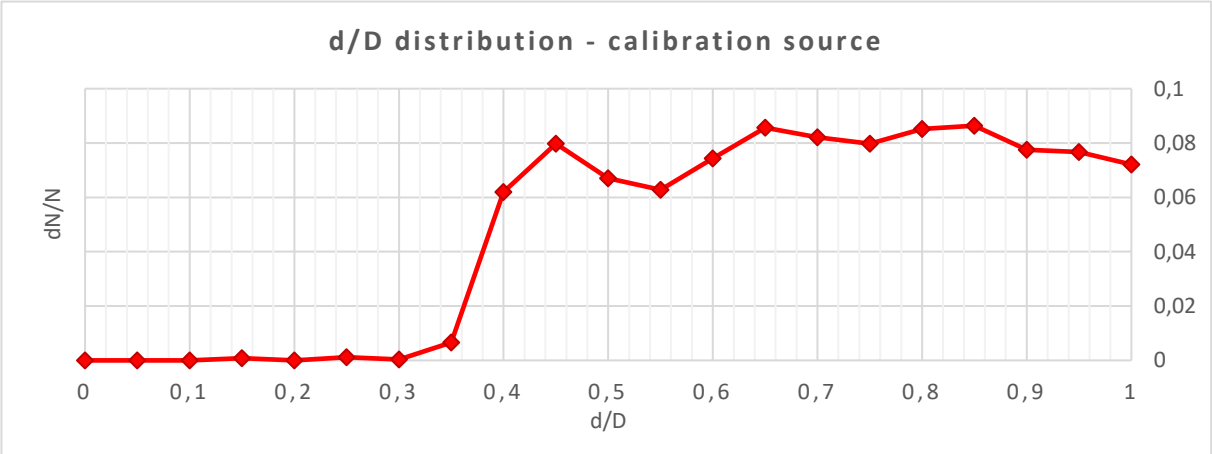

Figure 6.4 *– Distribution of the ratio between minor and minor axis among the tracks of the dosimeters irradiated using a ^{252}Cf calibration source .*

There are two main reasons for the tracks to have a circular shape: in case of overetching and of perpendicular incidence of the recoil proton. However, it is not possible to state why this happens without a study of the behaviour of the dosimeters exposed to a proton irradiation. Another study that can be performed to investigate this behaviour is to try different etching times to understand if these distributions change. 15 and especially 19,5 µm are deep removed layers, and as *h* increases the higher the probability of overetched tracks. Studying the variation of the signal with respect to the removed layer, can explain the reason of the trend previously shown.

6.3 Analysis of simulation data

As explained in Section 4.3.3, the output of a simulation is a file full of information about each single "digital" track. Among the various classes of data, which can anyway be changed rewriting few lines of the code to select whatever the user prefers, the three tracks' characteristics used in this analysis are the major and minor axes and obviously the LET_{sim}. These three have been chosen in order to be able to compare the same three figures.

Several simulations have been performed, all with the same geometry, just changing the energy of the primary neutrons. The energies chosen are the reference ones as defined in the ISO

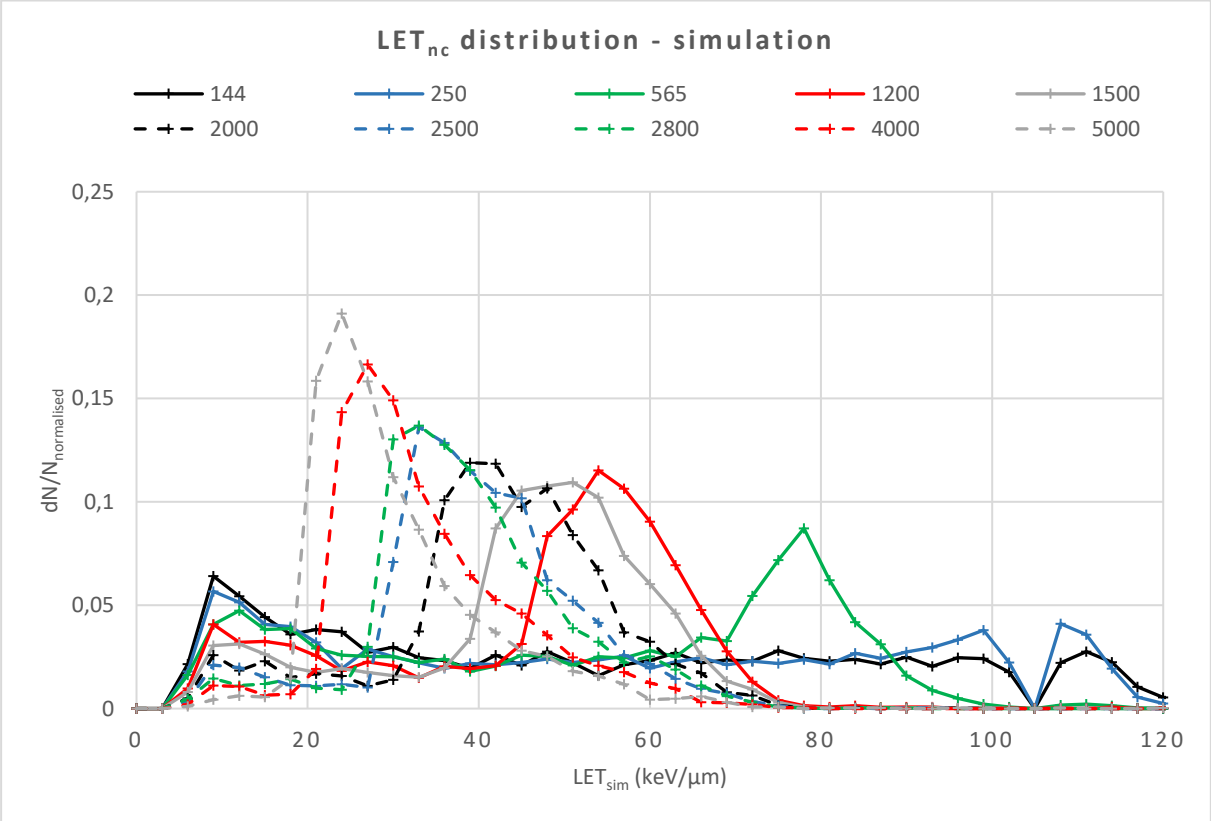

***Figure 6.5** – LET_{sim} distribution for various energies, calculated with the simulation built in GEANT4.*

standard[28], which are the same that can be produced at AMANDE and NPL, with the addition of two more (2 and 4 MeV) not to have too large gaps.

Starting from the LET_{sim}, shown in **Figure 6.5**, one can immediately notice that the distributions are very different with respect to the experimental ones. The simulations produce LET_{sim} distributions which have a quasi-homogeneous distribution at low energies (144 and 250 keV). Then a peak starts to appear, which grows in importance and moves to lower LET values as the incident neutron energy grows, while the contribution at high LET is less and less important until totally disappears. These distributions follow a behaviour which is, in principle, theoretically reasonable, namely protons at higher energies have lower LET values.

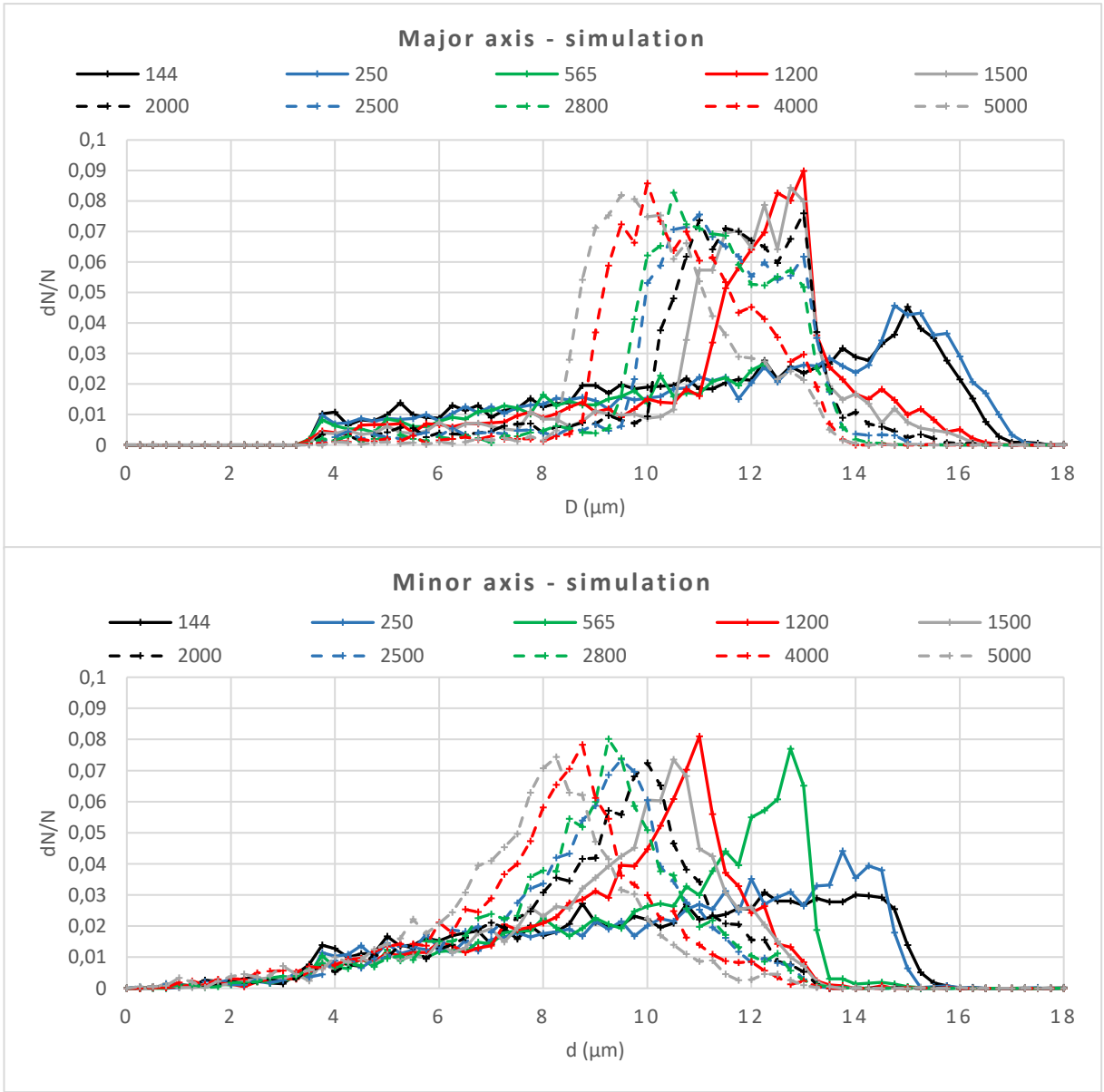

Figure 6.6 *– Major and minor axis distributions for various energies, calculated with the simulation built in GEANT4.*

Looking also at the distributions of major and minor axes in **Figure 6.6**, it is evident that the behaviour is different from the experimental one since for every energy the trend is different. Moreover, the distributions of the minor axes cover a dimension range which is shifted to lower values than the one of the major axes, especially at higher energies. This tells us another important fact and difference with respect to the experimental data, that is to say these simulated tracks have perimeters different from circles and more similar to oblong ellipses.

Figure 6.7 shows how the ratio d/D changes as the energy decreases, where some energies have been omitted in order to have a better comprehension of the general behaviour. At low energies, the recoil protons produced have a very low range inside CR-39 and release all the energy in a

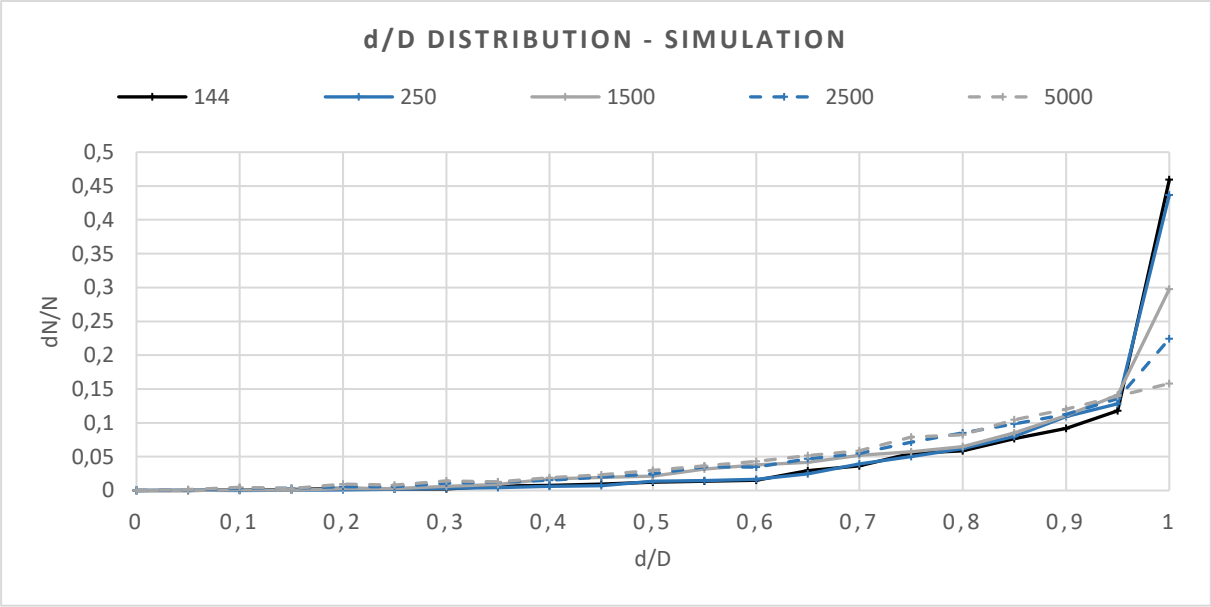

Figure 6.7 *– Evolution of the axes ratio distribution as the energy increases.*

short path which rarely will cross the removed layer surface. For this reason, the latent tracks will be mostly overetched and thus with an almost circular perimeter. As the energy increases, the recoil protons will have longer and longer paths and the possibilities for them to cross *h* will be higher. This is why the ratio distribution, which initially has by far as most probable values those between 0,9 and 1, flattens as the energy increases. This trend is similar to the one shown in **Figure 6.4** by experimental data, where the dosimeters irradiated with neutrons at 565 keV have the highest value of the bin between 0,9 and 1, even if the flattening is less gradual.

On the basis of the trend shown in **Figure 6.7**, it is possible to state that, even if at high energies the LET_{sim} shifts to low values, tending to superimpose to experimental data, the physical events promoting the two distributions are different. This is explained indeed by the fact that in the

case of experimental data, most of the tracks have a circular shape, while for the simulated one this is not true.

6.4 Experimental vs simulated data

From the two previous sections, it is clear that experimental and simulated data are very different, but it may be anyway interesting to see a comparison between each of the energies available. This kind of study has been performed only for the dosimeters irradiated in the AMANDE facility because the number of primary neutrons absorbed is higher, thus the information has a better statistical reliability.

6.4.1 565 keV

µIn the case of primary neutrons shot at 565 keV, the two LET distributions are kind of mirrored, with one presenting a peak in the lower part of the spectrum and the other the opposite

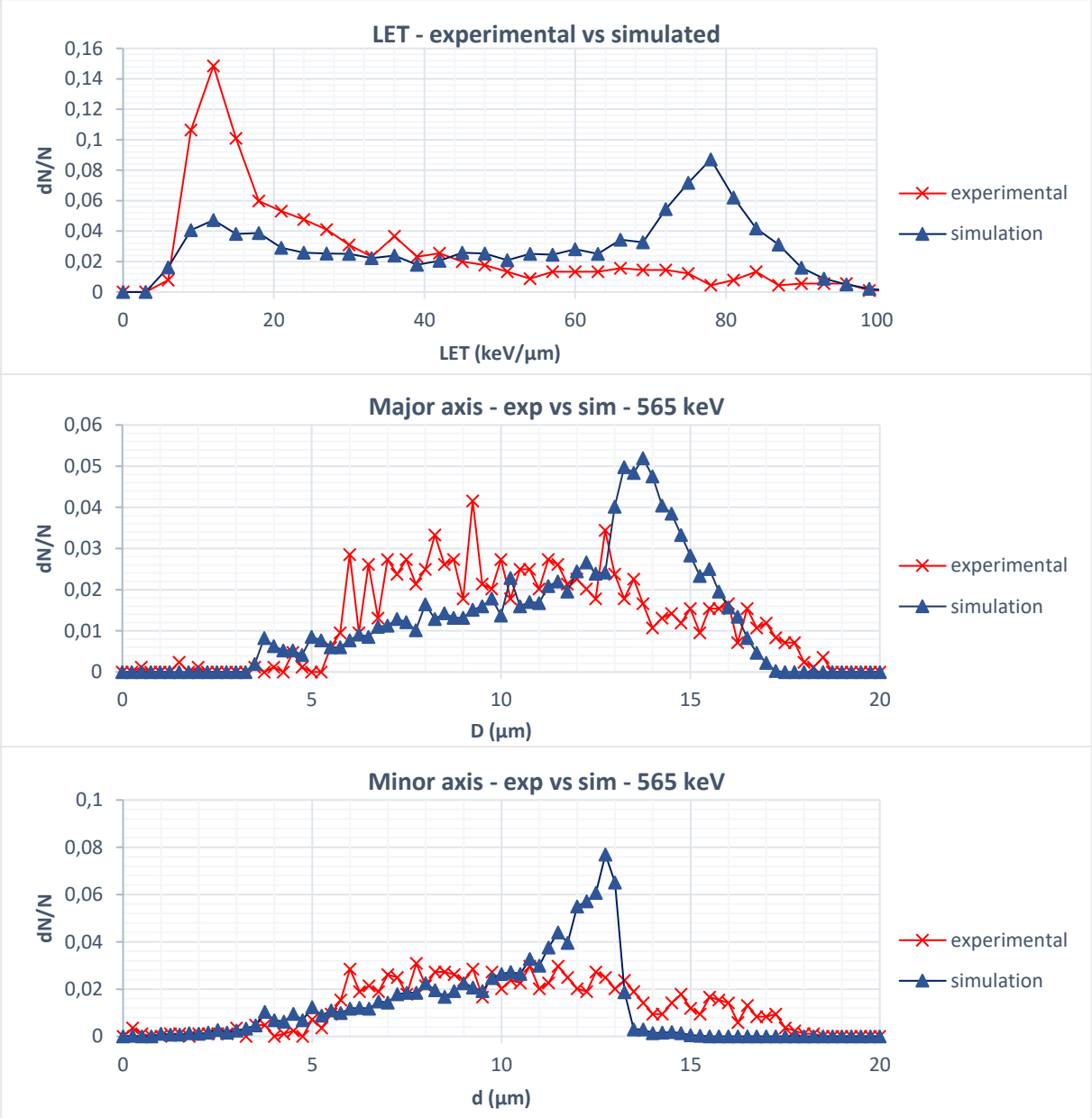

Figure 6.8 *– Comparison between experimental and simulated data for 565 keV primary neutrons.*

(cf. **103Figure 6.8**).

This difference is illustrated also by the axes. It seems like the simulation exaggerates a single kind of event, while misses other typologies. The first statement is justified by the presence of a peak absent in the experimental distributions, the latter by the steep decrease of the minor axis distribution. Anyway, without further studies it is not possible to understand what produces such differences.

6.4.2 2500 keV

At 2,5 MeV the distributions have a similar trend with just a shift in LET as shown in **Figure 6.9**, but the discrepancy is once again better highlighted looking at the differences in the axis distributions. Here, as in the case of 565 keV neutrons, the simulations cover a much narrower range of lengths, showing again a misrepresentation of the real events happening in the irradiation. In fact, again, instead of producing a uniform distribution, the simulations display two tight peaks one shifted with respect to the other.

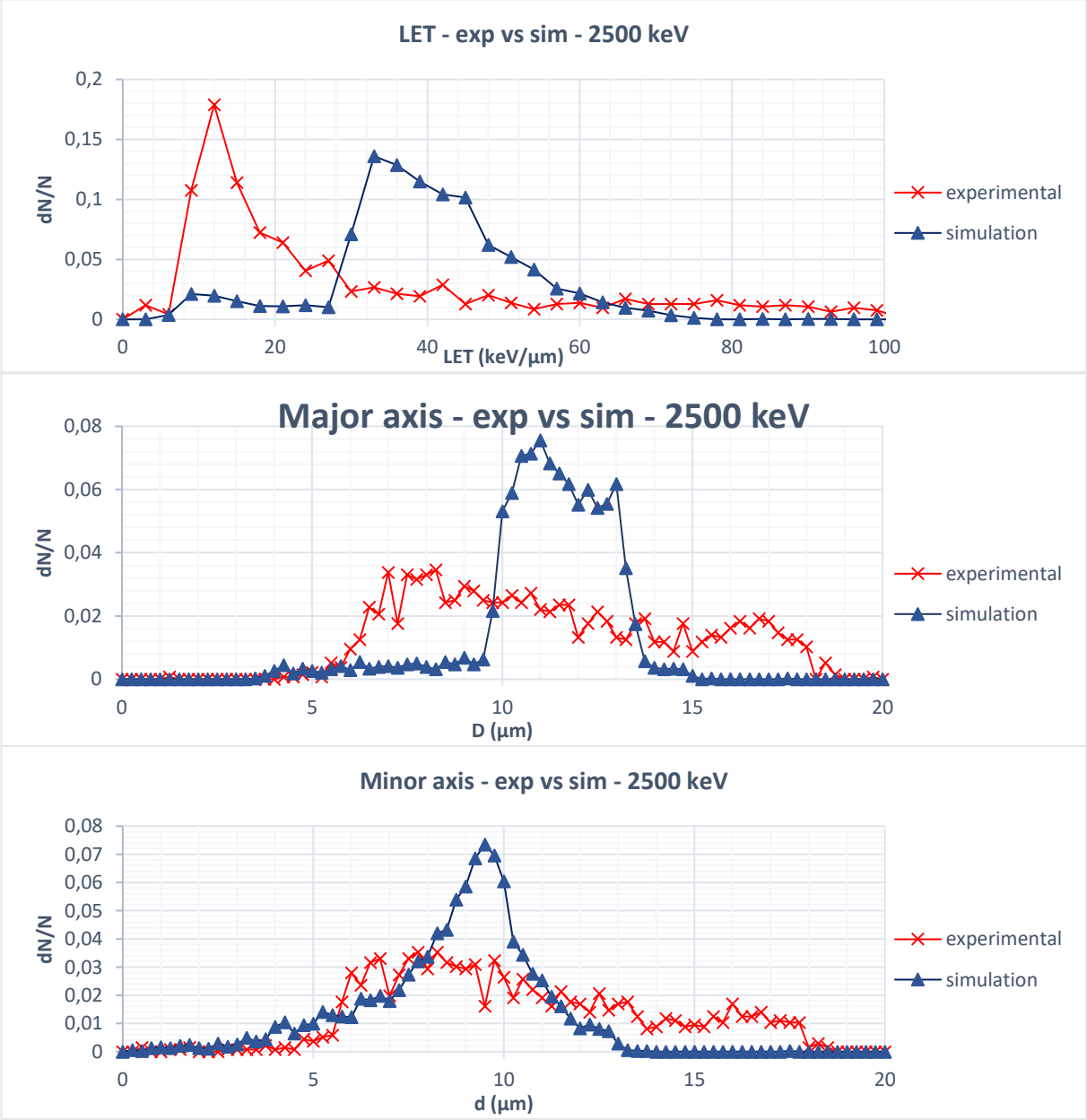

Figure 6.9 *– Comparison between experimental and simulated data for 2500 keV primary neutrons.*

6.4.3 5000 keV

The situation for the irradiation at 5 MeV is essentially the same as the one at 2,5 MeV, with just everything downscaled because at higher energies the LET is lower, and along with it also the major and minor axes of the etched tracks.

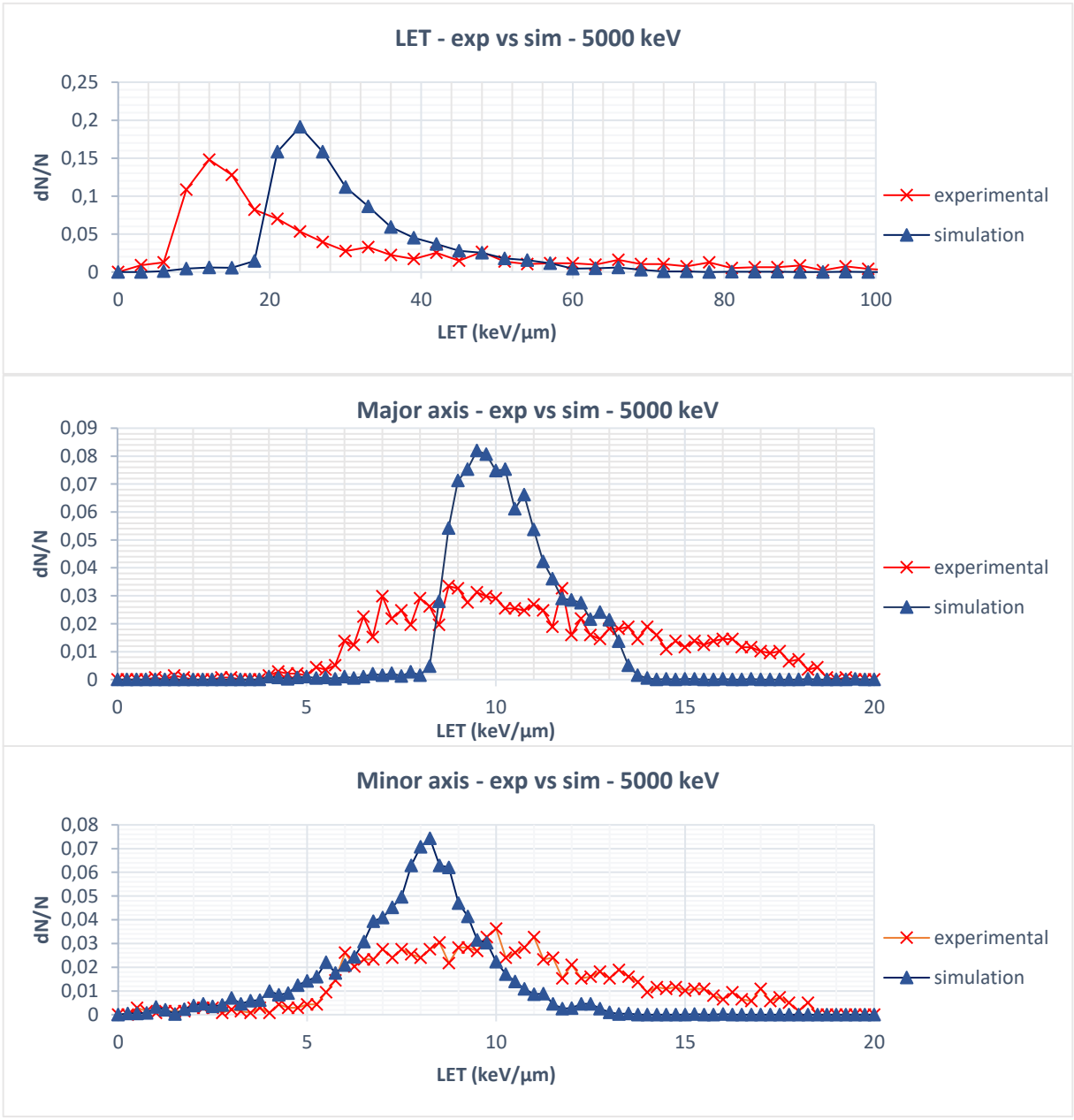

Figure 6.10 *– Comparison between experimental and simulated data for 5000 keV primary neutrons.*

7 Conclusions and future development

This chapter contains final notes about the work, considerations about the studies performed in the two previous chapters and ideas to further prosecute this work in the future.

7.1 Main results and conclusion

The primary objective of this thesis work was to enhance neutron individual monitoring performed using SSNTDs based on CR-39. To do so, the question of the possibility to have a rough spectroscopy of neutron fields in workplaces through the topology of the etched tracks was raised. A better understanding of the LET_{nc} spectra could help to flatten the dose response as a function of the incident neutron energy. Thus, two questions have been investigated:

- Is it possible to measure the energy of protons through the morphology of the tracks that they produce, and with which precision?
- Is there a link, from a theoretical point of view, between the incident neutron field and the LET distribution of the tracks induced in the CR-39? If so, is it possible to have an information on the neutron field (energy and angular distribution) using the LET_{nc} spectra?

To answer to these questions, two studies were performed:

- An experimental one, during which detectors already irradiated using monoenergetic proton and neutron fields were analysed using the Politrack™ system.
- A computational one, where a simulation environment has been coded using the C++ language and the Geant4 toolkit to be able to reproduce the LET spectra of Politrack™ the best way possible.

On the basis of the analysis presented in Chapter 6, it is possible to state that the goal has been reached only in part and in a preliminary way. As for as the experimental spectra, no discrimination is possible as a function of the incident neutron energy, meaning that it is not possible to retrace the energy of the primary neutrons not even in the very simple monoenergetic cases considered in this work. Furthermore, thanks to the availability of data from two different irradiation campaigns, it is possible to state that this is the actual behaviour of Politrack™ with a high degree of confidence.

Even if these experimental distributions are counterintuitive and an obstacle for the achievement of the final goal, they have been obviously taken as a fact and as reference for the

ideal distribution to achieve through the simulations. Nonetheless it is legitimate to question whether ways to achieve more functional distributions exist.

From the computational point of view, the simulations did not match the experimental LET_{nc} distributions, but they can produce meaningful distributions in the right LET_{sim} range (cf. **Figure 6.5**), between 0 and slightly less than 120 keV/µm.

Another promising characteristic of the simulations is that they show peaks at progressively lower LET_{sim} values, and this is a predicted and reasonable trend. Moreover, in the energy range considered, this behaviour is always consistent, with a gradual passage from an almost flat distribution to a peaked one.

All these elements are positive and represent a basis for a future development of this code. Obviously, it is necessary to understand the discrepancies between experimental and simulated LET spectra. In fact, looking at the various major and minor axes distributions (cf. **Figure 6.8** and following) it seems like some kind of event happening in a real irradiation gets underestimated or totally neglected by the simulations.

7.2 Perspectives

Since the goal has not been reached with the conclusion of this thesis work, it is interesting to illustrate the reasons why, according to who is writing this dissertation, it may be reasonable to move forward and continue the study and how this should be done. There are good arguments for both the experimental and the simulation part which will be illustrated in the following.

7.2.1 Experimental part

It is clearly necessary that spectra related to neutrons at different energies should have different trends, otherwise a real discrimination is impossible. For this reason, to actually carry on this method to achieve information on the components of the spectrum, it is crucial to study in better detail the experimental spectra, trying to identify why the different energies produce all the same distributions. There are two main reasons not to settle for the spectra obtained in this study and try to obtain better results, one related to the theory of track production and one to the results of this work.

From a theoretical point of view, in fact, as the energy of the primary neutrons grows, also the fraction of protons at high energies grows, along with obviously the maximum energy of these secondaries (cf. **Figure 4.18**). This very basic explanation is a physical fact and is what justified

this thesis work. What was learned at the end of this study is that the physical fact does not easily translate into a corresponding difference in the track morphology. Without a proton irradiation, anyway, it is not possible to state whether the limit of the method is this one or a type of event underestimated. So, it is mandatory to understand, in the first instance, if protons produce different damages (this was one of the studies expected for this work, but unfortunately it has not been possible). Moreover, monoenergetic proton irradiations are of major interest as they are a tool to understand the degree of uncertainty on the LET measurement through a series of very reliable irradiations. They will also be a way to investigate the resolution of the measurement of the minor and major axes through the Politrack™ optical system.

In parallel, the spectra obtained through the simulations give hopeful signs about a final achievement of the proposed goal, even if obviously the most reliable information is the one contained in the experimental data. These simulations, which rely on a physical model, in fact clearly show that the damages produced by different energies should lead to different morphologies of the tracks. This obviously is not enough to not trust experimental data but maybe can at least give good reasons to study in better detail the dynamics of track formation in this energy range.

7.2.2 Simulation part

The simulations are often just an approximation of the reality and during their development many compromises are done. In this specific case, the first thing which can be changed to enhance the results is the model of track etching dynamics. The model used has been developed starting from the premise that V_t has a constant value along the track length, which is indeed an approximation.

Many theories have been developed for the morphology of the tracks, and in this work the easiest has been chosen for time constraints. Initially, in fact, the simulation had a different philosophy which was changed not long before the deadline for the work. For this reason, it was not possible a real and extensive study of which was the most convenient model to use, which is indeed necessary for a future enhancement of the code.

Fortunately, the simulation has been built with a modular philosophy as explained in Chapter 4, in order to make possible such a modification of the code. The model for the morphology itself can be changed at any time by just “asking” the right parameters to the code and writing the right equations.

Even if, after future studies, a convergence between experimental and simulation data will not be reached, this code can still be used for estimations of absorbed dose by the dosimeters and to study in detail the history of protons inside CR-39. This thanks to the already cited characteristics of the simulation, and with limited modifications of the code.

7.3 Final notes

The cancelation of the initial planned irradiation campaign due to the SARS-CoV-2 lockdown has been very detrimental for the achievement of the final goal, especially due to the absence of the expected data about protons, as explained in Chapter 3. It has been quite difficult to develop such a work, which was initially intended to be heavily relying on experimental studies, in an uncertain sanitary situation and during a period of lockdown. In particular it was confirmed the importance of an investigation of the V-LET dependency in the proton region. Such investigation was foreseen in the original workplan using the microbeam of MIRCOM, but eventually did not take place.

Anyway, on the basis of the data collected and the work done, some interesting conclusions can and have be drawn; probably less than the initial premises, but this work has anyway made steps forward toward the understanding of the subject and will hopefully be a basis for more efficient future studies. Hopefully, future studies can demonstrate that dose assessment with CR-39 dosimeters and the Politrack^{TM} system can progress in the sense here proposed, to protect people more efficiently.

Appendix A: the code

The code is composed by several classes, each one (except for the SSNTDAnalysis one) with a header file (.hh) where the class is defined and with a source file (.cc) where the instructions using the class are actually given. The classes are the following:

- SSNTDDetectorConstruction: the geometry of the simulation is set;
- SSNTDDetectorMessenger: the maximum length of the steps is defined;
- SSNTDPhysicsList: the physics models are chosen and recalled;
- SSNTDPrimaryGeneratorAction: the source is set;
- SSNTDAnalysis: the analysis instruments are recalled and defined;
- SSNTDActionInitialization: the simulation is iniatialized;
- SSNTDRunAction: the structure of the run is defined and what happens at the beginning and end of it set;
- SSNTDEventAction: the structure of the event is defined and what happens at the beginning and end of it set;
- SSNTDSteppingAction: the structure of the step is defined and what happens at the beginning and end of it set;

It may be very useful to present the whole code, but it would take too much space. For this reason, this section will show the code for the two main characteristic class' source files, where most of the calcuslation related to this work is performed.

A.1 SSNTDSteppingAction.cc

```
#include <vector>
#include "SSNTDSteppingAction.hh"
#include "SSNTDEventAction.hh"
#include "SSNTDRunAction.hh"
#include "SSNTDDetectorConstruction.hh"
#include "G4Track.hh"
#include "G4Step.hh"
#include "G4Event.hh"
#include "G4RunManager.hh"
#include "G4LogicalVolume.hh"
#include "G4SystemOfUnits.hh"
#include "G4ParticleDefinition.hh"

SSNTDSteppingAction::SSNTDSteppingAction(SSNTDEventAction* eventAction)
   : G4UserSteppingAction(),
     fEventAction(eventAction),
     fScoringVolume1(0),
     fScoringVolume2(0)
{}
```

```
SSNTDSteppingAction::~SSNTDSteppingAction()
{}

void SSNTDSteppingAction::UserSteppingAction(const G4Step* step)
{
   // Initialization of vectors
   G4StepPoint* preStepPoint = step->GetPreStepPoint();
   G4StepPoint* postStepPoint = step->GetPostStepPoint();
   G4Track* Track = step->GetTrack();

   // first of all we initialize the details about the step
   // Particle name
   std::string ParticleName = Track->GetDynamicParticle()->GetParticleDefinition()->GetParticleName();
   // Event number
   G4int eventID = G4EventManager::GetEventManager() -> GetConstCurrentEvent()->GetEventID();
   G4double parentID = Track->GetParentID();
   G4double trackID = Track->GetTrackID();
   // Step number
   G4int stepNumber = Track->GetCurrentStepNumber();
   // Position
   G4ThreeVector preposition = preStepPoint->GetPosition();
   G4ThreeVector postposition = postStepPoint->GetPosition();
   // TrackLength
   G4double deltax = Track->GetStepLength();
   // kinetic energy, energy deposit
   G4double ekin = preStepPoint->GetKineticEnergy();
   G4double ekinfin = postStepPoint->GetKineticEnergy();
   G4double edepStep = step->GetTotalEnergyDeposit();
   // Angle
   G4ThreeVector direction = Track->GetMomentumDirection();
   G4double teta=asin(abs(direction.x())/direction.mag());

   //here we control to be inside the dosimeter or the converter and neglect other particles
   if (!fScoringVolume1)
   {
      const SSNTDDetectorConstruction* detectorConstruction
            = static_cast<const SSNTDDetectorConstruction*>
            (G4RunManager::GetRunManager()->GetUserDetectorConstruction());
      fScoringVolume1 = detectorConstruction->GetScoringVolume1();
   }
   if (!fScoringVolume2)
   {
      const SSNTDDetectorConstruction* detectorConstruction
            = static_cast<const SSNTDDetectorConstruction*>
            (G4RunManager::GetRunManager()->GetUserDetectorConstruction());
      fScoringVolume2 = detectorConstruction->GetScoringVolume2();
   }

   // get volume of the current step
   G4LogicalVolume* volume
         = step->GetPreStepPoint()->GetTouchableHandle()
         ->GetVolume()->GetLogicalVolume();
   //G4cout<<"here"<<G4endl;
   // check if we are in scoring volume ---> if protons simulated, comment the next two lines
   if (((volume != fScoringVolume1) && (volume != fScoringVolume2)) && (ParticleName!="neutron") &&
(parentID!=0))
   {step->GetTrack()->SetTrackStatus(fKillTrackAndSecondaries); return;}

  //here the vectors are filled
   if (ParticleName=="proton")
```

```
    {
      fEventAction->vpID.push_back(trackID);
      fEventAction->vpStepNumber.push_back(stepNumber);
      fEventAction->vpPrePosition.push_back(preposition);
      fEventAction->vpPostPosition.push_back(postposition);
      fEventAction->vpDeltaX.push_back(deltax);
      fEventAction->vpEkin.push_back(ekin);
      fEventAction->vpEkinFin.push_back(ekinfin);
      fEventAction->vpEdepStep.push_back(edepStep);
      fEventAction->vpTeta.push_back(teta);
    }

    if (ParticleName=="e-")
    {
      if (stepNumber==1)
      {
        fEventAction->vePrePosition.push_back(preposition);
        fEventAction->veEkin.push_back(edepStep);
      }
    }
}
```

A.2 SSNTDEventAction.cc

```
#include "SSNTDEventAction.hh"
#include "SSNTDAnalysis.hh"
#include "SSNTDRunAction.hh"
#include "SSNTDSteppingAction.hh"

#include "G4RunManager.hh"
#include "G4Event.hh"
#include "G4ios.hh"
#include "G4Track.hh"
#include "G4TrackStatus.hh"
#include "G4Step.hh"
#include "G4ThreeVector.hh"

SSNTDEventAction::SSNTDEventAction(SSNTDRunAction* runAction)
   : G4UserEventAction(),
     fRunAction(runAction)
{}

SSNTDEventAction::~SSNTDEventAction()
{}

void SSNTDEventAction::BeginOfEventAction(const G4Event* /*event*/)
{
   Edep=0.*keV;
   EdepSec=0.*keV;
   xMax=0.*um;
   Vmean=0.;
   TrackLength=0.*um;

   InitialPosition.setX(0.);
   InitialPosition.setY(0.);
   InitialPosition.setZ(0.);
   FinalPosition.setX(0.);
   FinalPosition.setY(0.);
   FinalPosition.setZ(0.);
```

```
    LinearizedLength.setX(0.);
    LinearizedLength.setY(0.);
    LinearizedLength.setZ(0.);

    vpID.clear();
    vpParticleName.clear();
    vpStepNumber.clear();
    vpPrePosition.clear();
    vpPostPosition.clear();
    vpDeltaX.clear();
    vpEkin.clear();
    vpEkinFin.clear();
    vpEdepStep.clear();
    vpTeta.clear();
    veID.clear();
    vePrePosition.clear();
    vePostPosition.clear();
    veEkin.clear();
}

void SSNTDEventAction::EndOfEventAction(const G4Event* /*event*/)
{
    G4double DX[] = {-dx+h,+dx+h};
    G4int eventID = G4EventManager::GetEventManager() -> GetConstCurrentEvent()->GetEventID();
    G4double LET2,t0,f0,f1,w0,w1;
    Energyat0=0.;
    Energyath=0.;
    LETsim=0.;
    alfa=0.;
    LET=0.;
    RANGE=0.;
    d=0.;
    d1=0.;
    d2=0.;
    h1=0.;
    D=0.;
    D1=0.;
    D2=0.;
    D3=0.;
    H1=0.;
    H2=0.;
    std::size_t size =vpPrePosition.size();
    G4double R=0.;
    G4double r=0.;
    G4double K=0.;
    G4double V=0.;
    G4bool particle =false;


    const  G4double ekinBin[] ={
1*keV,1.1*keV,1.2*keV,1.3*keV,1.4*keV,1.5*keV,1.6*keV,1.7*keV,1.8*keV,2*keV,2.25*keV,2.5*keV,2.75*
keV,3*keV,3.25*keV,3.5*keV,3.75*keV,4*keV,4.5*keV,5*keV,5.5*keV,6*keV,6.5*keV,7*keV,8*keV,9*keV,
10*keV,11*keV,12*keV,13*keV,14*keV,15*keV,16*keV,17*keV,18*keV,20*keV,22.5*keV,25*keV,27.5*ke
V,30*keV,32.5*keV,35*keV,37.5*keV,40*keV,45*keV,50*keV,55*keV,60*keV,65*keV,70*keV,80*keV,90*
keV,100*keV,110*keV,120*keV,130*keV,140*keV,150*keV,160*keV,170*keV,180*keV,200*keV,225*keV,
250*keV,275*keV,300*keV,325*keV,350*keV,375*keV,400*keV,450*keV,500*keV,550*keV,600*keV,650*
keV,700*keV,800*keV,900*keV,1000*keV,1100*keV,1200*keV,1300*keV,1400*keV,1500*keV,1600*keV,1
700*keV,1800*keV,2000*keV,2250*keV,2500*keV,2750*keV,3000*keV,3250*keV,3500*keV,3750*keV,400
0*keV, 4500*keV,5000*keV,5500*keV,6000*keV,6500*keV};
```

```
   const G4double RANGEbin[] ={
0.0263*um,0.0287*um,0.0312*um,0.0336*um,0.0360*um,0.0383*um,0.0407*um,0.0430*um,0.0453*um,0.049
9*um,0.0554*um,0.0609*um,0.0663*um,0.0716*um,0.0768*um,0.0819*um,0.0869*um,0.0919*um,0.1016*um
,0.1110*um,0.1201*um,0.1290*um,0.1377*um,0.1462*um,0.1626*um,0.1783*um,0.1930*um,0.2081*um,0.22
22*um,0.2360*um,0.2494*um,0.2624*um,0.2752*um,0.2877*um,0.2999*um,0.3237*um,0.3523*um,0.3799*u
m,0.4066*um,0.4326*um,0.4580*um,0.4829*um,0.5073*um,0.5313*um,0.5783*um,0.6244*um,0.6697*um,0.7
144*um,0.7588*um,0.8030*um,0.8912*um,0.9799*um,1.0700*um,1.1600*um,1.2500*um,1.3500*um,1.4500*
um,1.5500*um,1.6500*um,1.7600*um,1.8600*um,2.0900*um,2.3900*um,2.7000*um,3.0400*um,3.3900*um,3.
7600*um,0.1500*um,4.5600*um,4.9800*um,5.8800*um,6.8400*um,7.8700*um,8.9500*um,10.100*um,11.300
*um,13.870*um,16.660*um,19.660*um,22.830*um,26.150*um,29.650*um,33.340*um,37.210*um,41.260*um,
45.500*um,49.920*um,59.300*um,72.030*um,85.860*um,100.79*um,116.79*um,133.85*um,151.96*um,171.0
9*um,191.25*um,234.53*um,281.78*um,332.9*um,387.85*um};

   // This command eliminates particles having unusual behaviours
   if      (vpStepNumber.size()==0)          {G4EventManager::GetEventManager()->GetConstCurrentEvent()-
>IsAborted(); return;}

   // This command eliminates events where two particles are produced
   // in the sensitive depth. It can be interesting to find a way to separe
   // them, but maybe this happens too rarely to be useful
   for (std::size_t j=0; j<size; j++)
   {
      if  (vpID[j]!=vpID[j+1])  {G4EventManager::GetEventManager()->GetConstCurrentEvent()->IsAborted();
return;}
   }

   // Here we sample the energy at the interface for those crossing,
   // or the initial energy fort the auto-radiation
   if (vpPrePosition[0].x()<=0)
   for (std::size_t j=0; j<size; j++)
   {
      if ((vpPrePosition[j].x()>=-0.10*um) && (vpPrePosition[j].x()<=0.1*um))
      {
         Energyat0=vpEkin[j];
         InitialPosition=vpPrePosition[j];
      }
   }
   if (vpPrePosition[0].x()>=0)
   {
      Energyat0=vpEkin[0];
      InitialPosition=vpPrePosition[0];
   }


   // ROUTINE FOR FORWARD PARTICLES //

   if (vpPrePosition[0].x()<h)
   {
      if ((vpPrePosition[1].x()>vpPrePosition[2].x()) || (vpPrePosition[size-1].x()<0) )
      {G4EventManager::GetEventManager()->GetConstCurrentEvent()->IsAborted(); return;}

      // this is to set if the particle crosses the etched depth (so if
      // it is underetched)
      for (std::size_t  j=0; j<size;j++)
      {
         if ((vpPrePosition[j].x()<=DX[1]) && (vpPrePosition[j].x()>=DX[0]))
         {
             particle = true;
         }
      }
```

```
      //here the code fixes the Vmean value
      if (((vpPrePosition[size-1].x()>=0) && (vpPrePosition[size-1].x()<DX[0])) || (particle==true))
      {
         RANGE=(InitialPosition-vpPrePosition[size-1]).mag();
         LET=Energyat0/RANGE;

         // Compute the maximum depth
         LET2 = LET*LET;
         LET3 = LET2*LET;
         LET4 = LET3*LET;
         LET5 = LET4*LET;
         LET6 = LET5*LET;
         Vmean =(-2e-12*LET6+1e-9*LET5-2e-7*LET4+2e-5*LET3-0.001*LET2+0.0322*LET+0.8998);
         // this is the filter for the angle
         if      (sin(vpTeta[0])<1/Vmean)      {G4EventManager::GetEventManager()->GetConstCurrentEvent()-
>IsAborted(); return;}
      }
   }

   // ROUTINE FOR BACKSCATTERED PARTICLES //

   if (vpPrePosition[0].x()>h)
   {
      if (vpPrePosition[1].x()<vpPrePosition[2].x())
      {G4EventManager::GetEventManager()->GetConstCurrentEvent()->IsAborted(); return;}
      for (std::size_t  j=0; j<size;j++)
      {
         if ((vpPrePosition[j].x()<=DX[1]) && (vpPrePosition[j].x()>=DX[0]))
         {
            G4int i=0;
            do
            {
               t0=ekinBin[i-1];
               t1=ekinBin[i];
               f0=LETBin[i-1];
               f1=LETBin[i];
               w0=RANGEbin[i-1];
               w1=RANGEbin[i];
               i= i+1;
            } while (t1 <= vpEkin[j] );

            alfa = (vpEkin[j]-t0)/(t1-t0);
            // LET = (f0*(1-alfa)+(f1*alfa));
            RANGE = (w0*(1-alfa)+(w1*alfa));
            LET=vpEkin[0]/RANGE;
            LET2 = LET*LET;
            LET3 = LET2*LET;
            LET4 = LET3*LET;
            LET5 = LET4*LET;
            LET6 = LET5*LET;
            Vmean          =(-2.3393e-12*LET6+1.1623e-9*LET5-2.2226e-7*LET4+2.0827e-5*LET3-9.9256e-
4*LET2+3.2121e-2*LET+8.9995e-1);
            if     (sin(vpTeta[0])<1/Vmean)     {G4EventManager::GetEventManager()->GetConstCurrentEvent()-
>IsAborted(); return;}
            if     (Vmean==0)     {G4EventManager::GetEventManager()->GetConstCurrentEvent()->IsAborted();
return;}
         }
      }
```

```
    }

// here the particles not capable of leaving a track are eliminated
    if (Vmean==0) {G4EventManager::GetEventManager()->GetConstCurrentEvent()->IsAborted(); return;}

    // Here the calculation of the morphology starts, based on the theory
    // of Somogyi and Szalay for constant Vt

    G4double R0=vpPrePosition[size-1].x();

    // as first thing let's set the values for the conditionw
    h1=R0/Vmean+R0*sin(vpTeta[0]);
    H1=R0/Vmean+R0*(Vmean*sin(vpTeta[0])-1)/(Vmean-sin(vpTeta[0])+
          cos(vpTeta[0])*(sqrt(Vmean*Vmean-1)));
    H2=R0/Vmean+R0*(Vmean*sin(vpTeta[0])-1)/(Vmean-sin(vpTeta[0])-
          cos(vpTeta[0])*(sqrt(Vmean*Vmean-1)));

    // now let's calculate the morphology
    // D
    D1=2*h*(sqrt(Vmean*Vmean-1)/(Vmean*sin(vpTeta[0])+1));
    D3=2*sqrt(R0*(sin(vpTeta[0])-1/Vmean)*(2*h-R0*(sin(vpTeta[0])+1/Vmean)));
    D2=0.5*(D1+D3)+(R0-(h*Vmean/(Vmean*sin(vpTeta[0])+1)))*cos(vpTeta[0]);
    d1=2*h*sqrt((Vmean*sin(vpTeta[0])-1)/(Vmean*sin(vpTeta[0])+1));
    d2=D3;
    if ((h>=0) && (h<=H1))
    {
       D=D1;
    }
    if ((h>H1) && (h<=H2))
    {
       D=D2;
    }
    if (h>H2)
    {
       D=D3;
    }

    // d
    if ((h>=0) && (h<=h1))
    {
       d=d1;
    }
    if (h>h1)
    {
       d=d2;
    }

    // now the final LET
    R=D/(2*h);
    r=d/(2*h);
    K=(1+(r*r))/(1-(r*r));
    V=sqrt(1+R*R*(K+1)*(K+1));
    V2=V*V;
    V3=V2*V;
    V4=V3*V;
    V5=V4*V;
    V6=V5*V;

    if ((V>=1.04) && (V<=2.1))
    {
```

```
   LETsim=-662.69*V6+6337.9*V5-24883*V4+51240*V3-58254*V2+34691*V-8466.9;
}

if ((V>=2.1) && (V<=6.4))
{
   LETsim=1.4132*V3-22.453*V2+149.82*V-123.06;
}

if (LETsim==0) {G4EventManager::GetEventManager()->GetConstCurrentEvent()->IsAborted(); return;}


//here we decide what to show in the output .csv file
G4int fNtupleId = 0;
G4AnalysisManager* analysisManager = G4AnalysisManager::Instance();
analysisManager->FillNtupleDColumn(fNtupleId , 0, vpPrePosition[0].x()/um);
analysisManager->FillNtupleDColumn(fNtupleId , 1, vpPrePosition[size-1].x()/um);
analysisManager->FillNtupleDColumn(fNtupleId , 2, vpEkin[0]/keV);
analysisManager->FillNtupleDColumn(fNtupleId , 3, Energyat0/keV);
analysisManager->FillNtupleDColumn(fNtupleId , 4, Vmean);
analysisManager->FillNtupleDColumn(fNtupleId , 5, vpTeta[0]/degree);
analysisManager->FillNtupleDColumn(fNtupleId , 6, D/um);
analysisManager->FillNtupleDColumn(fNtupleId , 7, d/um);
analysisManager->FillNtupleDColumn(fNtupleId , 8, LETsim);
analysisManager->AddNtupleRow(fNtupleId);
G4cout<<eventID<<" YO, A PROTON! Its LETsim is:"<<LETsim<<G4endl;
```

References

[1] "The Statute of the IAEA | IAEA." [Online]. Available: https://www.iaea.org/about/statute. [Accessed: 26-Jun-2020].

[2] "Ionizing Radiation Dosimetry Laboratory (LDRI)." [Online]. Available: https://www.irsn.fr/EN/Research/Research-organisation/Research-units/human-radiation-protection-unit/LDRI/Pages/ionizing-radiation-dosimetry-laboratory.aspx. [Accessed: 26-Jun-2020].

[3] International Commission on Radiological Protection (ICRP), *ICRP Publication 60*, vol. 6, no. 1. 1981.

[4] International Commission on Radiological Protection (ICRP), *ICRP Publication 103*, no. 0. 2003.

[5] International Commission on Radiological Protection (ICRP), "Basis for dosimetric quantities used in Radiological Protection," 2005.

[6] International Commission on Radiological Protection (ICRP), *ICRP Publication 118*, vol. 6, no. 1. 1981.

[7] Institut de Radioprotection et de Sûreté Nucléaire (IRSN), "La radioprotection des travailleurs - Exposition professionnelle aux rayonnements ionisants en France : bilan 2018," 2019.

[8] S. Pomp, "Tutorial on neutron physics in dosimetry," *Radiation Measurements*, vol. 45, no. 10, pp. 1090–1095, Dec. 2010, doi: 10.1016/j.radmeas.2010.06.021.

[9] S. Einav *et al.*, "The nucleotide binding motif of hepatitis C virus NS4B can mediate cellular transformation and tumor formation without Ha-ras co-transfection," *Hepatology*, vol. 47, no. 3, pp. 827–835, Mar. 2008, doi: 10.1002/hep.22108.

[10] M. Caresana, M. Ferrarini, L. Garlati, and A. Parravicini, "Further studies on ageing and fading of CR39 PADC track detectors used as air radon concentration measurement devices," *Radiation Measurements*, vol. 46, no. 10, pp. 1160–1167, Oct. 2011, doi: 10.1016/j.radmeas.2011.07.040.

[11] "JANIS - Renderer." [Online]. Available: http://www.oecd-nea.org/janisweb/book/neutrons/O16/MT2/renderer/403. [Accessed: 12-Jul-2020].

[12] D. Nikezic and K. Yu, “Formation and growth of tracks in nuclear track materials,” *Materials Science and Engineering: R: Reports*, vol. 46, no. 3–5, pp. 51–123, Dec. 2004, doi: 10.1016/j.mser.2004.07.003.

[13] M. Caresana, M. Ferrarini, M. Fuerstner, and S. Mayer, “Determination of LET in PADC detectors through the measurement of track parameters,” *Nuclear Instruments and Methods in Physics Research, Section A: Accelerators, Spectrometers, Detectors and Associated Equipment*, vol. 683, pp. 8–15, Aug. 2012, doi: 10.1016/j.nima.2012.04.071.

[14] M. Bolzonella, “Characterization of a passive dosimeter based on a CR-39 track detector for envoironmental and personal dosimetry in neutron mixed fields,” 2019.

[15] Politecnico di Milano; Mi.am SRL, “Politrack - Automatic Track Detector Reader,” 2009.

[16] M. Caresana, M. Ferrarini, A. Parravicini, and A. Sashala Naik, “Evaluation of a personal and environmental dosemeter based on CR-39 track detectors in quasi-monoenergetic neutron fields,” *Radiation Protection Dosimetry*, vol. 161, no. 1–4, pp. 100–103, Oct. 2014, doi: 10.1093/rpd/nct320.

[17] P. Servell, “Dosimétrie individuelle des neutrons Rapport de projet de fin d’études,” Fontenay-aux-Roses, 2019.

[18] “Track Analysis Systems Ltd - TASTRAK PADC.” [Online]. Available: http://www.tasl.co.uk/plastics.php. [Accessed: 24-Jul-2020].

[19] “L’IRSN adapte son fonctionnement pour continuer à assurer ses missions dans la situation actuelle.” [Online]. Available: https://www.irsn.fr/FR/Actualites_presse/Actualites/Pages/2020324_Confinement-Covid-19-Fonctionnement-IRSN.aspx#.XyGcv-fOMUQ. [Accessed: 29-Jul-2020].

[20] “Premières irradiations sur le microfaisceau MIRCOM.” [Online]. Available: https://www.irsn.fr/FR/Larecherche/Actualites_Agenda/Actualites/Pages/2018-11-27-premieres-irradiations-microfaisceau-MIRCOM.aspx#.Xx1jcufOOHs. [Accessed: 26-Jul-2020].

[21] V. Gressier *et al.*, “AMANDE: a new facility for monoenergetic neutron fields production between 2 keV and 20 MeV,” *Radiation Protection Dosimetry*, vol. 110, no. 1–4, pp. 49–52, Aug. 2004, doi: 10.1093/rpd/nch185.

[22] “Le microfaisceau Mircom.” [Online]. Available: https://www.irsn.fr/FR/Larecherche/outils-scientifiques/installations-moyens-experimentaux/microfaisceau-mircom/Pages/default.aspx. [Accessed: 26-Jul-2020].

[23] V. Gressier, G. Pelcot, J. L. Pochat, and T. Bolognese-Milstajn, “New IRSN facilities for neutron production,” *Nuclear Instruments and Methods in Physics Research Section A: Accelerators, Spectrometers, Detectors and Associated Equipment*, vol. 505, no. 1–2, pp. 370–373, Jun. 2003, doi: 10.1016/S0168-9002(03)01099-4.

[24] “AMANDE facility.” [Online]. Available: https://www.irsn.fr/EN/Research/Scientific-tools/experimental-facilities-means/Amande/Pages/Amande-facility.aspx. [Accessed: 29-Jul-2020].

[25] “History - NPL.” [Online]. Available: https://www.npl.co.uk/history. [Accessed: 01-Aug-2020].

[26] National Physical Laboratory, *NPL’s History highlights*. 2015.

[27] “Neutron standards - NPL.” [Online]. Available: https://www.npl.co.uk/nuclear-metrology/neutron-standards. [Accessed: 01-Aug-2020].

[28] International Organization for Standardization, *ISO 8529-1:2001*. 2001.

[29] “Geant4 Scope of Application — IntroductionToGeant4 10.6 documentation.” [Online]. Available: http://geant4-userdoc.web.cern.ch/geant4-userdoc/UsersGuides/IntroductionToGeant4/html/IntroductionToG4.html. [Accessed: 09-Apr-2020].

[30] “Physics Lists | geant4.web.cern.ch.” [Online]. Available: https://geant4.web.cern.ch/support/physics_lists. [Accessed: 03-Jun-2020].

[31] “Low Energy Electromagnetic Physics - Livermore | geant4.web.cern.ch.” [Online]. Available: https://geant4.web.cern.ch/node/1619. [Accessed: 17-Apr-2020].

[32] “James Ziegler - SRIM & TRIM.” [Online]. Available: http://www.srim.org/. [Accessed: 03-May-2020].

[33] G. Somogyi and S. A. Szalay, “Track-diameter kinetics in dielectric track detectors,” *Nuclear Instruments and Methods*, vol. 109, no. 2, pp. 211–232, Jun. 1973, doi: 10.1016/0029-554X(73)90265-6.

[34] A. Allaoua, “Etude et développement de détecteurs dédiés aux mesures de référence de champs neutroniques mono-énergétiques,” 2009.